Deep Hi Observations Of Nearby Late-Type Galaxies

Amidou Sorgho

May 2019

A thesis submitted in partial fulfilment for the degree of Doctor of Philosophy in Astronomy

Department of Astronomy
UNIVERSITY OF CAPE TOWN

Supervisor: Claude Carignan

Abstract

This thesis makes use of sensitive HI observations to map the distribution and kinematics of the low column density neutral hydrogen in late-type nearby mostly isolated galaxies and in the nearby M81 group.

Using the KAT-7, GBT and MeerKAT AR1 telescopes, we present in the second chapter a survey of the HI in a sample of twenty nearby, mostly isolated galaxies down to low column density levels. This provided a new HI view of some of these galaxies, which allowed to derive their kinematics out to unprecedented extents. Despite the short spacings of KAT-7 and MeerKAT AR1, and the large size of the single-dish GBT that make these telescopes ideal for detecting faint structures, the observations revealed no clear detection of low column density HI clouds down to a typical sensitivity of $\sim 2.2 \times 10^{18}\,\mathrm{cm}^{-2}$ that could be associated to gas accretion in the observed galaxies. However, we do not discard the existence of such structures that, we note, could be in the form of discrete clouds smaller than the beam size of the telescopes.

In the third chapter, we use the DRAO telescope to perform a sensitive survey of the HI in a $5^\circ \times 5^\circ$ area of the M81 group. Similarly to previous observations, we find that the three major and interacting galaxies of the group – M81, M82 and NGC 3077 – are connected through HI bridges and intergalactic HI clouds. One of the major findings of the survey is the more complete map of the western HI arm connecting the three galaxies to the dwarf galaxy NGC 2976. These observations offer enough resolution to map the structure of the arm, and reveal a complex of small clouds filling the space between the arm and the HI forming "main body" of the interacting galaxies. Using a tilted-ring model, we also construct a large-scale rotation curve of the system formed by the interacting galaxies. Consistently with the large-scale velocity field, we observe a flat trend for the rotation velocity of the system from 20 kpc out to 80 kpc, well beyond the outskirts of the M81 disk, although with asymmetries like a wiggle at the vicinity of M82.

The fourth chapter focuses on a subset of the M81 survey containing the dwarf galaxy IC 2574 and the HI complex HIJASS J1021+68. In this chapter we perform

a thorough analysis of the distribution and kinematics of the HI in the two systems, and thanks to the high sensitivity we are able to detect a substantially large amount of low column density HI around IC 2574, in the form of an HI envelope, and in two large concentrations around the galaxy. We find evidence that HIJASS J1021+68 – which is found to be connected to IC 2574 through a filament of discrete clouds – is not a dark galaxy as previously suggested, but is instead a complex of clouds either stripped from, or falling onto the primordial HI envelope of IC 2574. The kinematical analysis of IC 2574 using a 3D tilted-ring model brings us to derive its rotation curve out to a larger extent than previous works and allows us to constrain its Dark Matter halo parameters, which we find consistent with the literature.

Overall, the different results presented in this work prove that the HI content of local galaxies is higher than what current observations reveal, and new sensitive telescopes such as MeerKAT and the upcoming SKA will unveil a new HI view of galaxies.

Acknowledgements

The completion of this PhD thesis may have taken just a few years, but my journey in the field of astronomy goes way back when I attended my first astronomy class with Prof. Carignan back in Burkina Faso. I certainly would have not had the motivation to pursue postgraduate studies, had he not given me the opportunity to study astronomy. With these few modest lines, I would like to express my deep and sincere gratitude to him for not only giving me the privilege to work with him, but also for believing in me when he had every reason not to. As you prepare to retire, Professor, I would like you to know that besides your many valuable contributions to the advancement of astronomy, your kind heart has motivated many young people to move forward and embrace the field of astronomy. I cannot thank you enough for your patience and your support during all those years.

My family has been understanding and has offered me of a great support during these long years, and I could not have completed this degree without their unconditional love. For what it's worth, a day has not passed by without thinking of you and praying God to keep you safe. To Karim, Zeynab, Adama, Boukary, Souley and Aicha, I say thank you for all your sacrifices, your support and your prayers. To Joseph, who I consider more a brother than a friend, I am deeply grateful for the continued support. You have always responded whenever I needed you, and I am lucky to have you in my circle.

I thank Laurent Chemin and Tyler Foster who I have collaborated with during the last two years of this PhD degree. More than a collaborator, Laurent has been a good friend and an excellent mentor, and his different pieces of advice have made the ride much smoother. In fear of not being able to finish my PhD programme in time when I was waiting for DRAO data, I remember spamming Tyler with emails out of stress. He has found a way to keep his calm and has always shown me respect, and his words of appreciation were more than encouraging. Working with the both of you has allowed me to learn a lot, and I thank you a lot for that.

An important part of the learning process during the PhD is done through interactions with seniors and experienced scientists in the field. I have had the chance during these last few years to collaborate with D.J. Pisano, Tom Oosterloo and Erwin de Blok. Their remarkable simplicity, humility and openness has made the interaction much easier, and the experience they shared with me has been very helpful. I

would like to thank them for that.

To Roslyn, Nicky and Carol at the Astronomy Department of UCT, I would like express my gratitude. During these tedious years they have not stopped showing me support and encouragement. Besides having to professionally handle paperwork issues, they have made themselves available to listen and discuss whenever I was feeling down. This meant a lot to me, and I would like you to know that you were part of this journey. Monique Mujawamariya has been the "aunty" that never failed to find the right words to encourage me in this journey, and I value the motherly love she gave me. Siphelo has luckily been around to help me through IT support whenever Google wasn't helpful enough, and for that I would like to say "thank you Chief!"

Pursuing a PhD away from home can be challenging, as it demands a certain moral support and human connection that we sometimes fail to get from friends. I was lucky to have good friends like Marie and Marc who stood by me when I suffered the loss of my sister, and when I was not sure if I would see the end of the PhD programme. Thank you for being there during the storms, and also for the beautiful memories which I hold dear to. I thank Loriane for her moral support and words of encouragement, and also thank Blaise and Julien for their friendship.

I would like to thank all the collaborators I have had the chance to work with, I acknowledge your various contributions. A big thanks to Tom Jarrett for providing the infrared data used in this work; thank you to Kelley Hess for her mentorship during my MSc and to Danielle Lucero for the great help she offered during the observations with the KAT-7 telescope.

I thank the entire Astronomy Department of UCT. From the HoD Prof. Patrick Woudt to the entire staff, to the postdocs and fellow postgraduate students I express my thanks. I particularly thank my office mates with who I had numerous sessions of good laugh. Thank you all for the social activities and the different chats in the office, the library and the seminar room.

I extend my gratitude to the friends and elders at the Université Joseph Ki-Zerbo back in Ouagadougou in Burkina Faso. I particularly thank Pierre "Tonton Pierre" Sanon for his wise words of advice, Zach Kam, Issouf Kafando, Sidiki Zongo and Issa Ouattara for their support.

Last but not least, I would like to thank all these anonymous people that I have come to interact with during the completion of this degree, be it in Cape Town, Ouagadougou or elsewhere. Your different acts of kindness have helped me move forward, and I pray that good things happen in your life. Keep spreading love, you are the beauty of this "pale blue dot" that is our world.

To Mom, Dad, and Abiba.

Declaration of Authorship

The work presented in this thesis was done under the supervision of C. Carignan and in collaboration with various people who provided some of the data and in some cases contributed to the analysis and discussion. This thesis contains research that has already been published or submitted for publication:

1. Chapter 2 (Paper I) entitled "Early Observations of the MHONGOOSE Galaxies: Getting ready for MeerKAT" has been published in the *Monthly Notices of Royal Astronomical Society Journal*; **A. Sorgho**, C. Carignan, D. J. Pisano, T. Oosterloo, W. J. G. de Blok, M. Korsaga, N. M. Pingel, Amy Sardone, S. Goedhart, S. Passmoor, A. Dikgale and S. K. Sirothia, 2019, MNRAS 482, 1248

We use the MeerKAT AR1, KAT-7, and GBT telescopes to investigate the HI distribution and kinematics in a sample of twenty nearby galaxies. After identifying the best calibrators for the galaxies observed with the KAT-7 telescope, we search for signs of gas accretion in the GBT data down to column densities of $\sim 2.2 \times 10^{18}\,\mathrm{cm}^{-2}$ at physical resolutions ranging from 9 to 64 kpc, and over a 20 km s^{-1} line width. Although we identify none, this allows us to set an upper limit on the column density levels and size scales (corresponding to the values quoted above) above which one can expect to detect signs of gas accretion in these galaxies. Next, we use the KAT-7 and MeerKAT observations to derive the rotation curves and mass models of two galaxies – NGC 3621 and NGC 7424 – out to an unprecedented extent, allowing us to construct their mass distributions. We find that the results obtained with the pseudo-isothermal model are the most consistent with observations, compared to the Navarro-Frenk-White and MOND models.

2. Chapter 3 (Paper II) entitled "A $5^\circ \times 5^\circ$ deep HI survey of the M81 group" has been published in the *Monthly Notices of Royal Astronomical Society Journal*; **A. Sorgho**, C. Carignan, L. Chemin, T. Foster, 2019, MNRAS, 486, 504

We study the HI distribution in the M81 group using a deep survey carried with the DRAO telescope. This survey is unprecedented, as no other survey had probed

before such a large area of the M81 group at such high sensitivity in HI. The survey allowed us to map and resolve, for the first time, the full extent of the western HI arm connecting the M81 interacting system to NGC 2976, a dwarf galaxy located south of the complex. Also, accounting for the ordered motion of the HI gas in the M81-M82-NGC3077 system, we have used the tilted-ring model to derive the rotation curve of the system. This reveals a roughly constant rotation of the complex over a large range of radii, with a prominent wiggle associated to M82, as if the outermost gas and galaxies were rotating at the same speed as the inner disk of M81. We also noted a non-negligible radial motion in the model, perhaps highlighting the streaming of outer gas and galaxies with respect to M81.

3. Chapter 4 (Paper III) entitled "A $5^\circ \times 5^\circ$ deep HI survey of the M81 group: II. HI distribution and kinematics of IC 2574 and HIJASS J1021+68" has been submitted for publication to the *Monthly Notices of the Royal Astronomical Society Journal*; **A. Sorgho**, L. Chemin, Z. S. Kam, T. Foster, C. Carignan, MNRAS (submitted)

We focus on the subset of the M81 survey covering the dwarf galaxy IC 2574 and the gas complex HIJASS J1021+68, and perform a thorough analysis of the distribution and kinematics of the HI in the two systems. Taking advantage of the high sensitivity of the observations, we explore the circumgalactic environment of IC 2574 and map, for the first time, its extended envelope of low column density HI. We also detect small blobs of HI in the space between the galaxy and HIJASS J1021+68, a complex that was previously identified as a dark galaxy, and was not resolved before in any observation. This confirms an earlier claim of a previous study that the gas complex is connected to IC 2574, and our study shows that the connection is made through a filament of gas clouds. The kinematical analysis of IC 2574 allows us to derive its rotation curve to a larger extent than previous works, and the mass distribution inferred from this using the pseudo-isothermal dark matter model provides a mass-to-light ratio consistent with the morphology of the galaxy.

Each of these chapters contains all the information to be read independently.

I confirm that I have been granted permission by the University of Cape Town's Doctoral Degrees Board to include the following publications in my thesis, and where co-authorships are involved, my co-authors have agreed that I may include the publications:

1. A. Sorgho, C. Carignan, D. J. Pisano, T. Oosterloo, W. J. G. de Blok, M. Korsaga, N. M. Pingel, Amy Sardone, S. Goedhart, S. Passmoor, A. Dikgale and S. K. Sirothia, "Early Observations of the MHONGOOSE Galaxies: Getting ready for MeerKAT", 2019, MNRAS 482, 1248.

2. A. Sorgho, C. Carignan, L. Chemin, T. Foster, "A $5° \times 5°$ deep HI survey of the M81 group", 2019, MNRAS, 486, 504.

3. A. Sorgho, L. Chemin, Z. S. Kam, T. Foster, C. Carignan, "A $5° \times 5°$ deep HI survey of the M81 group: II. HI distribution and kinematics of IC 2574 and HIJASS J1021+68", MNRAS (submitted)

SIGNATURE: Signed by candidate **DATE**: May 22nd, 2019

STUDENT NAME: Amidou Sorgho **STUDENT NUMBER**: SRGAMI001

Plagiarism Declaration

I, Amidou Sorgho, know the meaning of plagiarism and declare that all of the work in the document, save for that which is properly acknowledged, is my own.

Contents

List of Figures

List of Tables

Chapter 1

Introduction

Galaxies have long been the subject of numerous studies in the astrophysics community. While a lot of progress was made over the past few decades about their structure and the mechanisms regulating their evolution, a complete picture of their formation and evolution remains uncovered. Several types of telescopes were built in the effort of investigating galaxies and their environments, each probing a specific window of the electromagnetic spectrum. That is, these telescopes allow us to observe galaxies in different observing bands, ranging from the high energy Gamma ray bands to the low energy radio wavelengths. Observations in each of these bands reveal a different aspect of galaxies and their environments, making each band uniquely important in understanding the complex properties of galaxies and their kinematics. For example, at the optical wavelengths, one probes the stellar components and the ionised gas of the galaxy while the X-ray traces the hot gas surrounding the galaxies and abundant in the intracluster medium (ICM). At radio wavelengths, it is mainly the neutral hydrogen gas (HI), usually extending further out than the stellar disc (see e.g. Roberts 1972), that is detected thanks to its line emission. In continuum mode, radio wavelengths also map star forming regions and Active Galactic Nuclei (AGN) in galaxies.

The lifetime of a galaxy typically spans billions of years, which, compared to humans' timescales, is an eternity. So, besides observing galaxies at different stages of their "life" to comprehend their evolution, astrophysicists use numerical simulations and semi-analytic models. Currently, the most widely accepted model in the astrophysics community is the Lambda[†] Cold Dark Matter (ΛCDM) cosmological model (e.g. Dekel & Silk 1986, Frenk et al. 1988, Klypin et al. 1999) which predicts the existence of a non-baryonic, unseen matter dubbed Dark Matter (DM), that makes

[†]Lambda (Λ) represents the cosmological constant, closely associated with dark energy

up a large fraction of galaxies. The ΛCDM cosmology, supported by observations, predicts that matter in the Universe (baryonic and non-baryonic) is not uniformly distributed on large scales, but rather form a web-like pattern known as the "cosmic web" (Klypin & Shandarin 1983, Bond et al. 1996, Springel et al. 2005). The cosmic web is composed of dense clusters, sparsely populated voids, planar walls and thread-like filaments linking overdense regions. Clusters and filaments are found to be the most prominent components of the cosmic web (Cautun et al. 2014), where the majority of the baryonic matter is expected to be found. However, not all the baryons predicted by simulations can be recovered by observations. In fact, only a small fraction of these baryons is recovered by adding up the masses of visible baryons (Persic & Salucci 1992, Fukugita et al. 1998, Fukugita & Peebles 2004), suggesting that a large fraction is unseen. This discrepancy between observations and the predictions of numerical simulations is referred to as the "missing baryons problem", and it is believed that an important fraction of the baryonic mass is hidden in extended gaseous web-like filaments (e.g., Cen & Ostriker 1999, Davé et al. 2001) and as diffuse low column density gas around galaxies. Moreover, current star formation rates (SFRs) of nearby galaxies, as derived from observations, are an order of magnitude higher than what can be sustained by minor mergers and accretion (Sancisi & Fraternali 2008, Kauffmann et al. 2010). This suggests that local galaxies must somehow be accreting gas from the intergalactic medium (since minor mergers with satellite galaxies do not play a significant role in the gas accretion budget; e.g, Di Teodoro & Fraternali 2014), and further confirms the existence of missing baryons in the form of low density gas. Several authors have aimed at detecting these missing baryons by making a full census of the gas in and around nearby galaxies, using deep HI observations (e.g., Pisano 2014).

In this thesis, we use deep HI observations to not only investigate the HI content of nearby galaxies from the faint, low column density gas around, to the high column density gas residing in them, but we also study the HI kinematics of these galaxies. But before we dive into the subject, it is important to take a step back and briefly review the literature about the HI and DM content of galaxies, as well as the fundamentals of the instruments that allow the detection of the HI emitted by galaxies and extragalactic structures: radio telescopes.

1.1 HI content of nearby galaxies

1.1.1 Types and distribution of galaxies

Galaxies come in different sizes and shapes. From as early as 1920s, several attempts to classify galaxies based on their structures have been made, with the most commonly scheme used being the Hubble (1936) classification. This scheme was soon interpreted by other astronomers as an evolutionary sequence*: galaxies follow a sequence (known as the "tuning fork") where they evolve from ellipticals to spirals as they flattened out and developed arms. Although this evolutionary sequence was later found to be incorrect, the proposed classification scheme provided a basis upon which later classification systems such as the de Vaucouleurs (1959) and the revised Hubble (Sandage & Allan 1961) classifications were formed. From the Hubble system of classification, it is known that there exists three main types of galaxies, based on their optical morphologies: ellipticals (and lenticulars), spirals and irregulars.

Commonly referred to as early type galaxies, ellipticals and lenticulars are usually shaped like a spheroid, with an optical surface brightness decreasing monotonically from the centre outward. The simplified picture of these galaxies is that they are 'red and dead', contain mainly old stellar populations (e.g., Bower et al. 1992), and with almost no star formation taking place inside them. Their HI content is generally negligible. However, the actual picture was found to be more complex by some authors, and it is now established that a significant fraction of early type galaxies are hosting, or have hosted in their recent past, some amount of star formation (e.g. Trager et al. 2000, Yi et al. 2005, Kaviraj et al. 2007). More interestingly, a survey of nearby early type galaxies (Serra et al. 2012b) has detected HI in a significant fraction ($\sim$40%) of these galaxies outside clusters, demonstrating that it is common for non-cluster early type galaxies to host HI.

On the other hand, spiral and irregular galaxies (also known as late-type galaxies) are characterised by their morphologies that diverge from those of ellipticals. They are known to have a high content of HI, and have been the target of most HI studies. Spirals usually have at least two baryonic components: a disc composed of young stars, gas and dust, and a spherical bulge containing a mostly old stellar population. Because of their high content of young stars and the ongoing star formation within their discs, late-type galaxies are generally observed to have a blue colour. Kinematically, late-type galaxies rotate in the plane of their disc around their central bulge, and spirals are particularly known to exhibit arms that are mostly traced by

*It is widely believed that Hubble introduced the terms "early" and "late" to suggest an evolutionary sequence but, as discussed in Baldry (2008), this is a misconception.

the molecular hydrogen (HII).

The hierarchical models (e.g. White & Rees 1978, White & Frenk 1991, Springel et al. 2005) suggest that large galaxies are products of mergers between smaller galaxies. When the merger occurs between a pair of late-type, blue spirals, the resulting galaxy is generally (depending of the relative size of the merging galaxies) an early-type, red elliptical galaxy (Toomre & Toomre 1972, Mihos & Hernquist 1996). In principle, these mergers enhance the star formation activity in the interacting galaxies (e.g., Mihos & Hernquist 1996, Di Matteo et al. 2007), which tends to deplete their HI reservoir. This explains the poor content of HI in early type galaxies. In contrast, spiral galaxies that have not undergone these processes are expected to have a relatively large amount of neutral gas.

As mentioned earlier, the ΛCDM cosmology prescribes that matter is not uniformly distributed in the Universe, but rather in structures that form the cosmic web. Galaxies are no exception, as large surveys such as the SDSS (Sloan Digital Sky Survey; York et al. 2000), the 2dFGRS (2dF Galaxy Redshift Survey; Colless et al. 2001; 2003), the 2MASS (Two-Micron All Sky Survey; Huchra et al. 2005) and GAMA (Galaxy and Mass Assembly; Alpaslan et al. 2014) have shown that they tend to clump together to form large scale structures such as clusters, groups, filaments, etc. It is now known that clusters and filaments are the most massive components of the cosmic web, while underdense voids and walls occupy most of the volume (e.g. Cautun et al. 2014). A typical cluster comprises about a hundred to several thousands galaxies, gravitationally bound together and embedded in a large scale DM halo, while a group only contains a few to a hundred galaxies. Studies of the distribution of galaxies in different environments revealed that early type galaxies tend to reside in the dense environments of clusters, while late types are mostly found in less dense environments such as the outskirts of clusters, groups and voids (Hubble & Humason 1931, Dressler 1980). In this thesis we exclusively study late-type galaxies selected in sparsely populated environments, and use radio wavelength observations to investigate their HI contents.

1.1.2 The neutral hydrogen line

The HI line is detected at a frequency of 1.42 GHz (more precisely at 1.420405752 GHz, corresponding to a wavelength of about 21 cm), a window of the electromagnetic spectrum that is little affected by atmospheric absorption. The line was first predicted by van de Hulst (1945) and later discovered by Ewen & Purcell (1951), and is a result of magnetic interactions between the proton and the electron of the hydrogen atom. About every 1/11 Myr, an electron spin-flip transition (from parallel

to antiparallel) occurs in the ground state of the atom, producing a 21-cm photon. Because of the low emission rate of the transition, the HI line occurs very rarely; however, its detection is made possible by the very high column densities ($\gtrsim 10^{18}\,\mathrm{cm}^{-2}$) of the atomic hydrogen in the ISM (and often in clouds residing in the intergalactic medium, e.g. Wolfe et al. 2013). Indeed, in the low density regions of the interstellar medium (ISM) and below temperatures of about 10^4 K, the hydrogen exists in its atomic form, and is the most abundant baryonic element in the medium.

The HI line has widely been used to study the neutral gas in low redshift galaxies, including our own. Contrary to the traditional optical imaging (besides Fabry-Pérot and Integral Field Units) which provides a spatial view of the targets, HI line observations offer the observer a three-dimensional picture. On top of the two dimensions (right ascension and declination) needed for a spatial view, they provide a spectral dimension (thanks to the Doppler shift) which informs us about the structure of the emitting gas in the targets. This allows the observer to not only obtain the physical properties of galaxies such as their diameter and density distribution, but also to be informed about the associated kinematics of their ISM. In fact, the 21-cm emission is optically thin, implying that one can directly convert the total amount of HI seen along a particular line of sight into an HI mass density.

In this thesis we will frequently use the HI column density and mass of galaxies to quantify their HI content. While the notion of HI mass is trivial, it is worth noting that the column density gives the observer an idea on the density of the hydrogen atoms in the probed medium. In other words, it represents the number of neutral hydrogen per unit area along a particular line of sight. The column density is related to the line flux (integrated along the line of sight) I_ν by

$$N_{\mathrm{HI}}(\mathrm{cm}^{-2}) = 1.249 \times 10^{24}\, I_\nu/\Omega \tag{1.1}$$

where I_ν has units of Jy km s^{-1}, and Ω is the telescope beam solid angle in arcsec^2. If the line flux is furthermore integrated over the entire galaxy, then one can determine its total HI mass by

$$M_{\mathrm{HI}}(\mathrm{M}_\odot) = 2.36 \times 10^5\, D^2\, I_{\mathrm{tot}} \tag{1.2}$$

with D being the redshift-independent distance to the galaxy in Mpc and I_{tot} its total integrated flux.

1.1.3 HI discs

While the stellar and other baryonic components of galaxies are mostly confined to their stellar discs, the neutral hydrogen generally extends far beyond, especially in

late-type spiral and irregular galaxies. This makes the HI a sensitive tracer of past and current interactions of galaxies with their environment, since most interactions happen at large scale. The first observational studies of HI discs of galaxies using aperture synthesis to image the HI at reasonable angular resolution were conducted as early as in the 1970s (e.g., Rogstad & Shostak 1971, Baldwin et al. 1971, Allen et al. 1973, Roberts & Whitehurst 1975). These studies have revealed that the HI discs of late type galaxies usually extend farther than their stellar discs (see e.g. Roberts 1972). More specifically, a more recent study (Broeils & Rhee 1997) has found that the HI diameters of late type galaxies, measured at a surface density level of 1 $M_\odot\,pc^2$ ($1.25 \times 10^{20}\,cm^{-2}$), is on average 1.7 ± 0.5 times larger than their optical diameter (defined at the 25th B-band magnitude). Furthermore, although not frequent, there exist several late-type galaxies known to host large HI envelopes that greatly extend beyond the optical disc (e.g., M83: Rogstad et al. 1974, Huchtmeier & Bohnenstengel 1981, Heald et al. 2016; M101: Huchtmeier & Witzel 1979; NGC 925: Heald et al. 2011; NGC 2915: Meurer et al. 1996). As an example, Fig. 1.1 shows the extended HI envelope of M83 taken from Heald et al. (2016). Huchtmeier & Bohnenstengel (1981) measured the extent of the galaxy's HI envelope to be 6.5 times its optical size. These extended envelopes are often made of gas which has not yet been accreted onto the central galaxy, and these types of envelopes are thought to represent the remnants of the primordial HI from which the hosting galaxy has formed (e.g., Morris & Wannier 1980, van Woerden et al. 2004). In some other cases, the envelope is believed to have formed after the HI has been stripped from the central galaxy due to ram-pressure or gravitational interaction (e.g., NGC 3628: Haynes et al. 1979; NGC 4522: Vollmer et al. 2004, Kenney et al. 2004; NGC 4424: Chung et al. 2007, Sorgho et al. 2017), or after the HI has been "swept" by large-scale galactic winds or outflows (e.g. Koribalski et al. 1993, McKeith et al. 1995, Heckman et al. 1995).

Several targeted HI surveys of nearby late-type galaxies exist in the literature. For example, the WHISP (Westerbork HI Survey of Spiral and Irregular Galaxies; Swaters et al. 2002, Swaters & Balcells 2002, Noordermeer et al. 2005), THINGS* (The HI Nearby Galaxy Survey; Walter et al. 2008) and HALOGAS (Westerbork Hydrogen Accretion in LOcal GAlaxieS; Heald et al. 2011) surveys have improved our understanding of galaxy evolution by investigating the properties and kinematics of the HI in nearby late-type galaxies. The HALOGAS survey has performed deep observations of the diffuse HI in 24 nearby galaxies down to a typical column density limit of $10^{19}\,cm^{-2}$, in the hope of revealing the global characteristics of cold

*http://www.mpia.de/THINGS/Overview.html

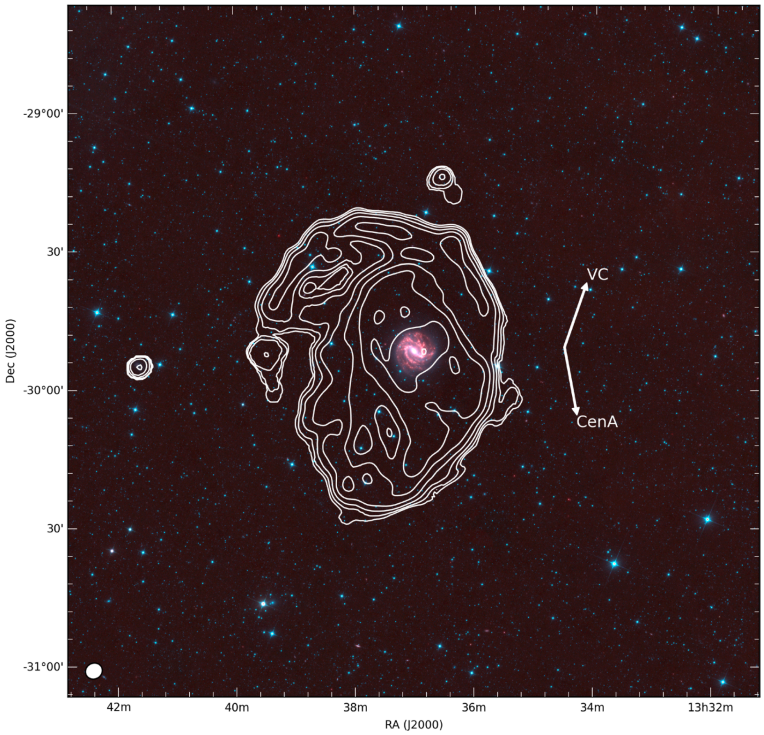

Figure 1.1: Total HI intensity map of M83 overlaid on a three-colour infrared *WISE* image. The HI distribution shows the extended envelope of the galaxy. Image taken from Heald et al. (2016).

gas accretion onto spiral galaxies in the local Universe. At an intermediate spatial resolution ($\sim 30''$), the survey investigated the properties of extraplanar HI in several galaxies (e.g., NGC 3198: Gentile et al. 2013; NGC 4414: de Blok et al. 2014; NGC 1003 & UCG 7774: Heald 2015; NGC 4559: Vargas et al. 2017) and found that most of the sample galaxies host thick HI discs and contain little extraplanar neutral gas (see Zschaechner et al. 2011; 2012).

By studying the distribution of the neutral hydrogen in the HI discs of 34 nearby galaxies at a high spatial ($\sim 6''$) and spectral ($1.3-5.2$ km s^{-1}) resolutions, THINGS has probed, on the sub-kpc scale, the kinematics of the ISM in the inner regions of galaxies by providing high resolution data cubes. The rotation curves (i.e, the variations of the rotation velocity with radius) derived from the THINGS data (de Blok et al. 2008) have shown that generally, the rotation velocities of luminous galaxies (mostly early-type spirals) increase steeply in their inner regions, slowly decline afterwards, and tend to be constant in the outer regions; on the other hand, the rotation velocities of less luminous galaxies (late-type spirals) increase gradually, and never quite remain constant over the extent of their HI discs. Rotation curves are a powerful tool for studying the mass distribution of galaxies. In fact, the total (baryonic and dark) mass $M_{\rm tot}(r)$ of a galaxy enclosed in a radius r is related to its rotation velocity $v_{\rm rot}(r)$ by

$$M(r) = r\, v_{\rm rot}^2(r)/G \tag{1.3}$$

where G represents the gravitational constant. So, by studying the rotation curve of a galaxy, one actually probes the distribution of its mass. Previous rotation curves of a few nearby galaxies (e.g., NGC 7793: Carignan & Puche 1990; DDO 154: Carignan & Purton 1998) had found a decline in their mass distribution, implying that their rotation may have been traced to the limit of their mass distribution. Contrarily to these results, the THINGS rotation curves of de Blok et al. (2008) have shown that, although in some curves the rotation velocity decreases at large radii out to the last measured point, none of the studied galaxies shows a decline in their curve that can unambiguously be associated with a cut-off in their mass distribution. This implies that, unlike the baryonic component of galaxies whose size is revealed by HI observations, the DM halo extends much farther from the galaxy centre.

1.2 Dark Matter halos of galaxies

One of the most important consequences of rotation curves is perhaps the discovery of the existence of the DM. Historically, the rotation of galaxies was discovered in the early 20th century, when Pease (1918) used the Mt. Wilson 60-in telescope

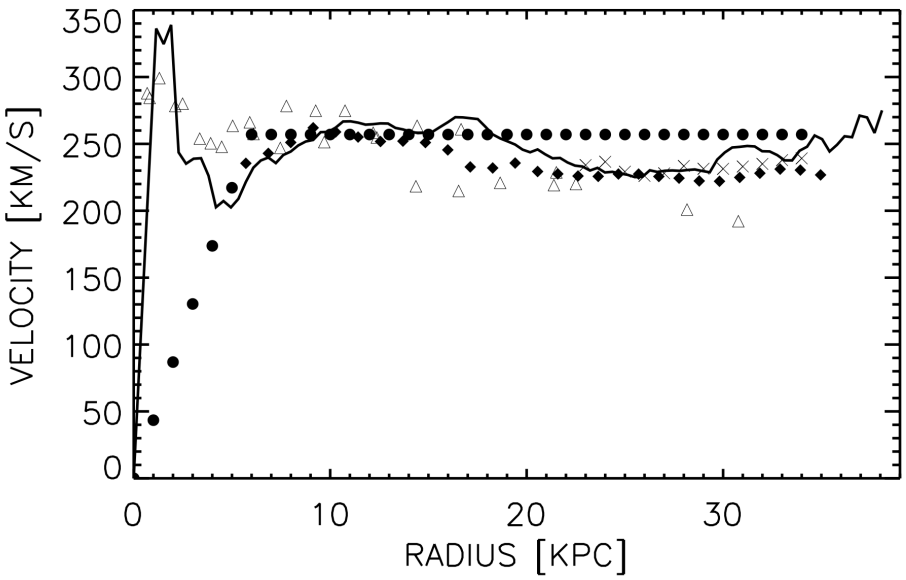

Figure 1.2: Rotation curve of M31 derived in different studies (Chemin et al. 2009), showing the rising and flat parts of the galaxy's rotation.

to investigate the rotation of M31, after previous studies had reported a few years earlier the detection of inclined optical absorption lines in a few nearby galaxies. This led later studies to derive the first rotation curves of the galaxy using optical (e.g., Babcock 1939, Mayall 1951) and HI (e.g. van de Hulst et al. 1957, Argyle 1965) emission lines.

The shape of the rotation curve observed in M31 (and later in many other disc galaxies) is what hinted at the existence of DM inside galaxies. In fact, the rotation curve was observed to rise steeply in the inner regions of the galaxy, and stay flat in the outer regions (see Fig. 1.2). If the mass distribution was traced by the distribution of light as was believed at the time, one would expect a declining rotation curve in the outer regions, one approaching Keplerian at large radii. This mass discrepancy, more pronounced in HI observations which extend farther than the optical observations (e.g., Bosma 1978; 1981a;b), was a definitive proof that a non-baryonic DM resides in galaxies and is expected to be much more dominant in the outer regions. A few decades before these extended HI studies – a few years before the first rotation curves were derived by Babcock (1939) – other authors (Zwicky 1933, Smith 1936, Zwicky 1937) had already suggested the existence of DM at much larger scales, from the distribution of galaxy velocity dispersions inside clusters, making the DM a mysterious matter that requires a particular attention.

In the inner parts of galaxies, the steep rise of the observed rotation velocities with the radius is largely attributed to the stellar disc while in the outer regions, the DM component dominates the dynamics (e.g., Rubin et al. 1978, Carignan & Freeman 1985, van Albada et al. 1985, Kent 1986). The flat rotation curve observed in the outer regions suggests that the DM must have a mass density profile that can be approximated to that of an isothermal (or a pseudo-isothermal) sphere. In the inner regions, the fraction of the rotation velocity associated with the DM is found to rise linearly with the radius, suggesting the presence of a central core of radius r_c in the DM distribution. Therefore, the DM density of the pseudo-isothermal model is given by

$$\rho_{\rm iso}(r) = \frac{\rho_0}{1 + (r/r_c)} \tag{1.4}$$

where ρ_0 is the central density and r the radius. In this profile, the mass density of the DM is approximately constant in the core, so in the inner regions one can write $\rho \sim r^{\alpha}$ with $\alpha = 0$. The velocity associated with the profile is

$$v_{\rm iso}(r) = \sqrt{4\pi G \rho_0 r_{\rm c}^2 \left[1 - (r/r_{\rm c}) \arctan\left(r/r_{\rm c}\right)\right]} \tag{1.5}$$

and gives an asymptotic velocity at large radii r.

With the advent of the first numerical N-body simulations (based on the CDM simulations) in the early 1990s, it was predicted that the density distribution of the DM in the inner regions of galaxies was described by a steep power law rather than a constant core (Dubinski & Carlberg 1991, Navarro et al. 1996b; 1997). The DM density in the "universal density profile" (Navarro et al. 1996b; 1997), also referred to as the Navarro-Frenk-White (NFW) profile, is described by

$$\rho_{\rm NFW}(r) = \frac{\rho_i}{(r/r_s)(1 + r/r_s)^2} \tag{1.6}$$

where r_s is the scale radius of the halo, and ρ_i is related to the density of the Universe at which the DM halo begins to collapse. The resulting rotation velocity can be written

$$v_{\rm NFW} = v_{200} \sqrt{\frac{\ln\left(1 + cx\right) - cx/(1 + cx)}{x\left[\ln\left(1 + c\right) - c/(1 + c)\right]}} \tag{1.7}$$

where v_{200} is the velocity at which the density of the halo exceeds 200 times the critical density of the Universe (Navarro et al. 1996b). The ratio $x = r/r_{200}$ (with r_{200} being the radius corresponding to v_{200}) represents the radius in units of virial radius, and $c = r_{200}/r_s$ the concentration of the halo. In this CDM-motivated "cuspy" model, the inner distribution of the DM density increases rapidly towards

the centre, and can be written $\rho \sim r^{\alpha}$ with $\alpha = -1$. This is in contrast with the observationally-motivated "core" pseudo-isothermal model, for which the inner mass density power law slope is $\alpha = 0$. The discrepancy between the two models, known as the "cusp/core controversy", remains one of the unsolved problems in small-scale cosmology (see a detailed review in de Blok 2010) is often cited as one of the greatest challenges faced by the CDM paradigm. Over the last few decades, much effort has been put both by observers and theoretical astronomers into solving this controversy, often by attempting to identify the accurate DM density profile of galaxies, and often by trying to reconcile observations and numerical models. For example, from as early as the mid-1990s, it was shown that the inclusion of baryonic physics and supernova feedback into numerical simulations can successfully lead to the creation of cores in originally "cuspy" profiles (Navarro et al. 1996a). In other words, the energy injected from supernova explosions within a dwarf galaxy can cause the sudden removal of gas from the centre of the galaxy's cuspy dark halo; and when the removed gas is assembled into a disc, and before it is transformed into stars, it is possible to create a core in the galaxy's dark halo. The proposed mechanism was adopted by several authors, and further works (see Read & Gilmore 2005, Mashchenko et al. 2006; 2008) have proposed that a series of moderately violent explosions is even more efficient than the initially-proposed single outburst mechanism, in transforming DM central density cusps into near-constant density cores. Pontzen & Governato (2012) analytically described later, in more detail, the physical processes behind the creation of cored profiles through repeated outbursts. Although the idea that mass outflows can produce cores inside cuspy DM profiles is generally accepted, more remains to be uncovered regarding the distribution of DM inside dwarf galaxies. For example, a recent work (Bose et al. 2019) based on high resolution simulations has noted the absence of cores inside Local Group-like dwarfs, arguing that recurrent star formation bursts alone are not sufficient to generate cores inside dwarf galaxies.

In practice, the constraint of a galaxy's DM halo is done by decomposing its observed rotation curve (generally obtained from HI line observations) into its different components: the stellar (obtained from optical observations) and gas discs, and the DM halo whose profile is "guessed" with either of the above-mentioned models. The decomposition allows to fit the model to the observed rotation curve, providing parameters such as the mass-to-light ratio (M/L) of the stellar disc and the properties of the DM halo.

While both the core-dominated pseudo-isothermal and cuspy NFW models tend to describe equally well the rotation curves of massive spiral galaxies, several studies have found that the core-dominated halo is clearly preferred over a cusp-like halo for

low-mass disc galaxies (e.g., Côté et al. 1991, de Blok et al. 2008, Oh et al. 2008, Carignan et al. 2013). In this thesis we decompose the rotation curves of two high mass, early-type spirals (Chapter 2) and a low-mass, late-type spiral (Chapter 4) using both the pseudo-isothermal and NFW models.

1.3 Radio telescopes

The HI data we use in this thesis are obtained thanks to radio telescopes. In this section we give an overview of the two types of telescopes used in the community: single dish telescopes and interferometers. Radio telescopes operate at long wavelengths (relative to optical wavelengths), corresponding to frequencies ranging from hundreds of MHz to tens of GHz. The basic requirements for a radio telescope is an antenna to collect radio waves and a receiver to detect the signal.

In general, what determines the capabilities of radio telescopes is, besides their angular resolution, their sensitivity and field of view. The resolution, function of the diameter of the telescope, determines the smallest angular size that can be resolved with the telescope. The sensitivity dictates how deep observations with the telescope can get, that is, what the level of brightness of the faintest structures is in the observations. As for the field of view, which is inversely proportional to the diameter of the antennas, it simply determines the limit of the angular size of the largest structures that can be mapped in a single pointing.

1.3.1 Single dish telescopes

Single dish telescopes are, as the name suggests, made of a single antenna of a parabolic shape that collects and directs waves towards a receiver usually mounted on the dish. There exists several single dish telescopes around the world with different sizes, with the largest and most recent (currently in commissioning phase) being the 500m diameter FAST (Five-hundred-meter Aperture Spherical Telescope; Nan et al. 2011) in China. At the time of writing of this thesis, the largest functioning single dish is the Arecibo telescope with a diameter of about 300m. The crave for large telescopes is motivated by the need for high angular resolution and sensitivity: they offer large collecting areas that make them sensitive to faint emissions, and allow to resolve structures that small telescopes cannot distinguish. However, big telescopes like FAST and Arecibo cannot be steered due to their size, so they instead have a moving feed while the dish is fixed on the ground. This limits the area of the sky that can be observed, and areas far from zenith are not easily accessible. The largest

Figure 1.3: Aerial view of the GBT telescope (taken from Ellingson 2015).

steerable single-dish telescopes, such as the Robert C. Byrd Green Bank Telescope* (GBT, used in Chapter 2; Prestage et al. 2009) and the Effelsberg telescope, are about 100m in diameter. An aerial view of the GBT is shown in Fig. 1.3.

Despite the large size of single-dish radio telescope, they still lack angular resolution. Mathematically, the angular resolution of a diffraction-limited telescope is sensibly λ/D, where λ is the observed wavelength and D the diameter of the telescope. In the 21cm, a 100m telescope yields a resolution of about $9'$ at best. This is not sufficient to resolve the sub-kpc structures of extragalactic objects, which sometimes require resolutions higher than $1'$. To achieve higher resolutions, several antennas are combined to form another type of telescope: interferometers.

1.3.2 Radio interferometers

Interferometers (*aka* synthesis arrays) are essentially made of (generally multiple) pairs of antennas with correlated outputs, providing resolutions higher than that of the individual antennas. Like in a two-slit experiment, an interferometer measures the interference pattern produced by multiple apertures; and the more antennas there are available, the more accurate is the recovered information. Two key terms are essential to understand about interferometers: the primary beam and the synthesised beam. The first is determined by the size of the constituent antennas and corresponds to the field of view of the telescope, while the latter is the angular resolution of the telescope and depends on the configuration of the array.

*GBT is a facility of the U.S.A National Science Foundation operated under cooperative agreement by Associated Universities, Inc.

Figure 1.4: Aerial view of the KAT-7 telescope (taken from Carignan et al. 2013).

Perhaps the most famous and widely used interferometer to investigate extra-galactic sources at radio wavelengths is the Karl G. Jansky Very Large Array* (VLA) telescope, whose antennas can be arranged into four different configurations, and each configuration providing a different angular resolution. At the 21cm wavelength, the highest resolution achieved by the VLA is about 1.3″ in its A-configuration (although most observations use a combination of the telescope's A and B configurations, providing a highest practical resolution of $5 - 6''$), making it the highest resolution telescope available for HI studies. Besides the VLA, interferometers such as the Westerbork Synthesis Radio Telescope (WSRT), the Australian Telescope Compact Array (ATCA), the Dominion Radio Astronomy Observatory (DRAO, see Chapter 3) telescope have facilitated several interesting and sometimes groundbreaking results.

Recently, the compact, seven-dish Karoo Array Telescope (KAT-7 Carignan et al. 2013) was built as an engineering testbed for the 64-dish MeerKAT telescope. Despite the small size of its individual dishes of 12 m, the short baselines of the telescope (ranging from 26 m to 185 m) and low system temperature (∼26 K) of its receivers made it sensitive to the large-scale, low surface brightness HI emission. We refer the reader to Chapter 2, where we present HI observations of five disc galaxies observed with the KAT-7.

In July 2018, the MeerKAT telescope† (see Camilo et al. 2018, for a description) was inaugurated‡ with the release of a continuum image of the centre of the Milky

*https://science.nrao.edu/facilities/vla/

†https://www.ska.ac.za/science-engineering/meerkat/about-meerkat/

‡see the media release at https://www.ska.ac.za/media-releases/

Way. As a precursor to the Square Kilometre Array (SKA) telescope, the first results of MeerKAT show signs of high capabilities, with the capacity of achieving sensitivities of the order of $10^{18}\,\mathrm{cm}^{-2}$ at $30''$ resolution, for a 48 hours observation (de Blok et al. 2018a). At the time of writing of this thesis, large HI surveys such as MHONGOOSE (de Blok et al. 2018a), MIGHTEE (Jarvis et al. 2017), LADUMA (Holwerda & Blyth 2010), etc. had started observing or were scheduled to start observing soon. These surveys aim to investigate different questions relating to galaxy evolution, probing the HI in both local and high redshift galaxies. In Chapter 2 of this thesis we present HI data of a nearby galaxy (NGC 3621) observed with 16 dishes of the MeerKAT Array Release 1 (AR1) as part of commissioning.

1.4 Structure of this thesis

The major part of this thesis is devoted to probing the low column density HI environments of nearby galaxies and constraining their HI kinematics. In Chapter 2 we present the observations of individual galaxies selected from the MHONGOOSE survey, conducted using both a single-dish telescope (GBT) and an interferometer (KAT-7). For two galaxies for which we have enough angular resolution, we perform a kinematical analysis which leads us to construct their mass models using the DM pseudo-isothermal and NFW halo models, and the DM-alternative MOND (MOdified Newtonian Dynamics) model.

In Chapter 3 we present a sensitive HI survey of the M81 group, in which we make a full census of the HI clouds in a $5^\circ \times 5^\circ$ region including the interacting M81 - M82 - NGC 3077 system and the dwarf galaxy IC 2574. We compare the results of this survey to previous HI surveys, which were either limited in resolution or in sensitivity. Also, accounting for the ordered motion of the interacting system, we use the tilted-ring model to derive a large-scale rotation curve of the system.

Chapter 4 is dedicated to the isolated M81 group members IC 2574 and HIJASS J1021+68. Focusing a subset of the M81 survey presented in the Chapter 3, we take advantage of the high sensitivity of the data to map an extended HI envelope around the dwarf galaxy IC 2574, and the previously catalogued dark galaxy HIJASS J1021+68. We also analyse the HI kinematics of IC 2574 and use the DM models to constrain its dark halo parameters.

Finally, we summarise the main results and give future prospects in Chapter 5.

Chapter 2

Early Observations of the MHONGOOSE galaxies: getting ready for MeerKAT

Abstract

We present early observations of 20 galaxies in the MHONGOOSE survey galaxies using KAT-7, the GBT, and MeerKAT. We present the best calibrators for five of the MHONGOOSE galaxies observed with the KAT-7, and search for signs of gas accretion in the GBT data, down to 3σ column density levels of $2.2 \times 10^{18}\,\mathrm{cm}^{-2}$ over a 20 km s^{-1} line width, but identify none. Using the KAT-7 and MeerKAT data, we have derived rotation curves and mass models for NGC 3621 and NGC 7424 out to an unprecedented extent. As a precursor to the SKA, the MeerKAT telescope combines both a high spatial resolution and a large field of view, necessary to map the extended neutral hydrogen in local galaxies. The mass models of the two galaxies were constructed for both the Dark Matter (DM) models (the pseudo-isothermal model and the Navarro-Frenk-White model) and MOND. Overall, we find that the DM models provide a better fit than MOND to the galaxies' rotation curves. Furthermore, the pseudo-isothermal model is found to be the most consistent with the observations.

2.1 Introduction

How galaxies accrete their gas and then convert that gas into stars remains one of the hot topics in the area of galaxy formation and evolution. Current star formation rates (SFRs) of nearby galaxies are, as derived from interferometer observations,

an order of magnitude higher than what can be sustained by minor mergers and accretion (Sancisi & Fraternali 2008, Kauffmann et al. 2010). This implies that local galaxies must somehow be accreting gas from the intergalactic medium (IGM).

Gas accretion from the IGM comes in two modes (Kereš et al. 2005): the "cold" mode, which dominates in low mass galaxies residing in low density and high redshift environments, and the "hot" mode predominant in high mass galaxies evolving in high density environments. Recent surveys such as The HI Nearby Galaxies Survey (THINGS; Walter et al. 2008) and the WSRT Hydrogen Accretion in Local Galaxies Survey (HALOGAS; Heald et al. 2011) have begun to solve the puzzle of gas accretion by not only studying the HI content and distribution in and around galaxies, but also by investigating the relation between the HI content and the star formation of galaxies. HALOGAS has mapped 22 disc galaxies down to a column density level of $\sim 10^{19}\mathrm{cm}^{-2}$ at spatial resolutions of a few kpc and spectral resolution of 16 km s^{-1}, an order of magnitude lower than typically found in the main HI discs. However, the survey focused on obtaining a high column density sensitivity but lacks spatial resolution. On the other hand, the THINGS survey was conducted with the VLA high spatial resolution but was limited in column density sensitivity. The challenge of the MHONGOOSE (MeerKAT HI Observations of Nearby Galaxies; Observing Southern Emitters, de Blok et al. 2018a) survey will be to combine high column density sensitivity and high spatial resolution over a large field of view, making it the first survey to benefit from this triple advantage, and that will therefore provide information on the processes driving the transformation and evolution of galaxies in the nearby universe at high resolution and also to low column densities. MHONGOOSE is a deep HI survey that will make use of the MeerKAT telescope to observe 30 nearby galaxies down to a targeted 3σ column density sensitivity of $7.5 \times 10^{18}\mathrm{cm}^{-2}$, at a resolution of $30''$ integrated over 16 km s^{-1}. At $90''$ resolution, the corresponding 3σ limit is $5.5 \times 10^{17}\mathrm{cm}^{-2}$. Several science topics will be addressed by MHONGOOSE, some of which are related to gas accretion in galaxies and the relation between the HI content and star formation in galaxies. In effect, one of the goals of the survey consists of showing how the low column density gas is connected with the cosmic web, and where gas accretion occurs.

Before the MeerKAT telescope is ready to conduct the full survey, it is essential to use existing telescopes to get a first characterisation of the candidate galaxies. In the present work, we use the Karoo Array Telescope (KAT-7; Carignan et al. 2013) and the Green Bank Telescope* (GBT, Prestage et al. 2009) to conduct the

*GBT is a facility of the U.S.A National Science Foundation operated under cooperative agreement by Associated Universities, Inc.

early observations of the MHONGOOSE sample. As an engineering testbed for the MeerKAT telescope, KAT-7 is an extremely compact array of seven 12m-diameter antennas, with baselines ranging from 26 m to 185 m. These short baselines of the telescope and its large primary beam of $\sim 1^\circ$ make it suitable to map the low column density structures. As for the GBT, the 100m diameter and excellent surface brightness sensitivity of the single-dish telescope give it the ability to survey the diffuse HI environments typically undetected by most interferometers; the telescope has been used regularly to detect low column density structures around galaxies (e.g, Chynoweth et al. 2008; 2009, Lockman et al. 2012, Wolfe et al. 2013, Pisano 2014).

The MeerKAT telescope is designed such that, at full capacity, it should reach a dynamic range of 1:10^4 in spectral line mode; the telescope will be able to detect structures at $\sim 10^{17}\,\mathrm{cm}^{-2}$ in the presence of $\sim 10^{21}\,\mathrm{cm}^{-2}$ emission. Because of this high dynamic range, it is essential to select suitable calibrators – calibrators that will cause the least errors in the flux and/or the phase of the targets – to optimise the quality of the observations with the telescope. Also, with the initial 16-antenna release of MeerKAT, one can test the capability of the upcoming full array by conducting science observations of nearby HI-rich galaxies.

The paper is organised as follows: we begin with a description of the MHONGOOSE sample in Section 2.2. The observations with the KAT-7, GBT and MeerKAT telescopes as well as the data reduction are discussed in Section 4.2, and the derived HI properties of the observed galaxies are given in Section 4.3. The rotation curves of NGC7424 (observed with KAT-7) and NGC 3621 (observed with MeerKAT) are derived in Section 4.4, and Section 4.4.4 provides a study of the mass (luminous and dark) distribution. Finally in Section 2.7, we summarise the main results of the work and discuss them.

2.2 Sample

The MHONGOOSE galaxies were selected based on their membership to both the HIPASS (HI Parkes All Sky Survey, Meyer et al. 2004) catalogue and the SINGG (Survey for Ionization in Neutral Gas Galaxies, Meurer et al. 2006) survey. These are galaxies with HIPASS flux higher than 50 mJy, having a galactic latitude $|b| > 30^\circ$ and a Galactic standard of rest velocity > 200 km s^{-1}. Further constraint was put on the declination ($\delta < -10^\circ$) and the distance (< 30 Mpc) to ensure that the physical resolution is comparable to that of the THINGS survey. This resulted in a sample of 88 galaxies that were later divided in 6 bins of $\log(\mathrm{M_{HI}})$, and 5 galaxies of various inclinations were selected in each bin: edge-on, face-on galaxies and galaxies

Object	R.A	Dec.	Type	B mag.	D (Mpc)	Tel.
(1)	(2)		(3)	(4)	(5)	(6)
ESO 300-G014.	03 09 37.8	-41 01 50	SABm	12.76	12.9	K/G
ESO 300-G016[a]	03 10 10.5	-40 00 11	IAB	15.57	9.3	G
ESO 302-G014.	03 51 40.9	-38 27 08	IBm	14.59	11.7	G
ESO 357-G007[b]	03 10 24.3	-33 09 22	SBm	14.61	17.8	G
IC 4951	20 09 31.8	-61 51 02	SBdm	13.61	11.2	K
KK98-195[a]	13 21 08.2	-31 31 45	I	17.17	5.2	G
KKS2000-23[a] ..	11 06 12.0	-14 24 26	I	15.80	12.7	G
NGC 0625.....	01 35 04.6	-41 26 10	SBm	11.59	4.1	K
NGC 1371.....	03 35 01.3	-24 56 00	SABa	11.41	20.4	G
NGC 1592.....	04 29 40.1	-27 24 31	Pec	14.38	13.0	G
NGC 3511.....	11 03 23.8	-23 05 12	SAc	11.36	14.2	G
NGC 3621[c]....	11 18 16.5	-32 48 51	SAd	10.16	6.6	M
NGC 5068.....	13 18 54.8	-21 02 21	SABcd	9.93	6.9	G
NGC 5170[b]....	13 29 48.8	-17 57 59	SAc	11.54	28.0	G
NGC 7424.....	22 57 18.4	-41 04 14	SABcd	10.69	13.6	K
NGC 7793.....	23 57 49.8	-32 35 28	SAd	9.61	3.9	K
UGCA 015	00 49 49.2	-21 00 54	IBm	14.99	3.3	G
UGCA 250	11 53 24.0	-28 33 11	Sd	12.75	24.4	G
UGCA 307	12 53 57.3	-12 06 21	IBm	13.99	8.6	G
UGCA 320	13 03 16.7	-17 25 23	IBm	13.07	7.7	G

Table 2.1: Total sample of galaxies observed. This includes the MHONGOOSE galaxies observed with KAT-7 and GBT, plus NGC 3621 observed with MeerKAT. Column (1): Object name; Column (2): J2000 optical position from NED; Column (3): Morphological type from the RC3 catalogue; Column (4): The B_j-band magnitude from Doyle et al. (2005); Column (5): Distance of the galaxy in Mpc from Meurer et al. (2006); Column (6): Telescope used for observation: K=KAT-7, G=GBT, M=MeerKAT. Notes: [a] Morphological type and total B-magnitude from HyperLEDA, [b] distance from Sorce et al. (2014), [c] distance from (Freedman et al. 2001).

of intermediate inclination ($50° - 60°$) were chosen. The latter inclination is optimal for kinematical modelling. A more complete description of the sample selection is given in de Blok et al. (2018a).

Five of the 30 MHONGOOSE galaxies were observed with KAT-7. We observed fifteen of the remaining galaxies (plus one already observed with KAT-7) with the GBT, which brings our total sample size to 20 galaxies.

On top of the MHONGOOSE sample, the galaxy NGC 3621 was also observed with the MeerKAT telescope as part of commissioning observations. The total sample is listed in Table 2.1.

2.3 Observations

2.3.1 KAT-7 observations and reduction

The KAT-7 observations were conducted between late 2014 and early 2015, and three different phase calibrators were observed for each galaxy. The observing times are summarised in Table 2.2, and the correlator mode used provided a total bandwidth of 12.5 MHz over 4096 channels, which corresponds to a velocity resolution of about 0.65 km s^{-1}. The observation technique consists in alternating between the target and a phase calibrator about every 20 min to calibrate the phase stability, and observe the flux calibrator two or three times per session. Given the large primary beam of the telescope ($\sim 1°$), a single pointing was sufficient to individually cover the galaxy candidates.

The complete data reduction was performed with the MIRIAD package (Sault et al. 1995), and the procedure followed is similar to the standard WSRT data reduction. However, since the KAT-7 telescope specifications are not implemented in MIRIAD, special care was taken to manually input, upon importing the data, some parameters such as the FWHM (58′), the system temperature (26 K), the telescope gain (37.5 Jy K^{-1}) and the HI rest frequency (1420.4 MHz). Furthermore, we performed a spectral and time averaging over 4 channels and 20 min respectively, to improve the signal-to-noise ratio of the data. This brings the total number of channels down to 1024 and the spectral resolution to 2.6 km s^{-1}. Because KAT-7 is an engineering testbed telescope, not all the RFI (Radio Frequency Interference) sources are known since the monitoring was still ongoing during the observations. So the RFI inspection had to be manually done to remove potential artifacts from the data, including the effects of Galactic HI on low velocity sources. The observing sessions were individually reduced and for each session a second order polynomial fit over line-free channels was used to perform continuum subtraction in the *uv* plane using the MIRIAD's task UVLIN. The emission from the galaxies typically spans less than 100 channels, providing a large number of line-free channels for the baseline fits. We then proceeded to correct the velocity coordinates of the continuum-subtracted *uv* data with the CVEL task in AIPS (Greisen 2003). This is because KAT-7 does not use Doppler tracking and, as mentioned before, the MIRIAD package does not contain the telescope's parameters. The resulting datasets for a source's individual sessions were then combined and a datacube was produced with a *natural* weighting.

To determine the best calibrators for the different sample galaxies, the process described above was repeated for each and every calibrator source. An ideal calibrator source can be approximated as a point source to the telescope. The selection of

the best calibrators is based on their brightness and structure: the sources have to be bright and not confused, and also should not be at large angular distance from the target. In the data, these criteria result in the following:

- the source must provide the least rms noise in the calibrated data cube of the target (the reference for the rms value being the theoretical noise),
- the scatter in the calibrator's phase vs amplitude graph for the best source must be the least.

The second criterion is to ensure that the source has the least variation both in phase and amplitude. To conduct a meaningful comparison between the flux calibrators, data with the same amount of observing time were considered. In Table 2.2 we list the best flux and phase calibrators, as well as the total observing time for each of the five targets considered. To illustrate the effects of the choice of the phase calibrators on the target source, we present in Fig. 2.1 the channel maps of the NGC 625 data cubes calibrated with two different phase calibrators: 0039-445 and 0201-440. This is the most extreme case amongst the galaxies in the sample of five, where we notice a large difference in the end products with different calibrators although the same calibration scheme was used. Fig. 2.1 also clearly demonstrates that we obtain a much higher signal-to-noise ratio (SNR) with the calibrator 0201-440.

Self-calibration

A drawback of the KAT-7's large field of view is mostly noticed when observing calibrators. Ideally one would want to have only the compact calibrator source in the field. However, this is not easily achieved when the FWHM is as wide as it is for KAT-7. In effect, unwanted secondary sources in the calibrators' field are likely to affect the phase variation of the data. Because of this, the observed spectra of the visibilities are not flat. As a result, assuming a point source for deriving the bandpass introduces ripples in the bandpass calibration. To solve the phase stability problem, we applied a self-calibration on the calibrator source. It consists of CLEANing a dirty map of the source previously produced with the INVERT task in MIRIAD; the output cleaned component is in turn used as a model with the SELFCAL task. To illustrate the effect of the self-calibration, we show in Fig. 2.2 the variation of phase of the calibrator source 0039-445 as a function of the baseline, after standard calibration (left panel) and after self-calibration (right panel). Although the standard calibration significantly reduces the scatter in the source's phase – the standard deviation in the phase goes from 99.3° to 15.5° – one does not quite achieve a stable phase throughout

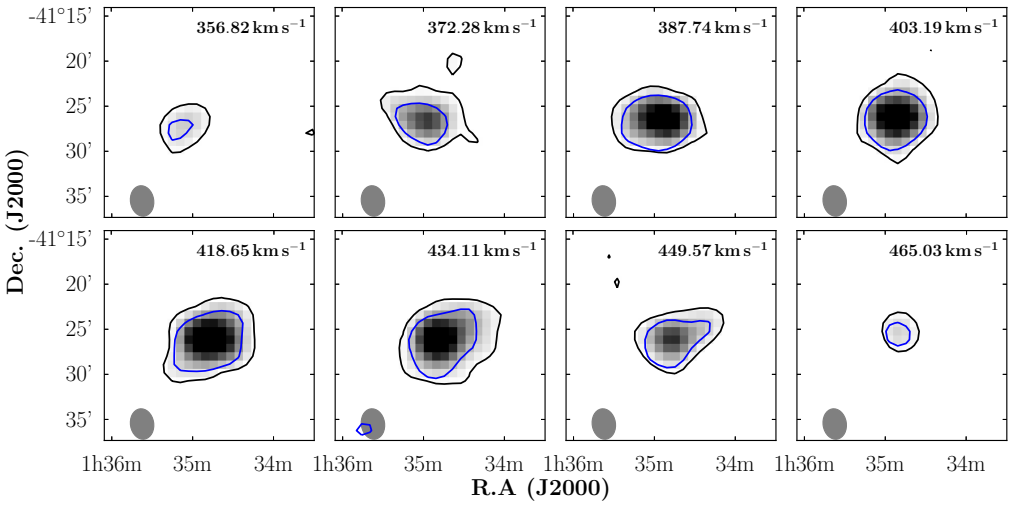

Figure 2.1: Channel maps of NGC 625 from two different cubes, obtained with two different phase calibrators: 0201-440 (*grayscale and black contours*) and 0039-445 (*blue contours*). The channels are sampled at 15.46 km s^{-1}, and both the black and blue contours are taken at the same flux level, 0.02 Jy $beam^{-1}$. The synthesised beam of the data is represented by an ellipse in the lower left of each panel.

the probed baseline. However, in the right panel of the figure, all the visibility points lie around the 0° phase.

2.3.2 GBT observations and reduction

The GBT telescope was used as an alternate instrument to observe the rest of the sample galaxies after KAT-7 became unavailable. Out of the 25 remaining galaxies, a total of 16 observable from the GBT were selected for mapping. The sample of 16 was observed in 2016 during 55 observing sessions* and for each session, an area of $2° \times 2°$ around each galaxy was observed for 10 hours, requiring a total observing time of 160 hours for the whole sample. The observational technique used is similar to that of Pisano (2014). The observations were done with the L-band receiver and the VEGAS spectrometer, using a 23.4 MHz bandwidth at 0.7 kHz resolution and a frequency switching at ±2.5 MHz. The primary flux calibrator source used during the individual sessions was either 3C48, 3C147 or 3C295 and the $T_{\rm cal}$ values determined for the noise diode were constant throughout individual sessions varied between 1.5 K and 1.7 K (with an average of 1.66 ± 0.03 K) from one session to another, for both the XX and the YY polarisations. This dispersion in $T_{\rm cal}$ corresponds to a flux

*As part of the project GBT16B-212

Galaxy	Flux cal. (best cal. *)	Observing time (h) Total	On source	Best phase cal.
NGC 625	0407-658*	11.2	8.3	0201-440
	PKS 1934-638	13.2	11.1	
ESO 300-G014	0407-658*	13.5	6.4	0220-349
	3C138	4.5	3.0	
IC 4951	PKS 1934-638*	22.7	22.4	PKS 1934-638
NGC 7424	0407-658	12.9	6.7	2259-375
	PKS 1934-638*	14.0	9.2	
NGC 7793	0407-658	13.0	7.4	0008-421
	PKS 1934-638*	15.1	8.7	

Table 2.2: Observing time spent on each of the KAT-7 sample galaxies. These are estimated after flagging

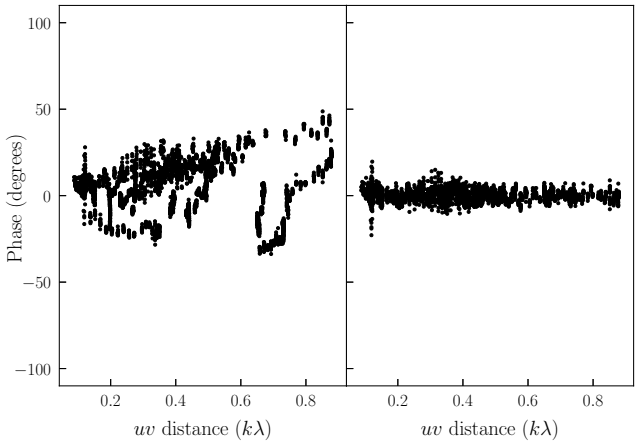

Figure 2.2: Phase variation of the calibrator source 0039-445 observed with the KAT-7, before (*left*) and after (*right*) applying self-calibration.

Parameter	KAT-7	GBT	MeerKAT
Weighting function	natural	–	robust = 0
Channel width (km s^{-1})	2.6	6.4	11.2
FWHM of beam	$\sim 3.5' \times 3.2'$	$9.1'$	$1.9' \times 1.2'$
Pixel size	$55'' \times 55''$	$105'' \times 105''$	$15'' \times 15''$
Map size	$3.9^\circ \times 3.9^\circ$	$2^\circ \times 2^\circ$	$\sim 2^\circ \times 2^\circ$
RMS noise (mJy beam^{-1})	7.0	10	1.7
$N_{\rm HI}$ ($1\sigma \times 10^{18}$ cm^{-2}, over 16.5 km s^{-1})^a	3.2	0.59	3.8

Table 2.3: Summary of the KAT-7, GBT and MeerKAT image cubes. The channel width listed for the MeerKAT data cube is the width obtained after Hanning-smoothing. Note: ^{a} the $N_{\rm HI}$ limit is assuming that any emission completely fills the beam.

uncertainty of 2%.

The frequency-switched spectra obtained after each observing session were individually reduced using GBTIDL* where a third-order polynomial fit was applied to the line-free regions of the spectra to remove residual baseline structures and potential continuum sources. The reduction was done with the same script as in Pingel et al. (2018). The data were then flagged to remove recurrent RFIs at $\sim$ 1416 MHz. The flagged data were then smoothed to a 6.4 km s^{-1} resolution using a boxcar kernel, and exported into AIPS via IDLTOSDFITS† where they were combined by source, before being imaged into data cubes. For most sources, the baseline subtraction did not succeed to completely remove the strong continuum sources in the field. For these, an additional continuum subtraction was performed using a fourth-order polynomial with the AIPS task XBASL.

The typical noise achieved per galaxy candidate is $\sigma \sim 20$ mK over 6.4 km s^{-1}, equivalent to 2.3×10^{17} cm^{-2} assuming optically thin emission. This corresponds to a flux sensitivity of $\sigma \sim 10$ mJy/beam, or a 5σ HI mass detection limit of $M_{\rm HI} = 4.7 \times 10^5\, d^2\, {\rm M}_\odot$ for a 20 km s^{-1} line width source at a distance d Mpc.

*http://gbtidl.nrao.edu/
†https://safe.nrao.edu/wiki/bin/view/GB/Data/IdlToSdfits

2.3.3 MeerKAT commissioning observations of NGC 3621

As of April 8th 2017, date of NGC 3621's observations, only half of the 32 then completed MeerKAT's antennas were available since the ROACH2 correlator then used was limited to a total of 32 inputs (see Camilo et al. 2018, for a description of MeerKAT). The observations were made as part of MeerKAT commissioning activities, and were not taken as part of MHONGOOSE. Two polarisations were used from each of the 16 antennas, which were chosen to give the best collection of shortest baselines available. Besides the high column density sensitivity and resolution of the telescope ($1.9' \times 1.2'$ as used), what makes it suitable for detecting extended HI features is its large field of view of $\sim 1°$. NGC 3621 has an optical size of $12.3' \times 7.1'$, which required no more than one MeerKAT pointing to map its HI distribution. The observations were conducted on the evening and at night for 8.2 hours in total, and made use of 1117-248 as complex gain calibrator and the sources PKS 0408-65 and PKS 1934-638 as flux and bandpass calibrators. The observation process is similar to KAT-7's, with the bandpass calibrator observed for 10min every hour during the observation, and the complex gain calibrator observed for 2min after every 5min with a dump rate of 4 seconds. The observations were performed with the 32k correlator mode, which has 32,768 channels over a total bandwidth of 856 MHz covering the frequency range of 856 MHz to 1712 MHz. This gives a channel width of 26.1 kHz (5.6 km s^{-1}).

Overall, after flagging, the total observing time of the target is 253 mins, that of the flux calibrators is 73 mins, while the phase calibrator received 110 mins. The data were reduced with MIRIAD following the same procedure as the KAT-7 data. In general, the MeerKAT data cannot be reduced with MIRIAD because of the *w*-projection algorithm not being available in the package. However, the *w*-projection is only necessary when the observations are affected by the *non-coplanar baselines* effect, which happens when the Fresnel number, defined as $N_F = D^2/B\lambda$ (where D is the antenna diameter, B the maximum baseline and λ the observing wavelength), is $N_F < 1$ (Cornwell et al. 2008). In the case of the MeerKAT observations, the baseline length at which $N_F < 1$ is 868m, which is larger than the maximum baseline of 715m of the array as used. This means that the non-coplanar effects are negligible, and *w*-projection can be ignored.

2.4 HI properties

2.4.1 HI Distribution

We present in Fig. 2.3 the HI column density maps of four of the five galaxies observed with the KAT-7, overlaid on optical DSS images. For the galaxy NGC 7424, for which we present a kinematical study in Section 4.4, we show the column density map and velocity field in Fig. 2.4. Fig. 2.5 (left panel) contains its radial HI surface density profile, obtained with the GIPSY's task ELLINT. The axial ratio of the ellipses used in ELLINT were determined by the optical inclination of the galaxy (see Table 2.4), and their orientation is determined from the galaxy's velocity field. In Table 2.4 we list the HI fluxes and masses of all observed galaxies, as derived from the observations. We also list, for comparison, the HIPASS HI fluxes of the galaxies as reported in Koribalski et al. (2004), Doyle et al. (2005) and Kobulnicky & Skillman (2008). The HI mass, HI diameters measured at the $10^{19}\,\mathrm{cm}^{-2}$ column density level and optical diameters measured at the 25th magnitude (from the RC3 catalogue; de Vaucouleurs et al. 1991) are also presented. Several authors (e.g. Broeils & Rhee 1997, Staveley-Smith et al. 2003, Noordermeer et al. 2005, Wang et al. 2014, Koribalski et al. 2018) estimate the HI diameter at a surface density level of $1\,\mathrm{M}_\odot\,\mathrm{pc}^{-2}$ (corresponding to $1.25 \times 10^{20}\mathrm{cm}^{-2}$), which is smaller than the diameter at $10^{19}\,\mathrm{cm}^{-2}$. However, as is noted in Serra et al. (2012b, for early type galaxies) and Wang et al. (2016), a significant fraction of HI mass is generally found outside the diameter defined at $1\,\mathrm{M}_\odot\,\mathrm{pc}^{-2}$. This makes the diameter at $10^{19}\,\mathrm{cm}^{-2}$ more representative of the full extent of the HI disc, as is further seen in Fig. 2.5. For each of the galaxies, except UGCA 319, the recovered KAT-7 flux is comparable to that of the HIPASS; also, the HI envelope is, as expected, more extended than their optical disc, as shown by their HI to optical diameter ratio listed in column (10) (see Broeils & Rhee 1997). For UGCA 319, the measured flux is ~ 3 times lower than the reported HIPASS flux, likely due to the close proximity of the galaxy to UGCA 320. Indeed, the angular separation between the two galaxies is $\sim 0.31°$, barely larger (about 1.3 times) than the Parkes resolution and only ~ 2.1 times the GBT resolution. One therefore expects the two sources to be confused in the HIPASS (and even GBT) observations, making it difficult to accurately measure their individual fluxes. This is further seen when comparing the total line flux of the two galaxies in both observations: we obtain 126.4 ± 0.7 Jy km s^{-1} in the GBT data, comparable to 121.6 Jy km s^{-1} from the HIPASS data. Moreover, the Parkes flux of UGCA 320, as reported in Pisano et al. (2011), is 107.3 ± 0.3 Jy km s^{-1}, about $\sim 12\%$ lower than the value derived in the present work. The total HI intensity maps of the GBT

data are presented in Chapter A.

2.4.2 NGC 3621

The HI line flux of NGC 3621, as measured from the MeerKAT data, is 877 ± 14 Jy km s^{-1}. This is in agreement with the LVHIS (Local Volume HI Survey; Koribalski et al. 2018) flux of 856.8 Jy km s^{-1} measured with the ATCA and 29% higher than the THINGS measurement of 679 Jy km s^{-1} with the VLA. The difference with the VLA measurement is not surprising given the limited field of view and column density sensitivity of the THINGS observations. In effect, the total HI intensity map presented in de Blok et al. (2008) does not cover the full HI extent of the galaxy, but only the inner $\sim 25'$. On the other hand, although the field of view of the ATCA telescope is similar to that of the VLA, the LVHIS observations of NGC 3621 consist of a mosaic of several fields to ensure that the full extent of the galaxy's HI disc was covered. In Fig. 2.6 we present a comparison of the global profiles of the galaxy as obtained from the MeerKAT, THINGS and LVHIS observations, respectively. While the profiles obtained with MeerKAT and ATCA are comparable, it is obvious that VLA misses much of the galaxy's flux. This is consistent with the flux values derived for the three observations. The total HI intensity map, velocity field and velocity dispersion maps are presented in Fig. 2.7: a region of high velocity dispersion is seen South-East of the nucleus. The different morphologies of the northern and southern sides of the disc imply that the galaxy does not have a nicely rotating disc, but is warped in the line-of-sight (this was also seen in the THINGS data, de Blok et al. 2008), and there could be a cloud-like structure located on the receding side of the galaxy. We also present, in Fig. 2.5, the radial distribution of its HI surface density. As discussed in Section 2.4.1, the profile of the galaxy shows that the HI diameter captures almost all the detected HI, unlike the $1\,M_\odot\,pc^{-2}$ isophote diameter which is approximately equal to the optical diameter of the galaxy.

2.4.3 Search for HI clouds

The MHONGOOSE galaxies were selected to exclude strongly interacting galaxies, and dense group and cluster environments, to minimise the gas contribution of companion galaxies. This way, the contribution of the cold gas accretion should be more apparent.

We searched, in the whole observed sample, for HI clouds associated with the galaxies that may be signs of gas accretion. However, none of the candidates present such structures down to a 3σ level (for any emission that fills the beam) of $\sim 2.2 \times 10^{18}\,cm^{-2}$ over a 20 km s^{-1} line width, with a beam size of $9.1'$. However, the

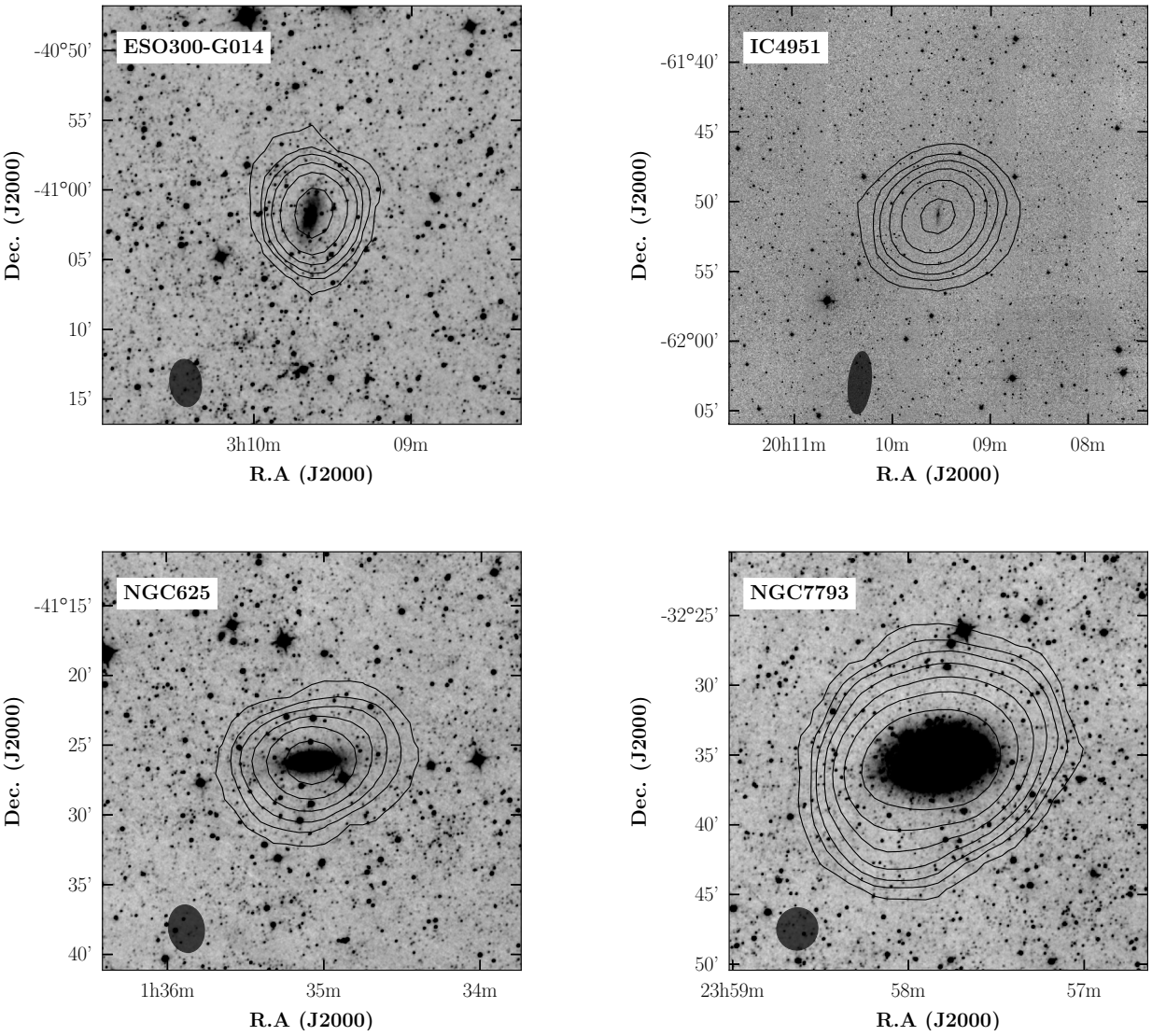

Figure 2.3: Column density maps of four of the KAT-7 galaxies overlaid on their *WISE* W1 images: ESO 300-G014 (*top left*), IC 4951 (*top right*), NGC 625 (*bottom left*) and NGC 7793 (*bottom right*). The contour levels are 0.5, 1.0, 2.0, 4.0, $\ldots \times 10^{19}\,\mathrm{cm}^{-2}$. The KAT-7 synthesised beam is shown as an ellipse at the bottom left of each panel.

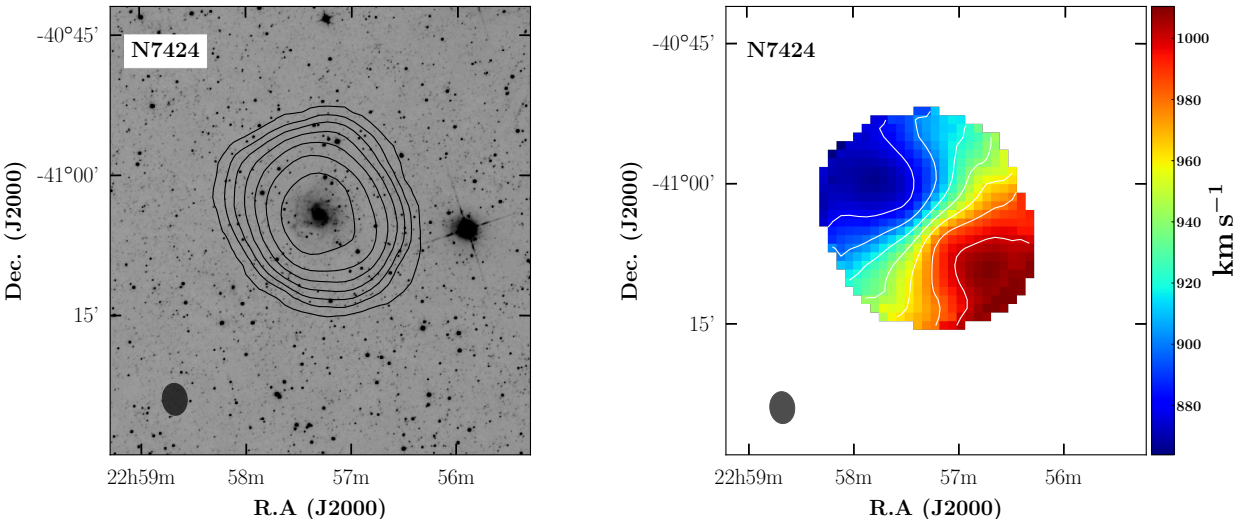

Figure 2.4: KAT-7 HI column density map (*left*), and velocity field (*right*) of NGC 7424. The contours of column density are 0.5, 1.0, 2.0, 4.0, ... $\times 10^{19}$ cm^{-2}, those of the velocity are 880, 900, 920, ..., 1000 km s^{-1}.

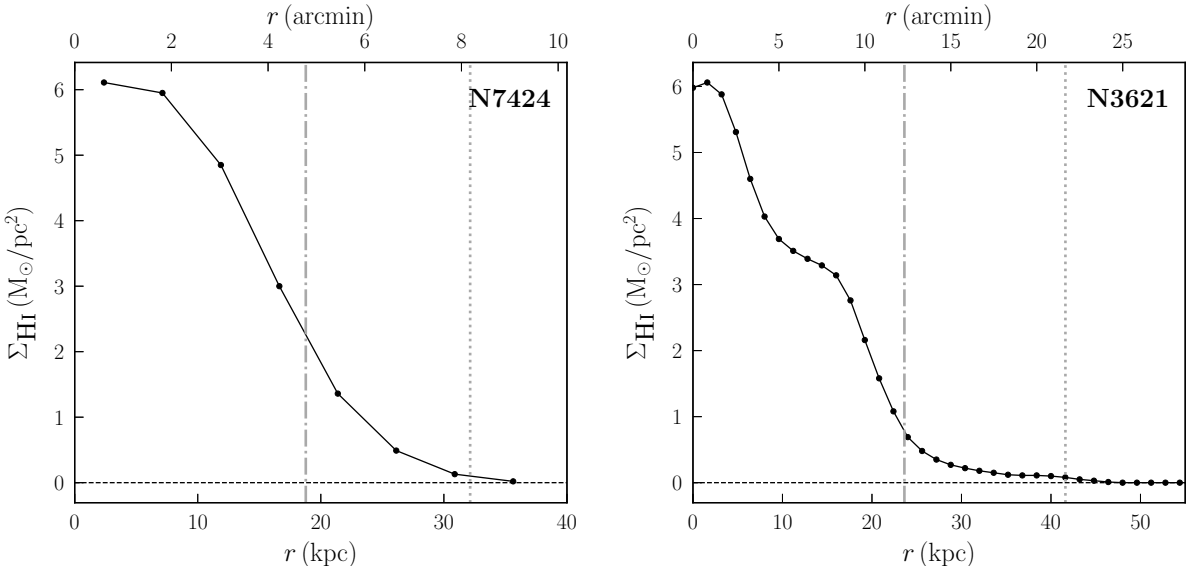

Figure 2.5: Radial distribution of the HI surface density of NGC 7424 (*left*) and NGC 3621 (*right.*). The *gray dashdot* and *dotted* lines show respectively the RC3 optical 25th magnitude and HI (10^{19} cm^{-2} column density level) radii. The optical and HI diameters of NGC 7424 are listed in Table 2.4 and those of NGC 3621 are $d_{25} = 24.6'$ and $d_{\rm HI} = 43.3'$ respectively.

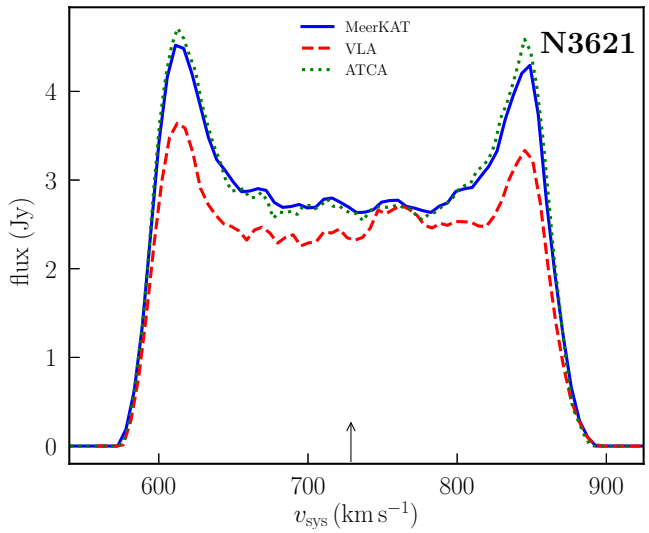

Figure 2.6: Comparison of the global profiles of NGC 3621 as derived from the MeerKAT (*blue line*), VLA (*red dashed line*) and ATCA (*green dotted line*) data cubes. The systemic velocity of the galaxy is marked by an upward arrow.

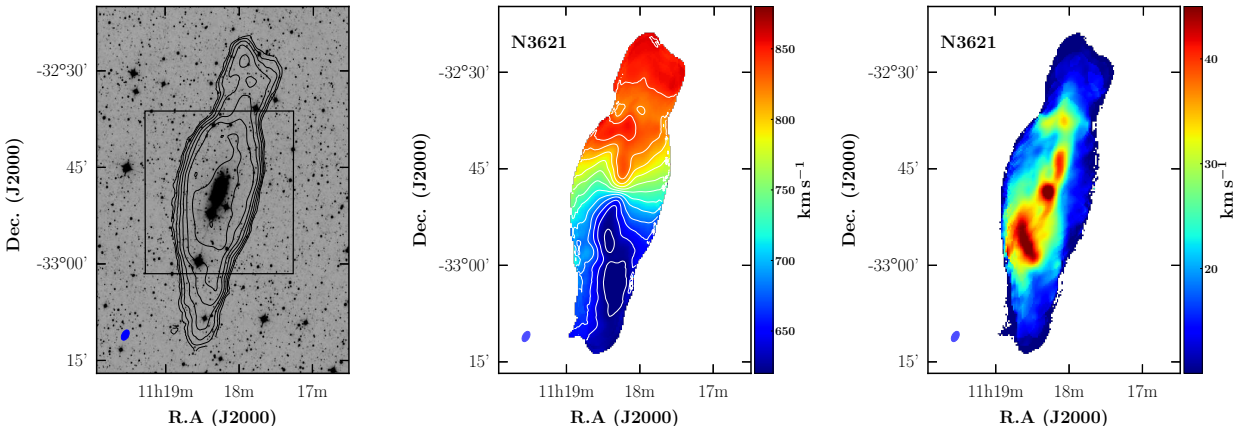

Figure 2.7: MeerKAT maps of NGC 3621. *Left:* column density contours overlaid on the W1 grayscale map. The contours are $0.1, 0.2, 0.4, ..., 12.8 \times 10^{20}$ cm^{-2}, and the rectangle represents the approximate spatial size of the THINGS data. *Middle:* velocity field of the galaxy. Contours are $600, 620, 640, ..., 900$ km s^{-1}. *Right:* velocity dispersion map of the galaxy.

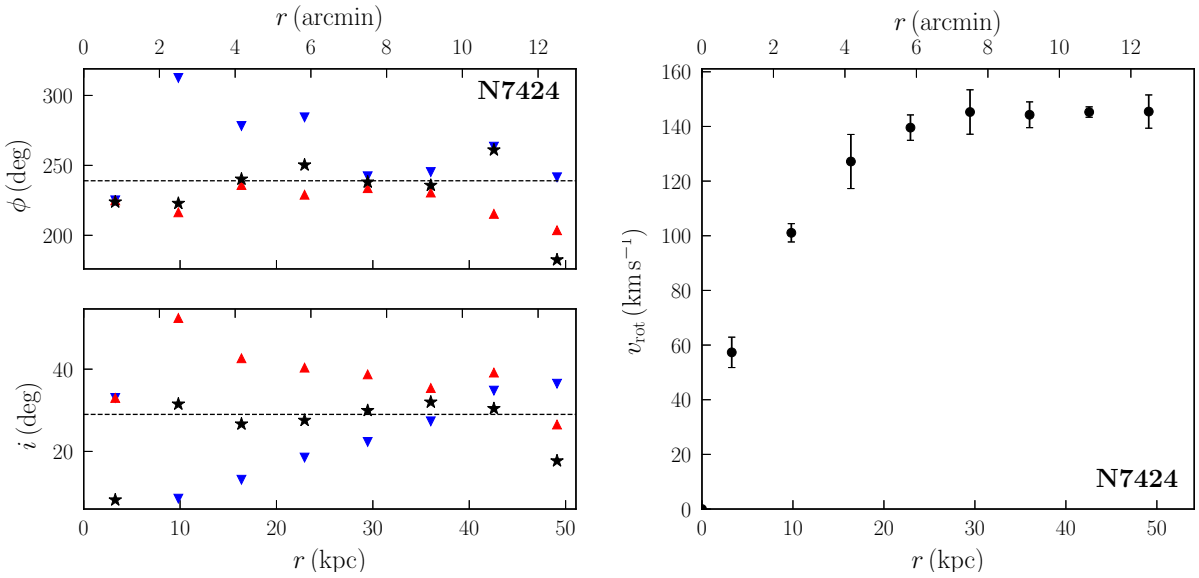

Figure 2.8: The tilted-ring model (*left*) and rotation curve (*right*) of NGC 7424. The blue and red triangles represent respectively the data points for the approaching and receding sides, while the black stars show the points for both sides combined. The *dashed* horizontal lines on the left panels indicate the adopted values for the position angle and inclination, respectively.

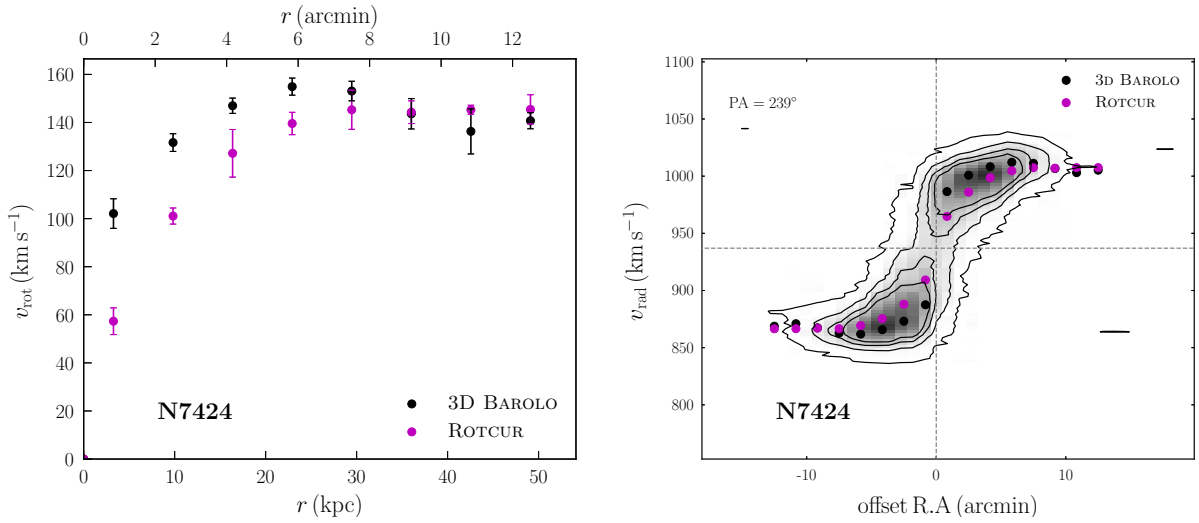

Figure 2.9: Rotation curves of NGC 7424. *Left:* comparison of the Rotcur and 3D Barolo rotation curves. *Right:* overlay of the derived rotation curves on the PV diagram of the galaxy taken along its major axis.

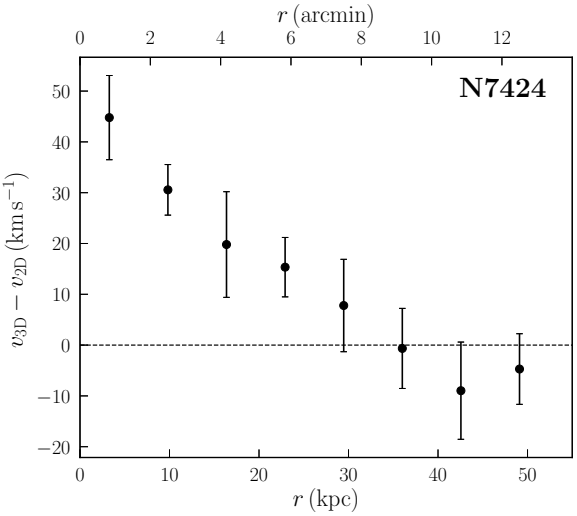

Figure 2.10: Difference between the rotation curves of NGC 7424 obtained using ROTCUR (v_{2D}) and 3D BAROLO (v_{3D}). The difference is highest at the centre and decreases to around zero in the outer regions.

particular case of suspected cloud near the galaxy UGCA 250 caught our attention; a cloud-like structure was seen but could not be confirmed due to artefacts in which it was embedded. The structure was located south-west of the galaxy, in a region of the data that was affected by RFIs and where the noise was higher. We then re-observed the galaxy at night (to avoid solar interferences) and the analysis of the new data showed that the structure is in fact an artefact, as we did not detect anything above 3σ at its position (see Fig. A.14).

Galaxy	v_{sys} (km s^{-1})	W_{50} (km s^{-1})	i (deg)	S_{HI} (Jy km s^{-1})	S_{HIPASS} (Jy km s^{-1})	M_{HI} (10^8 M$_\odot$)	d_{HI} (arcmin)	d_{25} (arcmin)	d_{HI}/d_{25}	Tel. (K/G)
(1)	(2)	(3)	(4)	(5)	(6)	(7)	(8)	(9)	(10)	(11)
ESO 300-G014	955.0	127.7	61.2	25.8 ± 0.6	25.6	10.1 ± 0.2	12.10	5.01	2.41	K
.....	954.5	126.9	...	25.9 ± 0.5	...	10.1 ± 0.2	15.75	...	3.14	G
ESO 300-G016	710.1	30.2	35.6[a]	2.9 ± 0.2	4.3	0.6 ± 0.1	< 9.0	0.71[a]	<12.68	G
ESO 302-G014	871.4	70.0	27.6	10.4 ± 0.4	11.1	3.3 ± 0.1	12.38	1.70	7.28	G
ESO 302-G009[b]	989.8	146.0	78.9	11.8 ± 0.6	13.9	10.7 ± 0.5	11.80	2.34	5.04	G
ESO 357-G007	1113.8	123.2	72.0	8.9 ± 0.3	11.0	6.4 ± 0.2	12.25	2.34	5.23	G
IC 4951	813.0	119.2	90.0	26.1 ± 0.4	24.6	7.8 ± 0.1	11.81	2.75	4.29	K
KK98-195	570.1	25.2	55.7[a]	6.0 ± 0.2	5.6	0.4 ± 0.0	10.21	0.45[a]	22.69	G
KKS2000-23...	1039.0	78.0	90.0[a]	11.1 ± 0.4	11.1	4.2 ± 0.1	15.05	3.47[a]	4.34	G
NGC 0625.....	396.0	71.6	74.4	34.5 ± 0.4	31.2	1.3 ± 0.0	13.71	5.75	2.38	K
NGC 1371.....	1460.5	382.6	47.5	71.2 ± 1.0	69.9	69.5 ± 1.0	22.28	5.62	3.96	G
NGC 1385[b]....	1493.6	182.4	55.6	27.4 ± 0.6	29.3	4.0 ± 0.1	15.75	3.39	4.64	G
NGC 1592.....	943.8	50.8	64.4	2.7 ± 0.2	5.9	1.1 ± 0.1	< 9.0	1.41	<6.38	G
NGC 3511.....	1117.5	257.9	72.6	69.7 ± 1.0	87.5	33.1 ± 0.5	19.25	5.75	3.35	G
NGC 3513[c]....	1194.5	92.1	38.3	7.1 ± 0.3	29.3	1.0 ± 0.1	< 9.0	2.82	<3.19	G
NGC 5068.....	667.0	69.3	30.1	177.0 ± 0.7	129.4	19.8 ± 0.1	24.88	7.24	3.44	G
NGC 5170.....	1497.6	508.9	90.0[a]	96.9 ± 1.2	74.1	222.2 ± 2.7	23.55	8.32	2.83	G
NGC 5253[d]....	406.6	62.6	70.1	49.2 ± 0.6	43.9	1.5 ± 0.0	20.48	5.01	4.09	G
NGC 7424.....	939.0	155.1	32.4	269.0 ± 1.3	250.2	116.5 ± 0.6	16.36	9.55	1.71	K
NGC 7793.....	227.0	176.0	48.8	274.2 ± 1.2	280.5	9.9 ± 0.1	20.85	9.33	2.23	K
UGCA 015....	295.5	31.9	67.4	3.3 ± 0.2	3.7	0.1 ± 0.0	< 9.0	1.70	<5.29	G
NGC 0247[b]....	156.2	199.2	74.9	741.4 ± 1.1	...	19.0 ± 0.0	40.57	21.38	1.90	G
UGCA 250....	1703.1	274.7	90.0[a]	86.9 ± 1.1	70.9	121.8 ± 1.5	21.66	4.36	4.97	G
UGCA 307....	822.8	72.3	62.0	26.9 ± 0.4	26.6	4.7 ± 0.1	17.50	2.00	8.75	G
UGCA 320....	740.9	109.2	90.0[a]	122.7 ± 0.7	93.9	17.3 ± 0.1	22.82	5.62	4.06	G
UGCA 319[bc]..	757.3	87.6	50.0	3.7 ± 0.2	27.7	3.4 ± 0.2	< 9.0	1.62	<5.55	G

Table 2.4: Properties of the galaxies in the KAT-7 and GBT samples. The parameters of NGC 3621, which is neither part of the MHONGOOSE sample nor a secondary source, are given in Section 2.4.2 instead. Column (1): Galaxy name; Column 2: Systemic velocity derived from the HI global profile; Column (3): HI profile width at 50% of the peak intensity; Column (4): Optical inclination from the RC3 catalogue (de Vaucouleurs et al. 1991); Column (5): Measured HI integrated flux; Column (6): HIPASS flux (Doyle et al. 2005); Column (7): Derived HI mass; Column (8): Measured HI diameter. An upper limit of 9′ was used as the HI diameter of the GBT galaxies smaller than the GBT beam; Column (9): optical diameter at measured at the 25th magnitude from the RC3 catalogue; Column (10): HI to optical diameter ratio; Column (11): Telescope used for observation: K=KAT-7, G=GBT. Notes: [a] Value from HyperLEDA (Makarov et al. 2014); [b] Source is secondary, not part of the MHONGOOSE sample; [c] HIPASS flux from Koribalski et al. (2004); [d] HIPASS flux from Kobulnicky & Skillman (2008).

2.5 HI kinematics of NGC 7424 & NGC 3621

2.5.1 NGC 7424

NGC 7424 is a late-type, moderately barred face-on galaxy hosting numerous ultra-luminous X-ray sources (e.g. Soria et al. 2006) and the supernova 2001ig (Chandra et al. 2002). The HI mass of the galaxy as measured from the KAT-7 data is $\log(M_{HI}/M_\odot) = 10.1$ and, using its *WISE* W1 photometry, we derived a stellar mass of $\log(M_\star/M_\odot) = 9.4$ based on Cluver et al. (2014). These values show that the galaxy is gas-dominated, in agreement with its local environment: it is a field galaxy residing in the vicinity of the IC 1459 group (e.g. Serra et al. 2015) where gas stripping mechanisms are not as pronounced as in, for example, dense galaxy clusters where galaxies present smaller HI gas fractions (see Sullivan et al. 1981, Haynes et al. 1984, Solanes et al. 2001, Serra et al. 2012b).

Rotation curve

We proceeded to derive the rotation curve of NGC 7424 using the implementation of the tilted ring model in the GIPSY task ROTCUR (Begeman 1989). The method assumes that the gas component of the galaxy is in circular motion, and uses a set of concentric rings to describe its rotation. Each ring is characterised by a fixed value of the inclination i, the position angle ϕ (measured counter-clockwise from North to the receding major axis of the galaxy), the systemic velocity v_{sys} and the rotational velocity v_{rot}. For a given ring, the line-of-sight velocity at any point of coordinates (x, y) a distance R from the centre of the galaxy can be written

$$v(x, y) = v_{sys} + v_{rot} \sin i \cos\theta \tag{2.1}$$

where θ is the azimuthal angle in the plane of the galaxy, and can be expressed as

$$\cos\theta = (1/R)\,[-(x - x_0)\sin\phi + (y - y_0)\cos\phi]\,, \tag{2.2a}$$

$$\sin\theta = (1/R\cos i)\,[-(x - x_0)\cos\phi - (y - y_0)\sin\phi]\,. \tag{2.2b}$$

We choose the size of the ring such that we have about two rings per beam width. Although this sets a constraint in the dependency of the points, it allows a better representation of the galaxy's velocity field. The first step of the procedure consisted of determining the rotation centre (x_c, y_c) and the systemic velocity v_{sys} of the individual rings, while keeping ϕ and i fixed to their optical values. Next, with v_{sys} and (x_c, y_c) fixed, i and ϕ were derived at various radii. This was done for both

sides of the galaxy on one hand, and separately on its approaching and receding sides on the other hand. The variations of ϕ and i as a function of the radius r are shown in the left panel of Fig. 2.8.

The systemic velocity derived for NGC 7424 is 937 ± 3 km s^{-1}, where the error is statistical. This value is consistent with the value of 939.0 ± 1.5 km s^{-1} derived from the global profile of the galaxy using the MIRIAD task MBSPECT, where the error is taken to be the difference between the line centres at 20% and 50% respectively. Because of the low inclination of the galaxy, the variation in both the inclination and the position angle is high in certain regions, especially in the inner $2'$ and beyond $11'$ (Fig. 2.8). We then use the average values of $\phi = 239 \pm 8°$ and $i = 29 \pm 3°$ over the region $2'$ to $11'$ to derive the rotation curve of the galaxy. The resulting curve is given in the right panel of Fig. 2.8 where, as in Carignan et al. (2013), the error on $v_{\rm rot}$ is a combination of the dispersion $\sigma(v)$ in each ring and half the difference between the velocities of the approaching and the receding sides:

$$\Delta v_{\rm rot} = \sqrt{\sigma^2(v) + \left[\frac{1}{2}(v_{\rm rec} - v_{\rm app})\right]^2} \tag{2.3}$$

Because the obtained rotation curve is greatly affected by beam smearing – especially in the inner regions of the galaxy – we used the automatic 3D BAROLO package (Di Teodoro & Fraternali 2015) to re-derive the curve from the 3-dimensional data cube, instead of the 2-dimensional velocity field as is done with ROTCUR. The previously obtained kinematical parameters were used as initial guess, and we adopted the two-stage fit mode of the code, which enables a second fitting stage to fit a Bezier function to the inclination and position angle. The averages of the derived kinematical parameters are $i = 29.8 \pm 1.7°$ and $\phi = 236.9 \pm 3.0°$ for the inclination and position angle respectively, while the new systemic velocity is now 936.2 km s^{-1}. These values are consistent with the results of the 2D fitting with ROTCUR. We compare in the left panel of Fig. 2.9 the rotation curves obtained from the 2D and 3D fitting methods, respectively. The new curve is less sensitive to beam smearing affecting mostly the inner regions of the galaxy. This is further seen in the right panel of the figure where we overlay the two rotation curves on the position-velocity (PV) diagram of the galaxy. The 3D BAROLO rotation curve describes better the rotation of the galaxy, while the ROTCUR-derived curve underestimates the velocities in the inner regions. We quantify that in Fig. 2.10 where we plot the difference between the two velocities of the different curves as a function of the radius. We see that the difference is largest (around 45 km s^{-1}) at the centre of the galaxy, and slowly decreases to about zero in the outskirts.

2.5.2 NGC 3621

Unlike NGC 7424, the galaxy NGC 3621 has been extensively observed in HI (e.g., Barnes et al. 2001, Koribalski et al. 2004, de Blok et al. 2008, Koribalski et al. 2018) and appears as one of the brightest HI sources in the southern hemisphere, at a distance of 6.6 Mpc (Freedman et al. 2001).

Rotation curve

The process used to obtain the rotation curve of NGC 3621 is similar to that described in Section 2.5.1. The systemic velocity obtained for the galaxy is 730.1 ± 1.4 km s^{-1}, consistent with the measurements of Koribalski et al. (2004, 730 ± 2 km s^{-1}) and the value of 728.8 ± 1.5 km s^{-1}, derived from the global profile with the MIRIAD task MBSPECT. The ROTCUR fit of the galaxy revealed large scatters in the galaxy's inclination and position angle at radii larger than 19.2 kpc (Fig. 2.11), probably a result of the galaxy's complex kinematics. The average values of these parameters, derived in the inner regions of the galaxy, are $i = 59.9 \pm 3.2°$ and $\phi = 345.2 \pm 6.7°$. These values, together with the derived value of the systemic velocity, were used as initial guess for the 3D BAROLO fit. Because of the galaxy's asymmetry and disturbed velocity field, we performed additional separate fits for the approaching and receding sides. We present in Fig. 2.12 the variations of the inclination and position angle from the 3D BAROLO fit, as well as the obtained rotation curves. The average inclination and position angle are respectively $64.0 \pm 1.3°$ and $354.7 \pm 3.0°$, consistent with those obtained in de Blok et al. (2008), although the average position angle is a little higher ($\sim 3\%$) than derived by the authors. The approaching and receding curves of the galaxy are very different in shape, with the receding (northern) side being more disturbed. This asymmetry of the galaxy is likely caused by the presence of a cloud-like structure located in the receding side of the galaxy (as is seen in the velocity field in Fig. 2.7). The PV diagram in Fig. 2.13 suggests the presence of a warp in the line-of-sight of NGC 3621, that is more pronounced in the receding side of the galaxy. This further confirms the results of de Blok et al. (2008, Fig. 78 therein) regarding NGC 3621.

To compare the 3D BAROLO rotation curve to the 2D-derived curve, we ran ROTCUR a second time with the kinematical parameters derived above. In the left panel of Fig. 2.13 we plot the two curves together with that obtained by de Blok et al. (2008), where it is clear that we reach radii that are almost twice the radii probed by the VLA observations. The velocities of the 3D BAROLO curve are higher in the inner parts of the galaxy than those of the ROTCUR curve, likely because

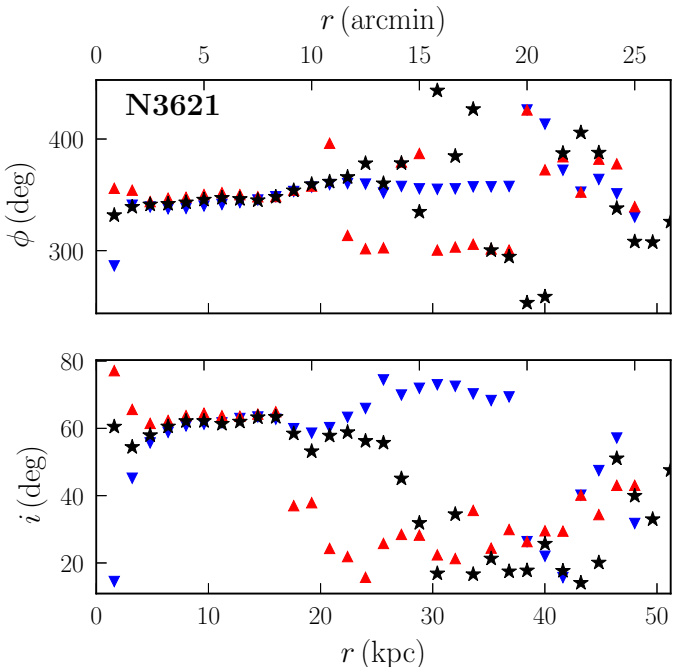

Figure 2.11: Tilted-ring model of NGC 3621 from a ROTCUR fit of the MeerKAT data. Legends are same as in Fig. 2.8.

of the beam smearing effects as in the case of NGC 7424. The 3D BAROLO curve agrees well with the THINGS curve in the inner $\sim$ 20 kpc of the galaxy, although the beam smearing is not completely suppressed in the former curve. Beyond 20 kpc, our curves seem to decrease while the THINGS curve increases. Although the galaxy presents a complex velocity field affected by warps especially in its receding side, the rotation curves derived in this work do not seem to be affected by these warps (see variations of the inclination and position angle in Fig. 2.12). A meaningful interpretation of the difference between our rotation curves and that of de Blok et al. (2008) beyond $\sim$ 20 kpc is hard to provide since the variations (with the radius) of the kinematical parameters obtained by the authors is not available. The difference in the adopted kinematical parameters, as well as the aforementioned stream of cloud that resides in the northern side of the galaxy, may affect the shape of the rotation curve especially in the outer regions. In the right panel of Fig. 2.13 we present a PV diagram of the galaxy on which we overlay the ROTCUR and 3D BAROLO rotation curves. Like in the case of NGC 7424, the rotation curve of NGC 3621 derived with 3D BAROLO describes better the PV diagram of the galaxy, especially in the inner regions. The PV diagram moreover shows that the velocities in the outskirts of the approaching side are lower than the receding side velocities, in agreement with the rotation curves in Fig. 2.12.

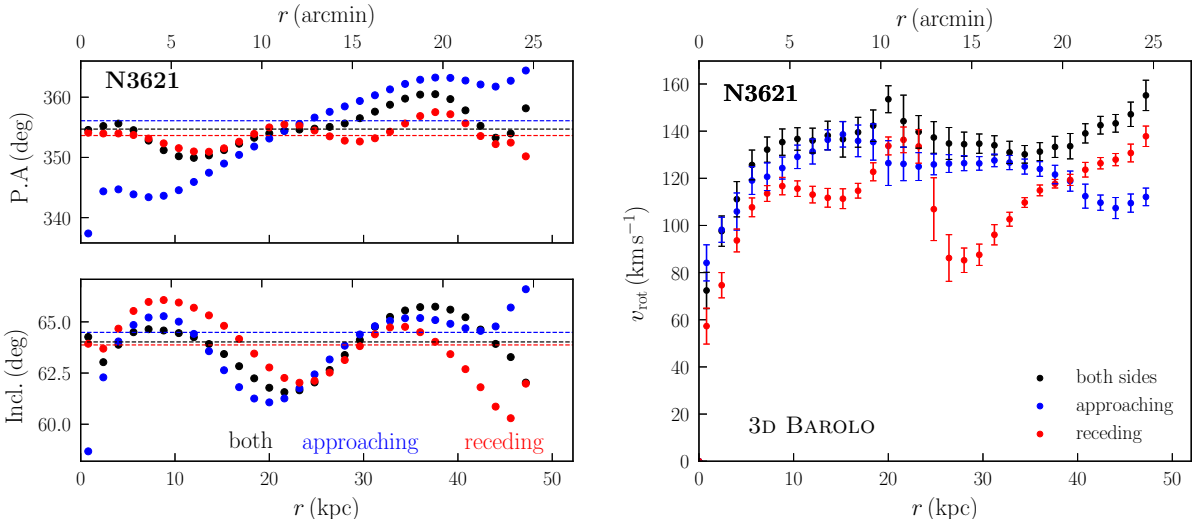

Figure 2.12: The 3D Barolo model of NGC 3621. *Left:* variations of the position angle and inclination. The average values of the parameters are shown by horizontal dotted lines. *Right:* the rotation curve for the approaching and receding sides, as well as both sides combined.

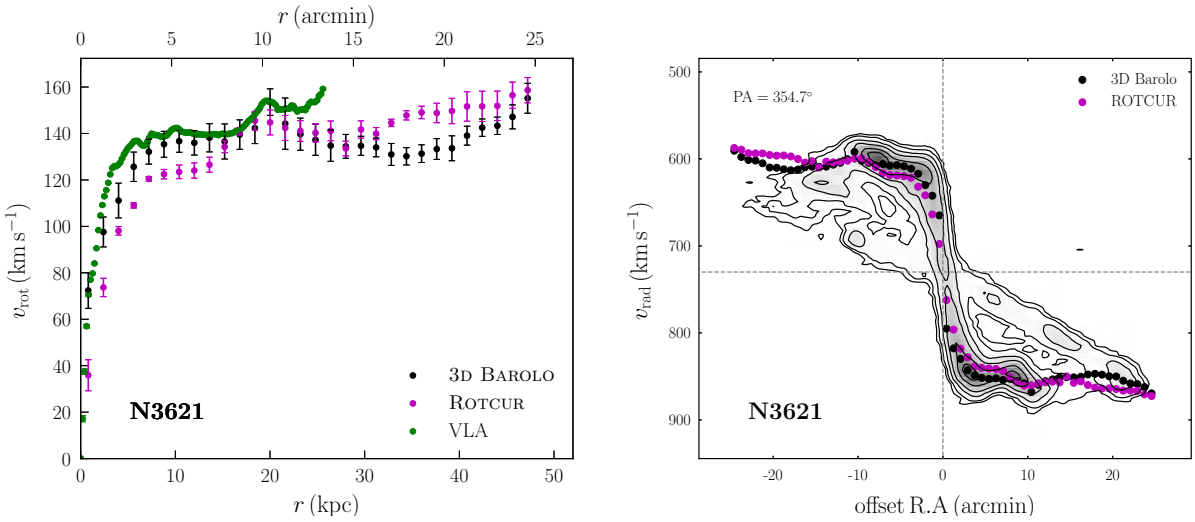

Figure 2.13: Comparison of the derived rotation curves of NGC 3621. *Left:* the 3D Barolo and ROTCUR rotation curves compared to the THINGS curve. *Right:* the 3D Barolo and ROTCUR curves overlaid on the PV diagram of the galaxy.

2.6 Mass models of NGC 7424 & NGC 3621

2.6.1 NGC 7424

The mass models for NGC 7424 were derived using its 3D BAROLO rotation curve and *WISE* (Wright et al. 2010) W1 (3.4μm) band photometry, sensitive to the old stellar populations of galaxies. The W1 light profile of the galaxy presented in Fig. 2.14, along with the galaxy's optical image, suggests the absence of a prominent bulge. An attempt to decompose the light profile in the left panel of Fig. 2.14 further confirmed a negligible bulge. We therefore consider the stellar disc and the gas disc as the only baryonic components contributing to the observed rotation curve. We can write

$$v_{\rm baryonic} = \sqrt{|v_{\rm gas}|\, v_{\rm gas} + \Upsilon_\star\, |v_{\rm disc}|\, v_{\rm disc}} \tag{2.4}$$

where $v_{\rm gas}$ is the gas velocity, $v_{\rm disc}$ the disc velocity and $\Upsilon_\star$ the disc mass-to-light ratio (M/L). $v_{\rm gas}$ is derived from the HI surface density, assuming a thin disc composed of neutral hydrogen and helium (the HI surface densities have been multiplied by 1.4 to take into account the helium and heavier elements). Also, using the W1-W2 (4.6μm) colour and the calibration from Cluver et al. (2014, Eq. 1), we derived an inferred disc mass-to-light ratio of $\Upsilon_\star = 0.25\ M_\odot/L_\odot$. In fitting the rotation curve, we fixed $\Upsilon_\star$ to the theoretical value on one hand, and let it free on the other hand (best fit model). Three different models were used in each case: the pseudo-isothermal (ISO) and the Navarro-Frenk-White (NFW) dark matter models, and the MOdified Newtonian Dynamics (MOND) model.

The pseudo-ISO model

Besides the baryonic components of the galaxy, an important fraction of galaxies' mass is contained in their dark matter (DM) halo. The DM halo contributes to the total rotational velocity of a galaxy, and we can therefore write that

$$v_{\rm rot} = \sqrt{v^2_{\rm baryonic} + v^2_{\rm halo}} \tag{2.5}$$

where $v_{\rm halo}$ is the DM halo contribution.

The density and velocity distributions of the model as a function of the distance r from the halo centre are respectively given by

$$\rho_{\rm ISO}(r) = \frac{\rho_0}{1 + (r/r_0)^2}, \tag{2.6}$$

$$v_{\rm ISO}(r) = \sqrt{4\pi G \rho_0 r_0^2 \left[1 - (r/r_0) \arctan\left(r/r_0\right)\right]} \tag{2.7}$$

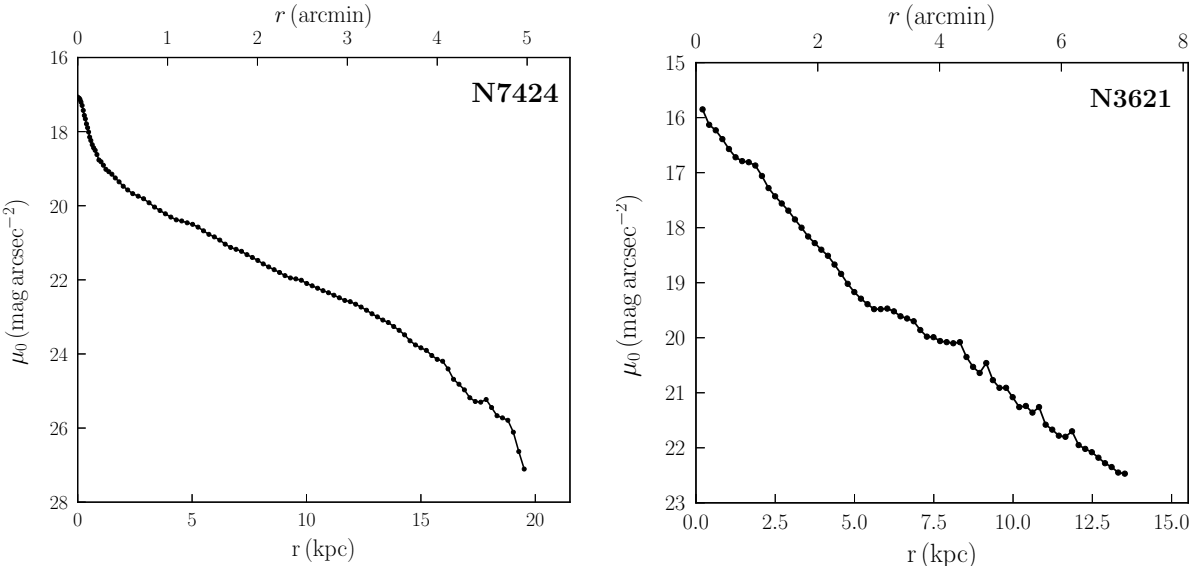

Figure 2.14: *WISE* W1 light profile of NGC 7424 (*left*) and Spitzer 3.6μm of NGC 3621 (*right.*)

where ρ_0 and r_0 are respectively the central density and the scaling radius of the halo. We used the model implemented in the GIPSY's task ROTMAS, with NGC 7424. As stated above, the stellar disc's M/L was first fixed to the *WISE* inferred value, then let free. Table 2.5 summarises the different values derived. The M/L value obtained in the best fit is 0.18 ± 0.57 $M_\odot/L_\odot$, which is consistent with the *WISE* inferred value, and shows that the two fits are in agreement. We present in the top panel of Fig. 2.15 the pseudo-ISO fit with the M/L fixed by the *WISE* colour.

The Navarro-Frenk-White model

The DM halo profile can also be described with the Navarro-Frenk-White (NFW, Navarro et al. 1997) profile derived from N-body simulations. The model describes the density profile by

$$\rho_{\rm NFW}(r) = \frac{\rho_i}{r/r_{\rm S}(1 + r/r_{\rm S})^2}, \tag{2.8}$$

where $r_{\rm S}$ is the scale radius of the halo, and ρ_i is related to the critical density, i.e, the density of the universe at which the DM halo begins to collapse. The resulting rotation velocity can be written

$$v_{\rm NFW} = v_{200}\sqrt{\frac{\ln(1+cx) - cx/(1+cx)}{x\,[\ln(1+c) - c/(1+c)]}} \tag{2.9}$$

where r_{200} and v_{200} are respectively the radius and density at which the density of the halo exceeds 200 times the critical density of the universe (Navarro et al. 1996b). The ratio $x = r/r_{200}$ represents the radius in units of virial radius, and $c = r_{200}/r_{\rm S}$ the concentration of the halo. The NFW mass density profile is cuspy in the inner regions of the halo and can be represented by $\rho \sim r^{\alpha}$, where $\alpha = -1$.

The fit of the NFW model to NGC 7424's observed rotation curve provides a negative M/L value for the stellar disc when the parameter is not fixed to the *WISE* inferred value of 0.25 $M_{\odot}/L_{\odot}$, which is physically unacceptable. Similarly, Carignan et al. (2013) obtained a non-physical stellar M/L of $\Upsilon_{\star} = 0$ for NGC 3109. However, when the stellar M/L is fixed to the *WISE* inferred value, the model provides a good fit to the observed rotation. The NFW model of NGC 7424 is presented in the middle panel of Fig. 2.15.

The MOND model

First proposed by Milgrom (1983a;b) as an alternative to DM, the MOND theory has been widely discussed in the last two decades and has proved successful in accurately reproducing the rotation curves of numerous galaxies (e.g., Begeman et al. 1991, Sanders & Verheijen 1998, Gentile et al. 2010). The model postulates that the classical Newtonian dynamics breaks in regimes where the acceleration is much smaller than the universal constant acceleration a_0, and the law of gravity is modified. The gravitational acceleration of a particle is then given by

$$\mu(x = g/a_0)g = g_N \tag{2.10}$$

where g is the gravitational acceleration, g_N the Newtonian acceleration and $\mu(x)$ the MOND simple interpolating function (Zhao & Famaey 2006).

As for the pseudo-ISO model, we fit the model to the rotation curve of the galaxy for both a fixed and a free M/L parameter. Moreover, we fixed the parameter a_0 to the generally accepted value of $1.21 \times 10^{-8}\,{\rm cm\,s^{-2}}$ (Begeman et al. 1991) on one hand, and let it free to vary on the other. The results of the fits are summarised in Table 2.5. The value of a_0 obtained when $\Upsilon_{\star}$ is fixed to the *WISE* colour is two times higher than the generally accepted value. On the other hand, when a_0 is fixed to the Begeman et al. (1991)'s value, we obtain a $\Upsilon_{\star}$ value of 0.92, i.e more than three times higher than the *WISE* inferred value. These may hint that the MOND model does not provide a good fit to the galaxy's rotation curve, although the obtained χ^2 values suggest otherwise. This is further seen in the bottom panel of Fig. 2.15 where we present the MOND fits to the galaxy's rotation curve with fixed M/L and free

Model		Parameter	Values	
			$\Upsilon_\star$ fixed	$\Upsilon_\star$ free
ISO		$\Upsilon_\star$	0.25	0.18 ± 0.57
		r_0	1.9 ± 0.4	1.8 ± 1.2
		ρ_0	107.9 ± 43.5	124.7 ± 178.5
		$\chi^2_{\rm red}$	1.8	2.1
NFW		$\Upsilon_\star$	0.25	—
		r_{200}	92.7 ± 1.9	
		c	6.5 ± 0.5	
		$\chi^2_{\rm red}$	4.8	
MOND	a_0 free	$\Upsilon_\star$	0.25	0.69 ± 0.14
		a_0	2.5 ± 0.2	1.4 ± 0.2
		$\chi^2_{\rm red}$	3.0	0.8
	a_0 fixed	$\Upsilon_\star$	—	0.92 ± 0.05
		a_0		1.21
		$\chi^2_{\rm red}$		0.9

Table 2.5: Results of the NGC 7424's mass models fits. The $\Upsilon_\star$ ratio is expressed in units of $M_\odot/L_\odot$, and the radii and densities have units of kpc and $10^{-3}\mathrm{M}_\odot\,\mathrm{pc}^{-3}$, respectively. The units of a_0 are $10^{-8}\,\mathrm{cm\,s}^{-2}$.

a_0: the model tends to underestimate the galaxy's velocities in the inner regions.

2.6.2 NGC 3621

The M/L of NGC 3621's stellar disc, as derived from the galaxy's *WISE* inferred colour, is $\Upsilon_\star = 0.50\ M_\odot/L_\odot$. This value is in agreement with the value of 0.59 $M_\odot/L_\odot$ derived in de Blok et al. (2008) who used the Spitzer 3.6μm band photometry to describe the optical component of the galaxy, and also similar to the 3.6μm value suggested by Lelli et al. (2016). Using the method described in Section 2.6.1, we constructed its mass models for the ISO, NFW and MOND models. However, for a more rigorous comparison of the mass models with those obtained in de Blok et al. (2008), we used, instead of the *WISE* W1 profile, the Spitzer 3.6μm light profile of the galaxy as in de Blok et al. (2008). Like in the case of NGC 7424, the galaxy's light profile does not present a bulge (right panel of Fig. 2.14), making us consider its stellar and gas discs as the only baryonic components to account for. Similarly to NGC 7424, we derived both the best fit and colour-fixed M/L models (see Table 2.6). The stellar M/L derived from the ISO best fit is, like in the case of NGC 7424, consistent with the value derived from the *WISE* colour while it agrees less for the NFW and MOND models. Fig. 2.16 presents the different fits for the fixed M/L models.

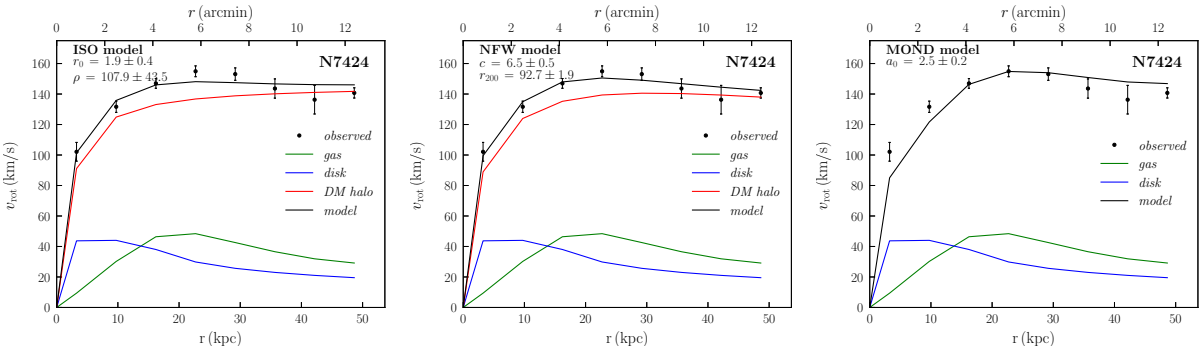

Figure 2.15: The mass models of NGC 7424 for the pseudo-ISO (*left panel*), NFW (*middle panel*) and MOND (*right panel*) models.

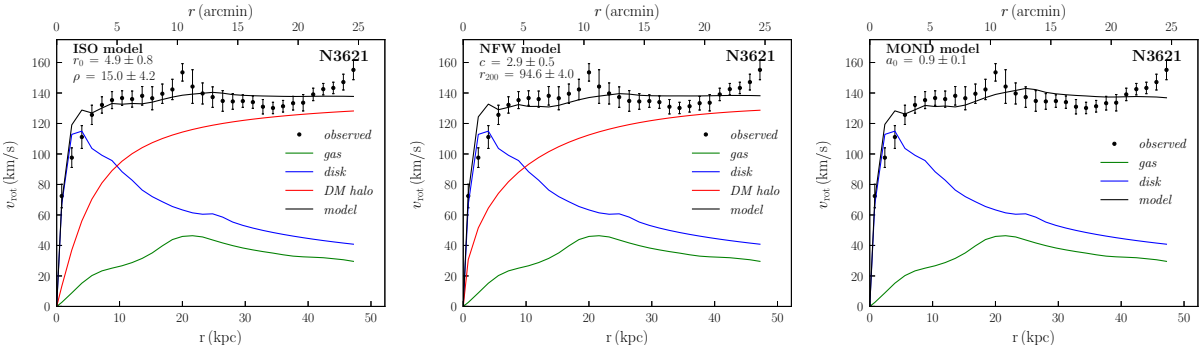

Figure 2.16: The mass models of NGC 3621 for the ISO (*left panel*), NFW (*middle panel*) and MOND (*right panel*) models.

Model		Parameter	Values	
			$\Upsilon_\star$ fixed	$\Upsilon_\star$ free
ISO		$\Upsilon_\star$	0.50	0.47 ± 0.16
		r_0	4.8 ± 0.8	4.4 ± 1.7
		ρ_0	14.9 ± 4.2	18.0 ± 1.0
		$\chi^2_{\rm red}$	2.0	1.7
NFW		$\Upsilon_\star$	0.50	0.36 ± 0.09
		r_{200}	162.7 ± 4.0	87.4 ± 2.5
		c	5.3 ± 0.5	8.0 ± 0.1
		$\chi^2_{\rm red}$	2.4	2.0
MOND	a_0 free	$\Upsilon_\star$	0.50	0.43 ± 0.06
		a_0	0.9 ± 0.1	0.9 ± 0.1
		$\chi^2_{\rm red}$	2.1	2.1
	a_0 fixed	$\Upsilon_\star$		0.36 ± 0.02
		a_0	—	1.21
		$\chi^2_{\rm red}$		2.1

Table 2.6: Results of the NGC 3621's mass models fits. The units are same as in Table 2.5.

2.7 Summary & Discussions

The test observations of the MHONGOOSE galaxies allowed to identify the best calibrators for each of the five galaxies observed. Three different flux calibrators (PKS 1934-638, 0407-658 and 3C138) were used in total, two of which were used per individual galaxy. All the flux calibrators performed well overall, with the flux being quite constant. However, due to the low observing time that the sessions with 3C138 have received, we cannot fully assess the quality of the calibrator. As for the phase calibrators, we successfully identified the best of three candidate sources for each galaxy. The most extreme case of source quality variation was observed between the phase calibrators 0039-445 and 0201-440, where the quality difference of the respective data cubes of the target galaxy was very significant.

The calibrations applied to the KAT-7 observations proved to slightly improve the quality of the data after a self-calibration of the calibrators was performed, as illustrated in Fig. 2.2. However, an estimation of the SNR of the resulting data cubes suggests that the improvement is a function of the size and the brightness of the target galaxy. In fact, the SNR is defined as the ratio between the strongest signal in a particular channel and the channel-to-channel rms:

$$\mathrm{SNR} = \frac{\mathrm{S}_\nu}{\sigma_{\mathrm{rms}}}. \tag{2.11}$$

Since the change in the rms is small compared to a galaxy's signal, and given that the rms in the data does not vary with the galaxy's size and brightness, the change in the SNR will be more noticeable for fainter galaxies than for brighter galaxies. This is what we obtain when comparing the SNR of the five KAT-7 galaxies. For example, the SNR of NGC 7424 before and after self-calibration is about 55, while that of NGC 625 goes from about 26 to about 35, that is, a $\sim 30\%$ increase in the quality of the data.

The search for gas clouds around the candidate galaxies – that might hint at ongoing gas accretion – was unsuccessful despite the high sensitivity of the GBT. Nonetheless, this quest allows us to put an upper limit on the column density levels to which one can expect to detect signs of gas accretion in these galaxies. Indeed, for the galaxies observed with the GBT, any potential search for gas clouds should be conducted at column density levels below a 3σ detection level of $\sim 2.2 \times 10^{18}\,\mathrm{cm}^{-2}$, for a 20 km s^{-1} line width. However, if the low column density gas is in discrete clouds, small compared to the GBT beam, we may have missed them. In effect, the physical size of the GBT beam at the distance of the galaxies range from about 9 to 64 kpc with an average of about 30 kpc, which is the range of sizes at which the

clouds are expected to be found. This confirms that like sensitivity, the resolution of HI observations is important to detect low-column density emission, as was clearly shown for the inter-galactic HI between M31 and M33 (Wolfe et al. 2013), and for some HALOGAS galaxies (Pingel et al. 2018). This is exactly what MeerKAT will provide us with: the ability to detect low column density HI at high spatial resolutions.

The ISO and NFW Dark Matter models of NGC 7424 show a DM-dominated galaxy at all radii (see Fig. 2.15). This is not surprising given the morphological type of the galaxy (late-type spiral), and is in agreement with previous studies on similar galaxies (e.g., Côté et al. 1991, Carignan et al. 2013). The free M/L fit of the galaxy's rotation curve with the ISO model yields a stellar M/L value of 0.18 ± 0.57 $M_{\odot}/L_{\odot}$, consistent with with the *WISE* inferred value of 0.25 $M_{\odot}/L_{\odot}$, although the error associated with the fitted value is large. This large error may hint that using the best fit method is not necessarily the best way to derive the disc M/L ratio of galaxies, and measuring the ratio from the photometry (in this case in the *WISE* W1 band) beforehand can help to better constrain the mass of the stellar component. As for the NFW model, we obtain a negative, therefore physically unacceptable value, making the model less suited than the ISO model to fit the rotation curve of NGC 7424 with free M/L. However, when the stellar M/L is fixed to the value derived from the *WISE* colour, the two models are both consistent with the rotation curve of the galaxy as is shown in the first two panels of Fig. 2.15. For the MOND model, we found that the fits provided values that are inconsistent with the *WISE* colour of the galaxy, and when the disc M/L is fixed, we obtain a value of the parameter a_0 that is not in agreement with the generally accepted value.

The MeerKAT commissioning observations of NGC 3621 with 16 antennas allowed to reach column density sensitivities of $10^{19}\,\mathrm{cm}^{-2}$, similar to the LVHIS observations with the ATCA. The rotation curve of the galaxy derived in this work extends to about 50 kpc, two times more extended than the THINGS survey previously reached with the VLA. The galaxy's total HI intensity map and velocity field suggest that NGC 3621 is asymmetric, and presents a warp in the line-of-sight (see Fig. 2.13). Its rotation curves for both its approaching and receding sides have very different shapes, confirming the complex kinematics of the galaxy. When overlaid on the PV diagram of the galaxy (Fig. 2.13), the rotation curve obtained by averaging both sides fails to accurately describe the approaching side of the galaxy at regions around $10'$, most likely due to the effect of the receding side on the averaged curve. Unlike NGC 7424 whose mass models suggest a DM-dominated galaxy at all radii, the models for NGC 3621 reveal a maximum stellar disc in the inner regions of the

galaxy. The fits of the ISO, NFW and MOND models to the galaxy's rotation curve provide more or less the same accuracy, with the ISO model providing the closest M/L value to the *WISE* inferred value. This result, together with the result of NGC 7424 fits, allows us to conclude that the ISO model is to be preferred over the other two models for these galaxies.

Acknowledgments

The KAT-7 and MeerKAT telescopes are operated by the South African Radio Astronomy Observatory (SARAO), which is a facility of the National Research Foundation (NRF), an agency of the Department of Science and Technology (DST). We thank the West Virginia University Research Office for its support of the operations of the GBT. We also thank Tom Jarrett who provided the *WISE* photometric data of the galaxies NGC 7424 and NGC 3621 used in this work, and Danielle Lucero who helped with the KAT-7 observations. The work of CC is based upon research supported by the South African Research Chairs Initiative (SARChI) of the Department of Science and Technology (DST), SARAO and NRF. The research of AS and MK has been supported by SARChI fellowship. DJP, NMP, and Amy Sardone acknowledge partial support by NSF CAREER grant AST-1149491.

Chapter 3

A $5^\circ \times 5^\circ$ deep HI survey of the M81 group

Abstract

A 25 $\deg^2$ region, including the M81 complex (M81, M82, NGC 3077), NGC 2976 and IC2574, was mapped during $\sim$ 3000 hours with the DRAO synthesis telescope. With a physical resolution of $\sim$ 1 kpc, these observations allow us to probe a large region down to column density levels of $\sim 1 \times 10^{18}$ cm^{-2} over 16 km s^{-1}, mapping the extent of the HI arm connecting the system and NGC 2976, and resolving the HI clouds adjacent to the arm. The observations also reveal a few clouds located between the system and IC 2574, probably tidally stripped from a past interaction between the two systems. Given the regular velocity distribution in the HI envelope of the system, we attempt and derive an idealised large-scale rotation curve of the system. We observe a flat trend for the rotation velocity of the overall system from 20 kpc out to 80 kpc, well beyond the outskirts of the M81 disc, although with asymmetries like a wiggle at the vicinity of M82. This supports the assumption that intergalactic gas and galaxies in the system participate to a large-scale ordered rotation motion which is dominated by M81. Also, our HI analysis of the group further supports the hypothesis that the galaxies forming the system moved closer from afar, in agreement with numerical simulations.

3.1 Introduction

Galaxy interactions are a key process driving the evolution of galaxies in the Universe. The theory predicts that the morphology and gas content of galaxies are shaped by the interactions with their environment and counterparts (e.g., Toomre & Toomre 1972, Gunn & Gott 1972, Dressler 1980). In particular, tidal interactions

are known to affect the stellar disc and star formation rates of galaxies (e.g., Cayatte et al. 1990, Hernquist 1992, Mihos & Hernquist 1996, van Dokkum et al. 1999, Hopkins et al. 2006). However, the component of galaxies through which the impact of galaxy interactions is most easily seen is the neutral hydrogen (HI) envelope, which is known to often extend farther than the stellar disc. In fact, observations of several nearby galaxies exhibiting HI envelopes revealed signs of interactions with either their environment (e.g., Vollmer et al. 2008, Kenney et al. 2014), or with other galaxies (e.g., Hibbard & van Gorkom 1996). One of the best examples of these galaxies is arguably the M81 group, whose main galaxy members (M81, M82 and NGC 3077) seem to share a common HI envelope although their optical discs are distinct.

The M81 group has been the subject of many HI observational studies over the last two decades. However, most of these studies either focused on individual galaxies in the group at high angular resolution (e.g. THINGS; Walter et al. 2008), or covered a large field of view but lacked angular resolution (e.g. GBT observations, Chynoweth et al. 2008; 2009). The first high resolution ($1'$), wide field ($1.7^\circ \times 1.6^\circ$) map of the group was obtained by Yun et al. (1994) with the VLA telescope, and revealed HI complexes in the system down to HI mass limits of $10^6\,M_\odot$. However, the velocity resolution (10.3 km s^{-1}) and HI column density sensitivity ($\sim 2 \times 10^{20}\,cm^{-2}$) of the observations conducted by the authors are limited, compared to the above-mentioned THINGS and GBT observations. Recently, a higher resolution VLA map* of the system was presented by de Blok et al. (2018b), where the discovery of a number of kpc-sized low-mass HI clouds in the vicinity of the M81 complex was reported. The authors achieved a high column density sensitivity level, with a mass detection limit of a few times $10^4\,M_\odot$; but like in Yun et al. (1994) and the GBT observations, the area covered in these observations only includes the complex and the dwarf galaxy NGC 2976 located south-west of the complex. The map presented by Yun et al. (1994) revealed a filamentary structure located west of M81 (but not connected to the complex), and spanning a length of only $\sim$ 21 kpc. In the subsequent high sensitivity map of Chynoweth et al. (2008) with the GBT, the filament appeared to connect the complex to NGC 2976. However, due to the limited resolution of the GBT ($\sim$ 10 kpc), it was impossible to resolve the individual clouds and as a result, it was not clear whether the apparent filament was made of discrete clouds or of a long single tail connecting the two structures. The recent observations of de Blok et al. (2018b) provided a partial answer to these questions, showing that the filament is in fact a series of discrete clouds connected to the M81 system, but not to NGC 2976.

*VLA data publicly available at http://www.astron.nl/~blok/M81data/

However, the lowest contour in the authors' total HI intensity map is $3 \times 10^{19}\,\mathrm{cm}^{-2}$. It is quite likely that an increased sensitivity could allow the detection of a more extended HI filament, possibly connecting to NGC 2976.

To date, none of the existing deep HI observations has ever covered an area of the group wide enough to include both the M81 system and the distant eastern member of the group, IC 2574. Located at a projected distance of 193 kpc from the centre of M81 group, the galaxy IC 2574 has a systemic velocity coinciding with that of the M81 system, which suggests a possible kinematical association with the system. Moreover, the existence of an "optically dark" galaxy – HIJASS J1021+68 – located west of IC 2574 has been reported in the recent blind HI HIJASS survey (HI Jodrell All-Sky Survey, Boyce et al. 2001). This hints at the existence of more low density clouds in the space between the M81 system and IC 2574, and a possible HI connection of the two entities through discrete clouds. A detection of such clouds, which is only achievable through deep HI observations, could offer new insights into the dynamics of the galaxy members of the M81 system.

The present observations aim, primarily, at not only making a full census of the HI clouds around the M81 system and in the region extending towards IC 2574, but also mapping at a high resolution the full extent of the HI streamers, filaments and tails connecting the main group members. We use the Synthesis Telescope (ST) of the Dominion Radio Astrophysical Observatory* (DRAO) to map, at high resolution and column density sensitivity, the HI in and around the M81 complex, including the area located East of the complex and extending out to include the galaxy IC 2574. A total of 30 fields were observed (including archival data), covering an area of 25 squared degrees at a spatial resolution of $\sim 1'$, which, at the distance of M81 (3.63 Mpc, Karachentsev et al. 2004), corresponds to 1.05 kpc. This resolution is ~ 2.5 times lower than that of de Blok et al. (2018b), but the achieved sensitivities are sensibly similar.

To achieve an even higher sensitivity than the previous VLA observations, we smooth the DRAO observations to a lower spatial resolution, in an attempt to not only extend the filament between the system and NGC 2976, but also detect any previously undetected gas cloud lying in the vicinity of M81. In fact, numerous high velocity clouds have been detected around M81 (and in the NGC 2403 group) in a GBT observational campaign of the region conducted by Chynoweth et al. (2008), Chynoweth et al. (2009) and Chynoweth et al. (2011), down to an HI mass limit of a few times $10^6\,\mathrm{M}_\odot$. However, when compared to cosmological N-body simulations, Chynoweth et al. (2011) found that the number of detected HI clouds is significantly

*https://www.nrc-cnrc.gc.ca/eng/solutions/facilities/drao.html

lower than predicted by the simulations. Moreover, the authors found a mismatch between the simulated minihalos and the phase space of the observed clouds. The implication of these results is that there must exist a vast population of smaller (<10 kpc) HI clouds not resolved by the GBT, likely generated by the galaxies themselves and through tidal stripping caused by galaxy interactions. This is confirmed by the de Blok et al. (2018b)'s observations where the authors reported the detection of newly discovered kpc-sized low-mass HI clouds with masses of a few times $10^6\,M_\odot$. This constitutes an evidence that increasing the sensitivity of the data can lead to an increase of the number of new detections.

This paper, which is the first of a series, presents the global results of the deep HI survey of the M81 group. We present here the distribution and kinematics of the HI gas in the group, and present global HI properties of the main group members. In forthcoming papers, we will investigate more deeply the local properties of the HI, especially the HI in the discrete clouds, and study the connections between the galaxies. The present paper is organised as follows: in Section 3.2 we describe the observations conducted with the DRAO ST and the data reduction method. Next, we present the HI profiles of the M81 system member galaxies and the HI maps obtained from the observations in Section 3.3 where we discuss the new features. A kinematical study of the M81 group is presented in Section 3.4, and we discuss the possible dynamical evolutions of the main galaxies of the group in Section 3.5. Finally, we summarise our results and give brief conclusions in Section 3.6.

3.2 Observations and data reduction

3.2.1 Observations

The observations were conducted between 2016 and 2018 using the DRAO telescope. The goals of the observations are as follow: i) detect and better resolve HI streamers, filaments and tails that connect group members over a larger area of the group than the existing HI maps, ii) follow up on the 9 HI clouds discovered in the GBT studies (Chynoweth et al. 2008; 2011) to better resolve them and clarify their relationship with the galaxies and intergalactic HI, and iii) add to the number of newly detected HI clouds in the M81 group, and search among these for possible candidate HI clouds associated with dark matter minihaloes, or new clouds analogous to the enigmatic population in the M31-M33 system (Wolfe et al. 2013; 2016).

With a primary beam full-width at half-power of 107⁄2 in the 21cm, the DRAO ST consists of 7 antennas of 9m diameter each, arranged such that they form an east-west baseline with a maximum separation of 617.1m (see Landecker et al. 2000,

for telescope specifications). The telescope was used to observe, at 1420 MHz, a total of 20 fields (for 144 hrs each) centred on a 25 $\deg^2$ region including the M81 complex, IC 2574 and NGC 2976. Moreover, 10 additional fields (with four centred on two different coordinates) were recovered from the DRAO archive and added to the observed data to increase the SNR in certain key areas (around M81, IC 2574, NGC 2976, and the area between M81 and NGC 2976). In Table 3.1 we give the centre coordinates of each of these fields, which are overlaid on an optical *WISE* (Wright et al. 2010) W1 grayscale image of the region in Fig. 3.1. With a spacing of $\Delta \sim 57'$, the centres of the 20 individual observed fields were chosen to give a uniform sensitivity across the region containing the major galaxy members of the group, while allowing to look for HI in clouds and filaments connecting and bridging galaxy members. It also allows to search for more widespread massive HI clouds associated with the DM halos of the group, whose existence is predicted by numerical simulations and expected to lie within 1 Mpc of the major DM haloes (Blitz et al. 1999). Upcoming observations with the DRAO ST will increase the sensitivity in the eastern region of the mosaic, around the galaxy IC 2574.

The spectrometer used for the observations provides a 4 MHz bandwidth distributed across 256 channels, which corresponds to a channel width of 3.3 km s^{-1} for a spectral resolution of about 5.3 km s^{-1}. The observations were centred on the velocity -36.7 km s^{-1}, which is approximately the central velocity of the complex, and cover the range -459 km s^{-1} to 382 km s^{-1}. The working observed noise at the field centres was on average 1.35 K per channel (or ~ 6 mJy beam^{-1} per channel) and varied only by 0.07 K from field to field. The archived fields are all centred on 0 km s^{-1} velocity and although they do not capture the entire velocity width of HI from the M81 system, after reprocessing to the same spatial and velocity resolution as the 20 new fields, they have similarly low rms noise levels in the range of $1.3 - 1.4$ K per channel. Six of these fields (all except HP03, JG5, JG6 and MB) have a bandwidth of 1 MHz and originally spanned only 64 channels, ranging in velocity from about -105 km s^{-1} to 105 km s^{-1}. The field HP03, like the present observations, has a bandwidth of 4 MHz, covering the range -422 km s^{-1} to 422 km s^{-1}. JG5 and JG6 were observed using the 2 MHz bandwidth, making their velocity coverage -211 to 211 km s^{-1}. As for the field MB, the bandwidth is 0.5 MHz and also centred on 0 km s^{-1}, which corresponds to the narrower range of about -53 km s^{-1} to 53 km s^{-1}.

As an interferometer, the ST is limited in its ability to accurately recover the fluxes of large scale structures, i.e those at angular sizes larger than $56'$, as given by the telescope's shortest baseline of 12.9m. To compensate for this, single dish

observations are combined to interferometric observations to perform a short-spacing correction. In this work, we used single-dish data from the 100m Effelsberg telescope obtained as part of the EBHIS HI survey (Winkel et al. 2016) to apply this short-spacing correction to the ST observations. The EBHIS data have a spatial resolution of 10.′8 and a full spectral resolution of 1.44 km s^{-1}, and covers our whole field both spatially and in velocity.

Field ID	J2000 position		Obs. date	$\theta_{\rm maj} \times \theta_{\rm min}$	$\theta_{\rm PA}$	$\Delta B_{\rm tot}$	Δv	$\Delta v_{\rm res}$	v range	rms
	R.A	Dec.	(YYYY/MM)	($''$)	($^\circ$)	(MHz)	(km s^{-1})	(km s^{-1})	(km s^{-1})	(mJy beam^{-1})
(1)	(2)		(3)	(4)	(5)	(6)	(7)	(8)	(9)	(10)
MG1	09:55:33.17	+69:03:55.0	2015/09	61.6 × 59.0	-90.8	4.0	3.30	5.28	-459 – 382	8.40
MG2	09:44:48.11	+69:03:55.0	2015/09	62.1 × 59.4	-81.4	4.0	3.30	5.28	-459 – 382	8.24
MG3	09:50:10.64	+69:55:06.6	2015/10	60.8 × 59.1	-91.9	4.0	3.30	5.28	-459 – 382	7.90
MG4	10:00:55.70	+69:55:06.6	2015/10	61.1 × 59.2	-86.3	4.0	3.30	5.28	-459 – 382	7.77
MG5	10:06:18.23	+69:03:55.0	2016/01	60.8 × 59.5	-101.4	4.0	3.30	5.28	-459 – 382	8.22
MG6	10:00:55.70	+68:12:43.4	2016/01	61.9 × 59.2	-94.4	4.0	3.30	5.28	-459 – 382	7.99
MG7	09:50:10.64	+68:12:43.4	2016/01	61.3 × 59.8	-90.2	4.0	3.30	5.28	-459 – 382	8.23
MG8	10:11:40.76	+69:55:06.6	2015/11	61.1 × 59.2	-94.0	4.0	3.30	5.28	-459 – 382	8.12
MG9	09:39:25.58	+68:12:43.4	2016/06	61.1 × 60.0	-74.6	4.0	3.30	5.28	-459 – 382	8.52
MG10	10:06:18.23	+70:46:18.2	2016/06	61.6 × 58.9	-76.8	4.0	3.30	5.28	-459 – 382	8.14
MG11	09:44:48.11	+67:21:31.8	2016/06	62.2 × 59.4	-81.9	4.0	3.30	5.28	-459 – 382	8.56
MG12	09:55:33.17	+70:46:18.2	2016/06	60.7 × 58.8	-84.1	4.0	3.30	5.28	-459 – 382	8.26
MG13	09:55:33.17	+67:21:31.8	2016/08	62.4 × 59.2	-89.5	4.0	3.30	5.28	-459 – 382	8.05
MG14	10:06:18.23	+67:21:31.8	2016/08	62.4 × 59.2	-88.8	4.0	3.30	5.28	-459 – 382	8.43
MG15	10:11:40.76	+68:12:43.4	2016/08	62.1 × 59.0	-87.1	4.0	3.30	5.28	-459 – 382	8.12
MG16	10:17:03.29	+69:03:55.0	2016/09	61.5 × 59.1	-81.7	4.0	3.30	5.28	-459 – 382	8.43
MG17	10:22:25.82	+69:55:06.6	2016/10	61.3 × 58.9	-84.1	4.0	3.30	5.28	-459 – 382	8.28
MG18	10:17:03.29	+67:21:31.8	2016/10	62.7 × 58.9	-88.6	4.0	3.30	5.28	-459 – 382	8.41
MG19	10:22:25.82	+68:12:43.4	2016/11	62.1 × 59.2	-83.9	4.0	3.30	5.28	-459 – 382	8.09
MG20	10:27:48.35	+69:03:55.0	2017/01	61.5 × 58.8	-68.0	4.0	3.30	5.28	-459 – 382	7.70
HP03*	09:55:33.17	+69:03:55.0	2014/03	60.0 × 59.6	-79.1	4.0	3.30	5.28	-422 – 422	7.48
JG5*	09:55:33.17	+69:03:55.0	2012/07	62.7 × 58.2	-74.5	2.0	1.65	2.64	-211 – 211	8.80
JG6*	10:28:23.48	+68:24:44.0	2012/07	61.6 × 59.1	-94.7	2.0	1.65	2.64	-211 – 211	8.32
NN*	09:45:20.69	+70:32:11.3	2009/05	61.2 × 58.5	-92.7	1.0	0.84	1.32	-105 – 105	8.01
PO*	10:08:02.65	+70:19:16.1	2010/12	62.1 × 59.2	-102.5	1.0	0.84	1.32	-105 – 105	8.01
PP*	09:47:46.22	+67:48:35.4	2010/11	63.8 × 58.7	-92.1	1.0	0.84	1.32	-105 – 105	8.91
MB*	09:56:54.88	+69:03:50.5	2005/07	62.7 × 58.2	-67.2	0.5	0.41	0.66	-53 – 53	8.64
MB2*	09:56:54.88	+69:03:50.5	2009/01	61.3 × 59.0	-97.1	1.0	0.84	1.32	-105 – 105	8.00
PM*	09:42:42.72	+69:09:55.2	2011/03	61.3 × 58.8	-87.1	1.0	0.84	1.32	-105 – 105	8.43
PN*	09:31:48.72	+68:35:05.2	2011/03	62.1 × 58.7	-91.5	1.0	0.84	1.32	-105 – 105	8.47

Table 3.1: The parameters of the individual fields of the DRAO mosaic. The archived fields are marked with an asterisk. Column (1): Field ID; Column (2): J2000 coordinates of the field centre; Column (3): Date of observation; Column (4): Beam size; Column (5): Position angle of the beam; Column (6): Total bandwidth of the spectrometer used for observation; Column (7): Channel spacing of the corresponding cube; Column (8): Velocity resolution; Column (9): Range of velocity covered; Column (10): Noise per channel in the cube.

3.2.2 Data reduction

Calibration, reduction and data-processing on individual datacubes for each of the fields are undertaken before combining them into a mosaic. The approach used is essentially identical to that developed for the Canadian Galactic Plane Survey (see Section 2.2, Taylor et al. 2003), and also used in Chemin et al. (2009). HI 21cm line (spectrometer) DRAO ST data are bandpass calibrated immediately post-observation, after correlated UV data are formed. At this stage continuum data are brightness-temperature (total intensity) calibrated through observations of sources 3C48, 3C147, 3C286 and 3C295. The spectrometer data are not initially total-intensity calibrated with these astronomical sources at the same time as the continuum; rather this is done at a later stage. Instead, we first perform a channel-by-channel subtraction of the continuum emission in the datacubes. This is achieved by averaging line-free channels at both ends of each datacube, providing two continuum maps (respectively at the low and high velocity ends) that are then linearly interpolated in the velocity space to obtain the continuum level. This continuum level is then subtracted from each channel map of the datacube, providing a continuum-subtracted datacube that is then calibrated. DRAO field observations are bracketed by observing a set of strong compact and non-time variable calibrator sources (3C48, 3C147, 3C286 and 3C295; see Landecker et al. 2000), and continuum maps in each of the 1420 MHz and 408 MHz bands are flux-density calibrated and phase referenced in the post-processing stages of the data product preparation. We use these calibrated continuum maps to calibrate the HI line data as discussed below. The second step consists in performing the calibration, for which two continuum maps are created for each individual datacube: one created by CLEANing (around strong sources) a calibrated continuum map of each field obtained in the 30 MHz-wide band of the DRAO, and a second one created by averaging the above-mentioned end-channels continuum maps. A comparison of the fluxes of point sources between these two continuum maps is then performed, allowing to calibrate the fluxes in the cubes. This calibration method provides uncertainties of about 5%. At this point, the individual fields are continuum-subtracted and calibrated, and spatially overlap as shown in Fig. 3.1. They are then added together following an rms-weighting scheme, to form a single mosaic datacube of $1024 \times 1024 \times 256$ pixels in size, where each pixel is $20''$ wide.

The final step of the reduction consists in adding the single-dish EBHIS data to the DRAO ST data to apply the short-spacing correction. This was done in the image plane, and consisted of smoothing the ST mosaic to the same resolution as the EBHIS data ($10\farcm8$) then subtracting the smoothed mosaic from the EBHIS data

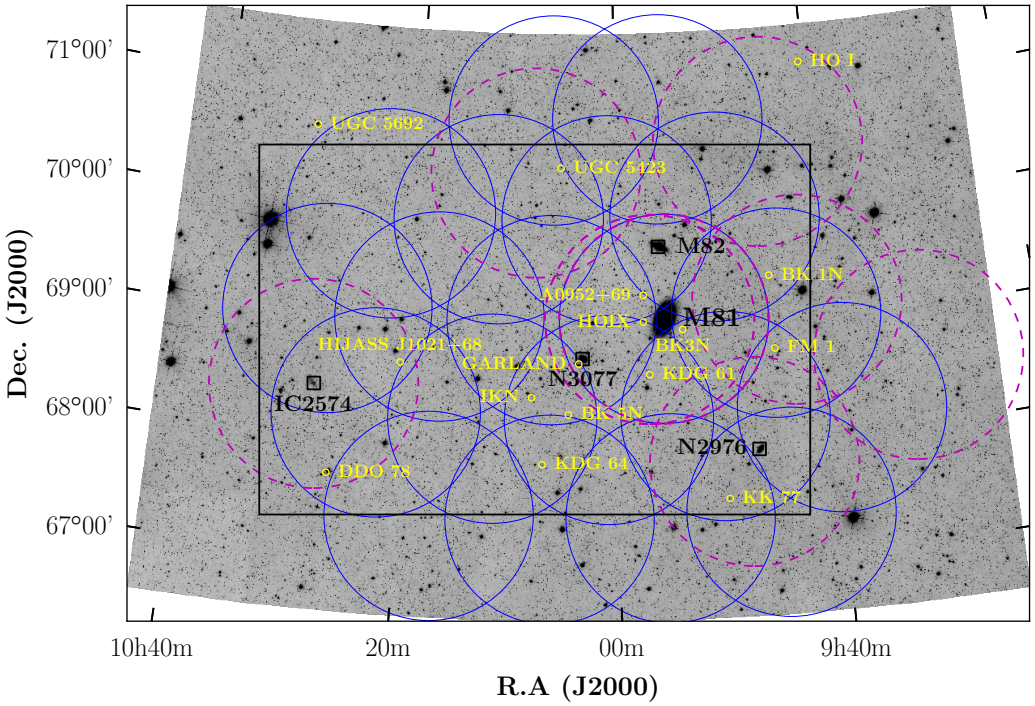

Figure 3.1: The mosaic fields observed with the DRAO ST overlaid on a *WISE* W1 grayscale image of the region. The *blue circles* show the original fields while the *magenta dashed circles* represent the archived data. The rectangle shows the area of the moment maps presented in Figs. 3.4, 3.6, 3.10 and 3.11. The major galaxies of the group are labelled in *black squares* while the dwarf galaxies are labelled in *yellow circles*.

to leave the missing structures that the DRAO ST did not detect. The difference cube, essentially containing structures invisible to the ST, was then added back to the full resolution DRAO mosaic. Due to the careful calibration of our interferometer data and the excellent overlap between spatial structures observed by the ST and the Effelsberg telescopes, the final short-spacings corrected DRAO mosaic shows no negative bowls around structures as large as the MW HI, and as small as the M81/82 galaxies themselves.

The spectral and spatial resolutions of the short-spacing corrected datacube are 5.2 km s^{-1} and $61'' \times 59''$ respectively, with a channel width of 3.3 km s^{-1} and a pixel size of $20''$. The average noise around the M81/82 system is 3.6 mJy beam^{-1}, increasing to 4.8 mJy beam^{-1} around NGC 2976, and reaching 5.3 mJy beam^{-1} around IC 2574. In terms of column densities at a 16 km s^{-1} velocity width, these noise levels correspond to 1.8×10^{19} cm^{-2}, 2.3×10^{19} cm^{-2} and 2.6×10^{19} cm^{-2} respectively around M81, NGC 2976 and IC 2574. In Fig. 3.2 we show a sensitivity map of the datacube, derived from the emission-free channels in the cube. The noise values in the map were determined from a total of 41 emission-free channels (out of a total of 244 channels*) selected at each spectral end of the datacube. We also overplot in the figure the different DRAO ST fields used for the mosaic.

To increase the column density sensitivity of the observations, we have also produced a smoothed version of the cube, with a lower angular resolution of $1.8'$. At the distance of M81, this translates to a physical resolution of 1.9 kpc. This low resolution cube has a spatial resolution of $108'' \times 108''$, and a velocity resolution of 5.2 km s^{-1}. Like the full-resolution cube, it also has a channel width of 3.3 km s^{-1}. The average noise in the cube is 5.5 mJy beam^{-1} around the M81 system, which translates to a 1σ column density sensitivity of 1.1×10^{18} cm^{-2} at a velocity width of 16 km s^{-1}. Because of its higher sensitivity, we will only use this smoothed version of the cube for the rest of the analysis in this paper.

3.2.3 Milky Way emission

A major problem with mapping the HI in galaxies at low systemic velocity is the contamination from the Milky Way (MW). Several techniques exist to remove the MW's foreground HI from observations, ranging from manual mitigations to statistical methods (e.g. Sofue & Reich 1979). Chynoweth et al. (2008) performed, in their work, a spectral interpolation of the signal-of-interest over the contaminated channels, allowing to "guess" the shape of the target emission in these channels. Although

*Twelve of the 256 channels, located at the edges of the cube, were removed because of strong artefacts.

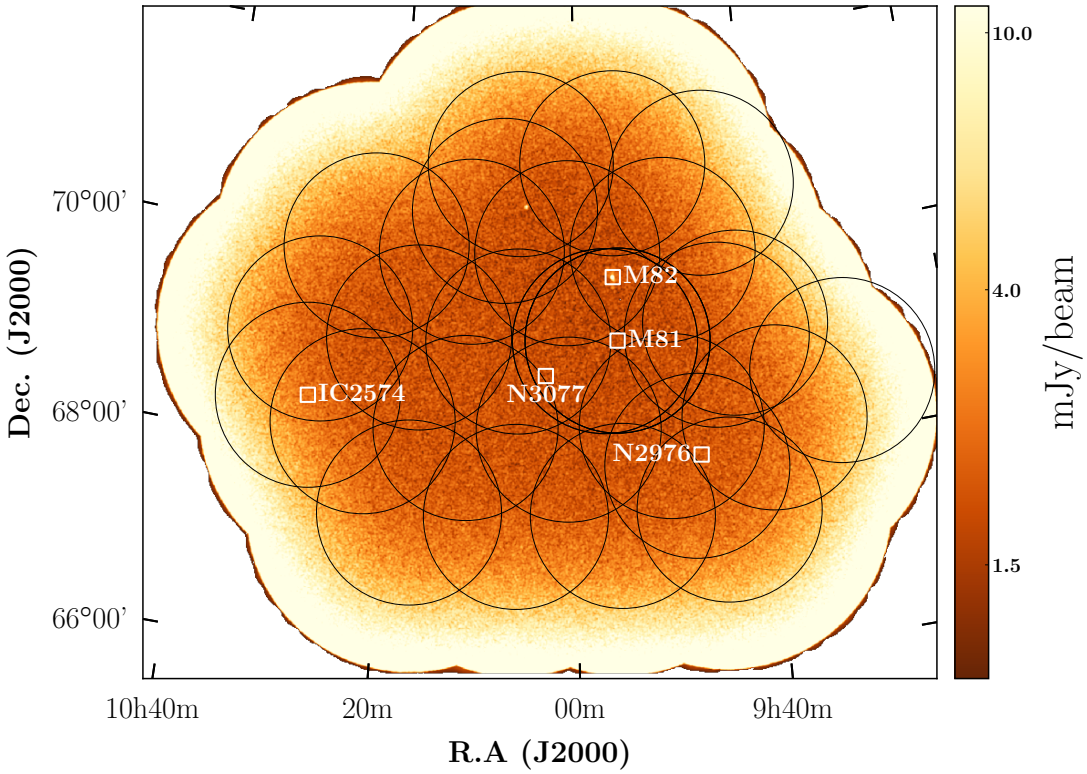

Figure 3.2: Sensitivity distribution map of the mosaic, derived from the line-free channels of the data where the noise is uniform over the central region. The black circles show the individual fields of Fig. 3.1.

this technique provides an acceptable representation of the targeted emission, it does not provide an accurate description of the global profile of the emission, especially for high spectral (and spatial) resolution.

The technique used in the present work is somewhat similar to that described in Chemin et al. (2009), and consists of subtracting a modelled MW emission from the observations. We started by identifying the channels affected by the MW emission and found a total of 24 channels, covering the velocity range -76.3 km s^{-1} to -40.0 km s^{-1} and -23.5 km s^{-1} to 19.3 km s^{-1}. In Fig. 3.3 we present a position-velocity diagram obtained by considering a horizontal slice cutting through the centre of M81, which illustrates the two peaks of the MW emission at -56.5 km s^{-1} and -2.1 km s^{-1}, respectively. Next, we constructed a total HI intensity (zeroth moment) map from the MW-free channels, based on a mask created using the "smooth and clip" method described in Section 3.3.2 below. This MW channels-free intensity map, presented in Fig. 3.4, was obtained by blanking the above-mentioned 24 channels affected by MW emission. The map was then used as a mask to identify and blank the emission of the M81 system from the data. This means that any pixel in the contaminated channels that has a non-zero value in the constructed moment map was blanked. This leaves us with a datacube which has no M81 emission in the MW-contaminated channels. In a subsequent step, we used a two-dimensional gaussian kernel of standard deviation equals to $4.2'$ (equivalent to about 2.3 beams) to interpolate from the non-blanked pixels and replace the previously blanked pixels that presumably represent the emission from the M81 system. Kernels of smaller sizes were found to poorly model the MW emission and therefore produce artefacts in the inner regions of the M81 system, and larger sizes sensibly provide similar results. The interpolation is done individually for all the planes that are MW-contaminated and, in theory, fills the M81 pixels (i.e, pixels that belong to the M81 system) with Galactic foreground emission. Given the high level of foreground contamination of the data, it is best to rule all emission in the affected channels and outside the M81 system as noise or galactic foreground emission. Therefore, the pixels in the affected channels that lie outside M81 (i.e, the pixels outside the moment map) can be discarded by either setting them to zero, or to a pure statistical noise value. In practice, the second option is equivalent to replacing these pixels with their counterparts from emission-free channels selected outside the velocity range of M81. This produces a datacube in which the MW emission is almost completely removed.

An inspection of the resulting cube showed that the procedure described above successfully mitigated most of the foreground HI in the data. However, because of the zero spacing correction of the data, the entire planes of a few channels (where

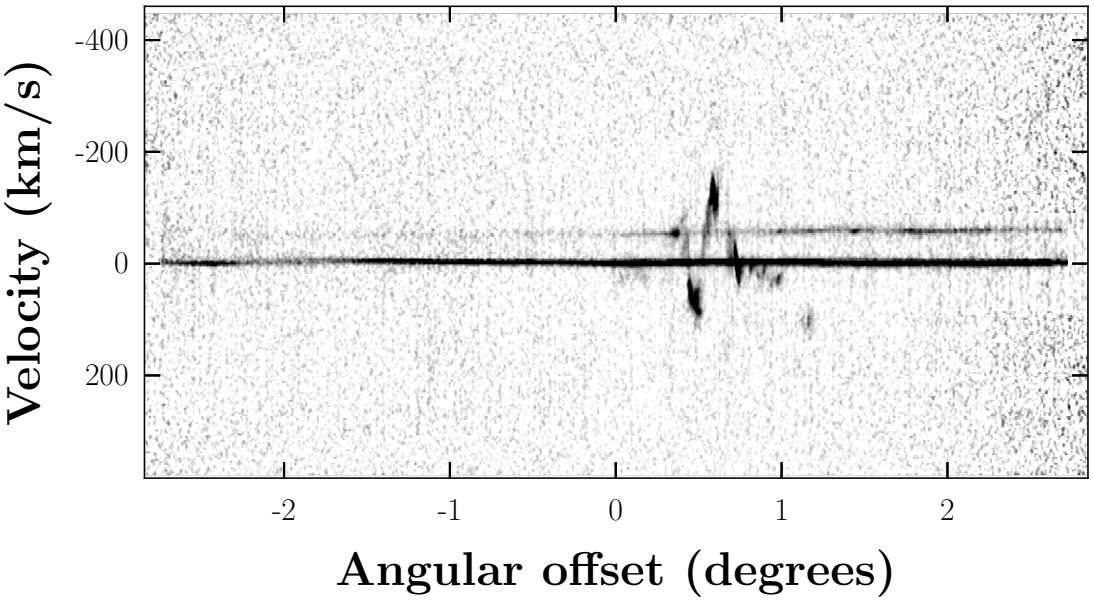

Figure 3.3: Position-velocity slice of the DRAO cube, showing the contamination of the data by the foreground MW emission. The two horizontal lines (centred at -56.5 km s^{-1} and -2.1 km s^{-1}) show the peaks of the Galactic HI.

the foreground emission peaks) were completely covered with bright MW emission. No emission from the M81 system could be detected in these channels because of their low flux relative to the Galactic HI. The applied technique did not succeed at completely removing the foreground emission in these channels due to its relatively high brightness, especially at projected regions around the M82 galaxy and in the northern parts of the western arm of the complex where residual emission are seen. This is partly because the spatial region spanned by the M81 system (masked before modelling the MW emission) represents an important part of the area covered by the mosaic. This therefore lowers the accuracy of the constructed model, resulting in a poor subtraction of the MW in certain regions. However, given the limited number of affected channels and regions, this does not significantly impact the overall global HI properties of the system.

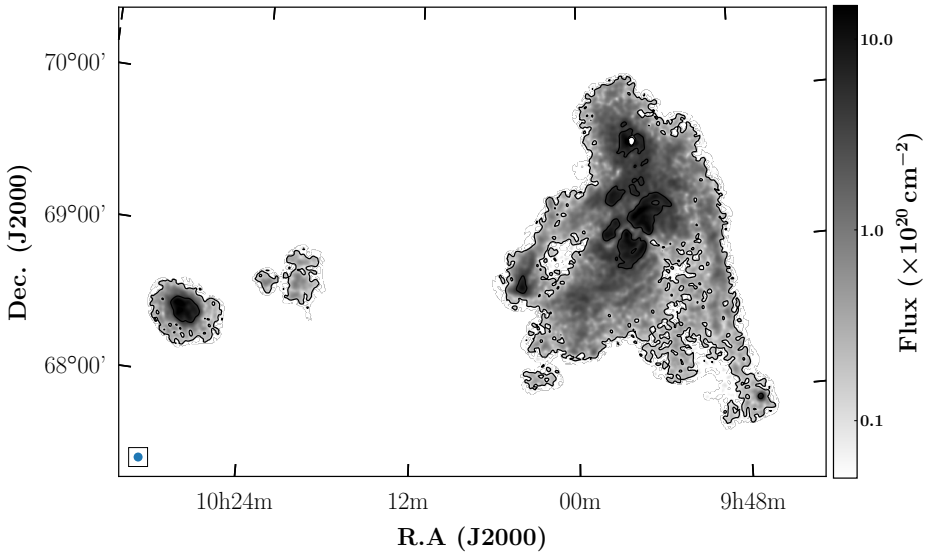

Figure 3.4: Column density map of the data computed by blanking MW channels. The contour shows the $10^{19}\,\mathrm{cm}^{-2}$ column density level.

3.3 HI distribution in the system

3.3.1 Major galaxies of the group

The major three galaxies of the group have been the target of numerous studies in several bands, which helped to shed light on their structure and properties. The general picture of the group is the MW-like galaxy M81 with a stellar mass of $6.4 \times 10^{10}\,\mathrm{M}_{\odot}$ interacting with M82 and NGC 3077 of stellar masses $1.2 \times 10^{10}\,\mathrm{M}_{\odot}$ and $2.1 \times 10^{9}\,\mathrm{M}_{\odot}$ respectively. Their optical properties, as well as those of the other two massive members of the group (NGC 2976 and IC 2574), are listed in Table 3.2. Being the most massive galaxy in the group, M81 (NGC 3031) is a prototypical grand design spiral galaxy. Optical HST observations of the galaxy (Chandar et al. 2001) have revealed the presence of a young, blue cluster population, whose formation appeared to have begun about 600 Myr ago as a result of the galaxy's interaction with its counterparts. Later, Davidge (2009) found that the specific SFR in the M81 disc is consistent with that expected for an isolated galaxy of a similar mass, indicating that the SFR in M81 has not significantly increased in the past few tens of millions of years. The second largest galaxy M82 (NGC 3034) is a starburst galaxy at a distance of 3.5 Mpc (Jacobs et al. 2009), host of several reported supernovae

Object	J2000 position		Type	Distance	m_B	$M_\star$	$d_{maj} \times d_{min}$	P.A	Incl.
	R.A	Dec.		(Mpc)	(mag)	(10^9 $M_\odot$)	($'$)	(°)	(°)
(1)	(2)		(3)	(4)	(5)	(6)	(7)	(8)	(9)
M81	09 55 33.2	69 03 55.1	SAab	3.63	7.89	63.8	26.9 × 14.0	157	57
M82	09 55 52.7	69 40 45.8	SBc[a]	3.53	9.30	12.1	11.2 × 4.3	65	82
NGC 3077	10 03 19.1	68 44 02.1	Sm[b]	3.82	10.61	2.1	5.4 × 4.5	45	38
NGC 2976	09 47 15.5	67 54 59.0	SAc pec	3.56	10.82	1.2	5.9 × 2.7	143	61
IC2574	10 28 23.5	68 24 43.7	SABm	4.02	10.80	0.4	13.2 × 5.4	50	60

Table 3.2: Optical properties of the main galaxies in the M81 group. Column (1): Galaxy name; Column (2): Optical position from NED; Column (3): Morphological type from RC3; Column (4): Distance to the galaxy from Karachentsev et al. (2004); Column (5): Total B-magnitude from RC3; Column (6): Stellar mass of the galaxy derived from *WISE* photometry (courtesy of Thomas H. Jarrett) at the distance listed in column (4); Column (7): Optical diameter measured at the 25th magnitude from Karachentsev et al. (2004); Column (8): Optical position angle from Nilson (1973). Column (9): Optical inclination from Appleton et al. (1981). Notes: [a] morphological type from Mayya et al. (2005); [b] morphological type from Karachentseva et al. (1979)

(Mattila et al. 2013, Gendre et al. 2013) including the recently discovered bright, Type Ia supernova SN 2014J (Goobar et al. 2014). It is a well studied edge-on galaxy, classified as an irregular galaxy in the RC3 catalogue (de Vaucouleurs et al. 1991) but probably more an SBc (Mayya et al. 2005), and provides a good laboratory to study in great detail the properties of the neutral and molecular gas (e.g., Yun et al. 1993, Neininger et al. 1998, Matsushita et al. 2005). Walter et al. (2002b) detected molecular streamers in and below the M82's disc, whose structures provide evidence that the molecular gas within the optical disc of the galaxy is disrupted by the interaction with M81. This further confirms an earlier claim by Sofue (1998), who described M82 as a low-mass galaxy with a strong central concentration of mass and hardly any evidence for a dark matter halo. The smallest of the three galaxies, NGC 3077, was found to have lost its gas during a close encounter with M81 (e.g., Brouillet et al. 1991, Thomasson & Donner 1993, Yun et al. 1993) and high resolution observations show that as much as 90% of the galaxy's atomic gas is situated in a prominent tidal arm (Walter et al. 2002a).

3.3.2 Global HI profiles and moment maps

To compute the global profile of the total HI in the field and the moment maps, we first built a mask of the datacubes. This was done using the smooth and clip algorithm of the SoFiA pipeline (Serra et al. 2015). The pipeline takes as input the (MW-subtracted) datacube and a weight map of the field, computed by taking the

inverse of the rms noise at each spatial position of the cube. The data presented a long horizontal artefact below the system and east of NGC 2976, so this region was flagged in the masking process. The algorithm creates different convolved versions of the cube, and for each of them builds a mask using a user-defined threshold. These masks are later combined into a single, final mask which, in principle, contains both the bright and low-column density structures. Because of the non-uniformity in the distribution of the noise throughout the cube, we used the median absolute deviation (MAD) method on the negative side of the flux histogram to derive the noise in the data. This method computes the noise from the negative voxels only, which are less likely to contain real emission. We performed extensive tests and found that the MAD method provides a more robust measure of the noise than the standard deviation. We also found that the optimum mask is obtained with a combination of six smoothing kernels, which convolve each the data to resolutions equal to 1, 2 or 3 times the original resolution along either the spatial or spectral axes. The convolution process of the data uses a Gaussian kernel along the spatial axes, and a boxcar kernel along the spectral axis. The detection threshold at each of these resolutions is 4σ, where σ is the noise level at the given resolution determined using the above-mentioned MAD method. During the merging phase of the detected pixels into individual sources, we have required that only sources spanning at least 5 channels (16.5 km s^{-1}) be retained. This ensures that noise peaks spanning a few channels are discarded. Furthermore, we have used the reliability module of the package (illustrated in Serra et al. 2012a) to evaluate the reliability of the different sources from the distribution of their "positive" and "negative" detections. The positive (negative) detections are defined as having a total positive (negative) total flux. Then we required that sources with a reliability less than 90% be discarded. A masked version of the datacube was created by applying the resulting mask to the data, and the total HI intensity map (zeroth moment), the intensity-weighted velocity field (first moment) and the velocity dispersion map (second moment) were computed from the masked data using the `MOMENT` task in MIRIAD (Sault et al. 1995). Also, the global HI profiles of the field were computed by integrating all fluxes within each plane of the masked data.

In Fig. 3.5 we show the integrated HI profiles of each of the major galaxies in the field-of-view; for comparison, we overplot in the figure the HI profiles (of the galaxies in the VLA field-of-view) derived from the VLA D-array data. The profiles were extracted within ellipses corresponding to the optical size of the galaxies. We also show in the figure, a comparison of the HI profiles of the DRAO mosaic, VLA D-array mosaic (de Blok et al. 2018b) and GBT (Chynoweth et al. 2008) observations,

integrated over the same area: the field-of-view of the VLA mosaic. The profiles show an agreement between the DRAO and VLA data for most of the galaxies, except for M82 where DRAO recovers more flux than the VLA. This is because, unlike the VLA D-array data, the DRAO data is zero-spacing corrected and is therefore more sensitive to large-scale, faint structures that exist around M82. It is worth noting that the VLA+GBT mosaic of de Blok et al. (2018b) also showed the presence of diffuse gas around the galaxy. Because of the continuum at the centre of M82, any emission or absorption at the core of the galaxy is not reliable; we therefore blanked the inner $2'$ of the galaxy prior to deriving the HI profile. In fact, the bright core of M82 seemed to have phase errors associated with it, which causes baseline variations in the data. Since this is not well modelled by the linear continuum baseline that was fitted and subtracted from the data, the values of the fluxes in this part of the galaxy were found to be inaccurate.

The total HI intensity map of the system, computed from the full resolution and smoothed $1.8'$ resolution datacubes, are presented in Fig. 3.6. The western arm of the system is found to extend as far as to NGC 2976. The projected length of the arm is $\sim 83'$, which corresponds to a physical size of ~ 87.7 kpc at the distance of M81, and has an HI mass of $(4.9 \pm 0.3) \times 10^8\,M_\odot$. Moreover, numerous intergalactic HI clumps were detected in the region between the "main body" of the system and the arm. The previous GBT map revealed an extended cloud of gas in the region (the so-called "Cloud 3" of Chynoweth et al. 2008), and the subsequent VLA D-array map of de Blok et al. (2018b, Fig. 11 therein) also showed HI clouds at that position, connecting to the arm. What is new in the present map is that more small clouds are detected in the area, and they tend to fill the space between the arm and the south-western side of M81. While it is established that the bridges between the interacting galaxies M81, M82 and NGC 3077 have a tidal origin (e.g., van der Hulst 1979, Yun et al. 1994, Yun 1999, de Mello et al. 2008), the long HI filament connecting the triplet to NGC 2976 has a less certain origin. Although one may be quick to rule that it is a tidal bridge resulting from the strong interactions in the group, it is important to note that a more definitive conclusion may be reached from a multi-wavelength study of the gas in the filament. For example, tidally stripped gas is known to be metal-rich while the loosely-bound circumgalactic gas, mostly containing inflowing material, is generally less metal-rich (e.g., Lehner et al. 2013, Tumlinson et al. 2017). A study of the metallicity of the gas in the filament can then help us to determine the nature of the filament, and such study can be done by obtaining UV absorption-line observations of QSOs behind the filament (e.g., Bowen et al. 2016, Lehner et al. 2017).

The primary aim of the present DRAO observations is to make a complete census of HI clouds around the M81 system, and in the space between the system and IC 2574. At a projected distance of 46.5 kpc west of IC 2574, we detected the previously catalogued dwarf galaxy HIJASS J1021+68 (Boyce et al. 2001, Lang et al. 2003) which is not optically detected. The galaxy, which was previously observed to be a single concentration, appears to be surrounded by HI clouds of various sizes. It also appears to be connected to IC 2574, as was suggested by Boyce et al. (2001). However, unlike the single-dish observations, the high resolution DRAO mosaic allows to resolve the connection between the two galaxies, and it is clear in Fig. 3.6 that there exists a "filament"-like complex of clouds connecting the two galaxies. In Fig. 3.7 we show the HI profile of HIJASS J1021+68, as well as those of the neighbouring clouds. Although the systemic velocities of the clouds – and that of the dark galaxy as well – coincide with the MW emission, the profiles show that they are located in spectral regions that are not greatly affected by MW emission and therefore did not require a MW subtraction. However, the position of the peak emission of these clouds with respect of the MW emission suggests that they may just be wings of broader MW emission. To ensure that these structures are not just an extension of the Galactic emission, we have extracted the profiles of four "control" regions of various sizes, at various positions around HIJASS J1021+68. These "control" profiles are shown in Fig. 3.8, and the respective regions they are extracted from are represented by boxes in Fig. 3.9. Contrarily to the profiles of HIJASS J1021+68 and associated clouds, the control spectra show no presence of broad HI emission extending outside the MW-subtracted channels, showing that the clouds are most likely real and are not just remnant Galactic emission.

The derived HI mass of HIJASS J1021+68 is $(3.5 \pm 0.7) \times 10^7\,M_\odot$, in agreement with the quoted HIJASS mass of $3 \times 10^7\,M_\odot$. For the complex of small HI clouds lying east of the object, which seem to form a "filament" towards IC 2574, we measured a total HI mass of $(1.3 \pm 0.5) \times 10^7\,M_\odot$. The northern cloud of HIJASS J1021+68, which seems to connect to the dark galaxy, has an HI mass of $(1.6 \pm 0.6) \times 10^7\,M_\odot$, and the cloud south to the galaxy has a mass of $(0.1 \pm 0.2) \times 10^7\,M_\odot$. A more detailed study of this eastern region of the M81 group will be presented in a subsequent paper.

In Fig. 3.10 we present the velocity field of the complex, computed from the DRAO datacube with the MIRIAD task `MOMENT`. As noted in de Blok et al. (2018b), the velocity field shows a regular rotation of the disc, especially in the inner regions. Beyond a certain radius (approximately 10 kpc along the minor axis) the rotation of the galaxy is disrupted, especially along its minor axis and towards the position of the dwarf galaxy HoIX. There is little velocity gradient along the western arm,

implying that the arm is almost contained in the plane of sky. We also note an arc connecting HoIX to M82, hinting at a kinematical association between the two galaxies. There seems to be a velocity continuity between the western side of IC 2574, the gas cloud HIJASS J1021+68, and the region of the system containing NGC 3077 and the eastern bridge of the system. This, together with the fact that there exists a peak of an apparent cloud in the space between HIJASS J1021+68 and the NGC 3077, may suggest that IC 2574 is not completely isolated from the system.

The velocity dispersion map of the group, presented in Fig. 3.11, shows that the velocity dispersion is, as expected, highest around M82 and in the northernmost region of the western arm. While the dispersion may be intrinsically high around M82, a comparison of the velocity dispersion map with that obtained from the blanked MW channels data has suggested that the high dispersion value in the upper region of the western arm and in the region northeast of M82 is undoubtedly artificial and is likely a result of the MW subtraction.

3.3.3 HI masses

The overall HI detected in the field of the VLA observations, encompassing the M81 system as well as NGC 2976, has a total HI mass of $1.1 \times 10^{10}\,M_{\odot}$ (at the distance of M81) as derived from the DRAO data. As discussed in de Blok et al. (2018b), determining the HI mass of the individual galaxies in the complex can only be done with a limited accuracy, due to the presence of tidal HI features that make it impossible to determine their true HI extent. Several authors (Appleton et al. 1981, Yun 1999, Chynoweth et al. 2008, de Blok et al. 2018b) who have determined the HI mass of the complex's members have performed the measurement within the optical discs of the galaxies. Although this method is likely to underestimate the HI masses (given that the HI envelope is known to extend father than the optical disc), it provides, at the moment, the best estimate that one can obtain. We use here the optical size (D_{25}) of the different galaxies to derive their HI mass, which we compare in Table 3.3 to the values in the literature. We find that the masses derived in this work are higher than those of the VLA D-array of de Blok et al. (2018b), but lower than those of Chynoweth et al. (2008). This is consistent with the expectations, given that the DRAO data is corrected for short-spacing unlike the VLA-only data. Also, the values of Chynoweth et al. (2008) are not only derived from a single-dish telescope, but the fluxes of the sources in the MW-affected channels of the GBT HI datacube are a linear interpolation of the fluxes outside those channels. The masses of Yun (1999) are systematically higher than those measured in the present work, in de Blok et al. (2018b), and in Chynoweth et al. (2008). It is not clear what ellipses

Galaxy	$M_{\rm HI}$ ($\times 10^9$ M$_\odot$)				
	DRAO	dB18	C08	Y99	A81
M81	2.54	2.29	2.67	2.81	2.17
M82	0.44	0.44	0.75	0.80	0.72
NGC 3077	0.33	0.23	1.01	0.69	1.00
NGC 2976	0.14	...	0.52	...	0.16
Total	11.2	7.74	10.46	5.6	5.4
IC2574	1.4	...	...	...	1.0
Total+IC2574	12.6	...	...	...	6.4

Table 3.3: HI masses of the main galaxies in the M81 group. The DRAO masses were derived at the M81 distance. dB18 = de Blok et al. (2018b); C08 = Chynoweth et al. (2008); Y99 = Yun (1999); A81 = Appleton et al. (1981).

Yun (1999) measured the HI masses in, and what the method used for the MW HI subtraction is. To get an estimate of the uncertainty in the HI masses, de Blok et al. (2018b) measured the masses within a radius of $2R_{25}$ and their obtained masses are still lower than those of Yun (1999). The method adopted to determine the masses of the individual galaxies due to the complexity of the system is highly dependent on the ellipses considered, and the different definitions of the size of the galaxies constitute a source of discrepancy between the different HI masses.

Also, it is not clear what method the authors used to mitigate the foreground galactic HI in their data, which covers a non-negligible part of the M81 group. Besides M81, the HI masses of all galaxies derived in Appleton et al. (1981) are higher than those derived in this work, which may be due to the reasons mentioned above.

The total HI mass of the galaxies in the M81 system is 3.5×10^9 M$_\odot$, whereas the total HI mass detected in the field is 1.1×10^{10} M$_\odot$. This implies that only about 31% of the HI in the region resides in galaxies. The majority of the HI is in the form of intergalactic gas and "lives" in structures like bridges, tails and clouds.

3.3.4 Zero-spacing corrected VLA data

The zero-spacing corrected version of the C+D array data presented in de Blok et al. (2018b) was obtained using a GBT dataset from Chynoweth et al. (2011). This GBT dataset covers the M81/M82 and NGC 2403 groups, and has a sensitivity of 2.5×10^{17} cm^{-2} (at a spatial resolution of 9.1′) in the area covering the system. However, due to the baseline subtraction procedure used for the GBT data, the zero-spacing corrected VLA cube contains many artefacts in the Galactic velocity range. This makes it hard to apply the MW subtraction technique described in Section 3.2.3, and the analysis in de Blok et al. (2018b) excludes the MW-affected velocity range.

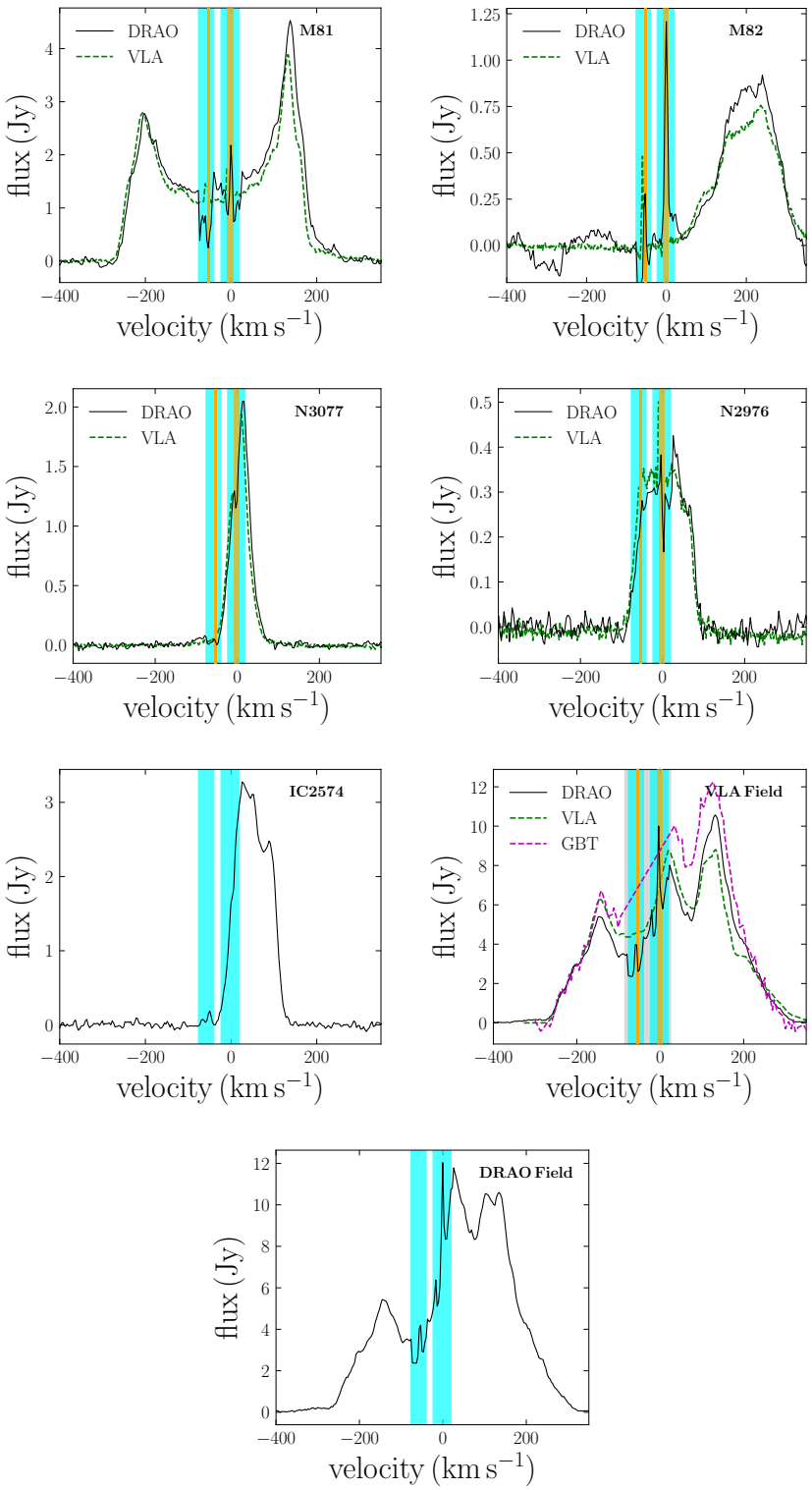

Figure 3.5: HI intensity profiles of the major galaxies of the M81 group (first five panels), derived from the DRAO and VLA D-array datacubes (when available). The last two panels show respectively the HI profiles of the area covered by the GBT (and VLA) observations, and the profile of the entire DRAO field. We also overplot on the second last panel the GBT profile. The vertical shaded areas show the velocity range of the DRAO (*cyan shade*), the VLA (*orange shade*) and the GBT (*light gray shade*) data contaminated by galactic foreground.

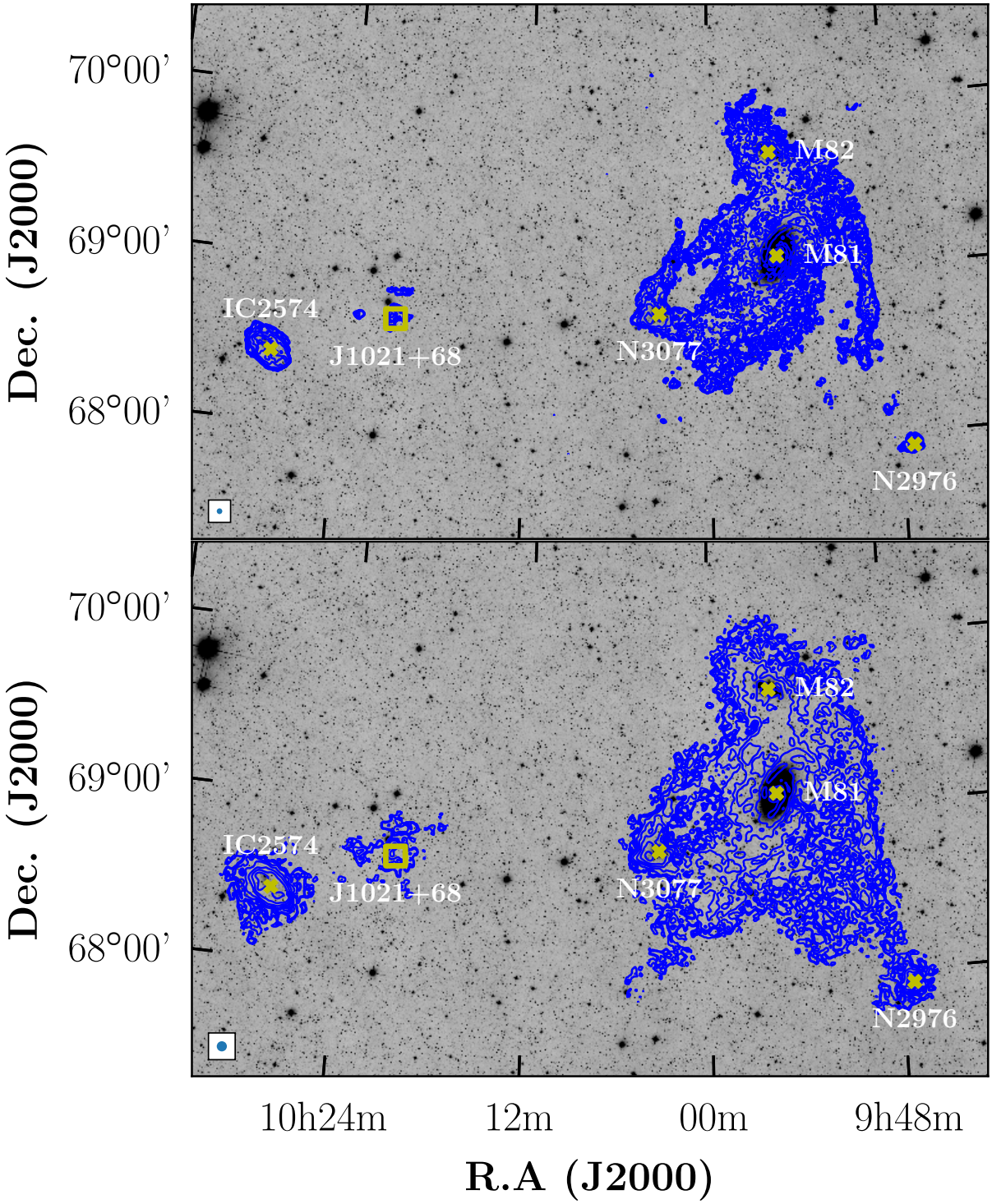

Figure 3.6: Column density maps of the full resolution (*top*) and smoothed 1.8′ (*bottom*) DRAO data overlaid on optical *WISE* W1 grayscale image. The crosses show the position of the major galaxies of the group, and the square shows the position of HIJASS J1021+68. Contours are $1, 2, 4, \ldots, 128 \times 10^{19}\,\mathrm{cm}^{-2}$.

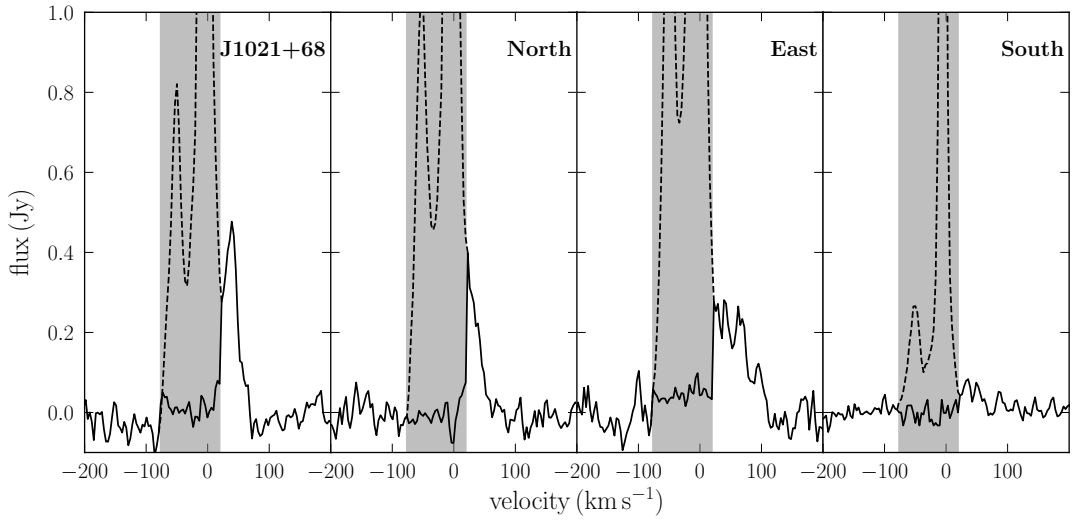

Figure 3.7: The HI profile of HIJASS J1021+68 (first panel) and those of the three neighbouring clouds (second to fourth panel) derived from the MW-subtracted datacube. The *dashed line* shows the global profile before MW subtraction. The grey shaded area represents the entire velocity range processed for MW subtraction. The different parts of the cloud are shown in Fig. B.1.

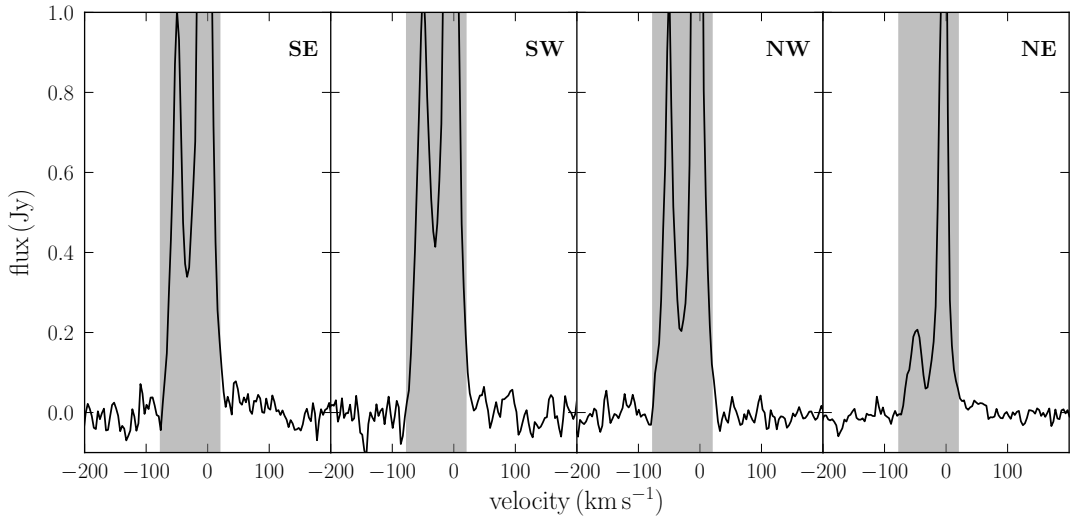

Figure 3.8: The "control" HI profiles of boxes taken southeast (SE), southwest (SW), northwest (NW) and northeast (NE) around HIJASS J1021+68 (see Fig. 3.9 for the positions of the boxes). The peaks of the MW emission in the panels are lower than in the first three panels of Fig. 3.7 due the relatively smaller size of the "control boxes". None of the panels present a profile that spreads outside the grey area, as it the case for the profiles of the clouds in Fig. 3.7.

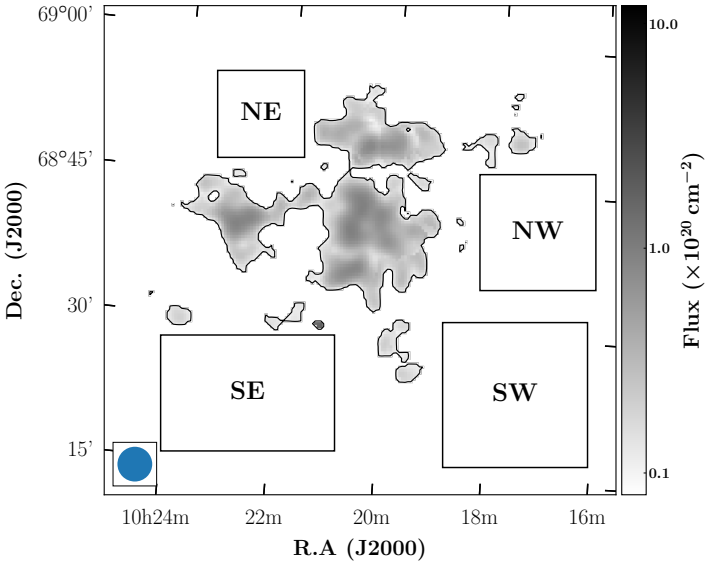

Figure 3.9: A zoom-in on the HIJASS J1021+68 region showing the boxes used to extract the "control" profiles of Fig. 3.8. The labels of the boxes are the same as in Fig. 3.8, and the contour shows the $10^{19}\,\mathrm{cm}^{-2}$ column density level.

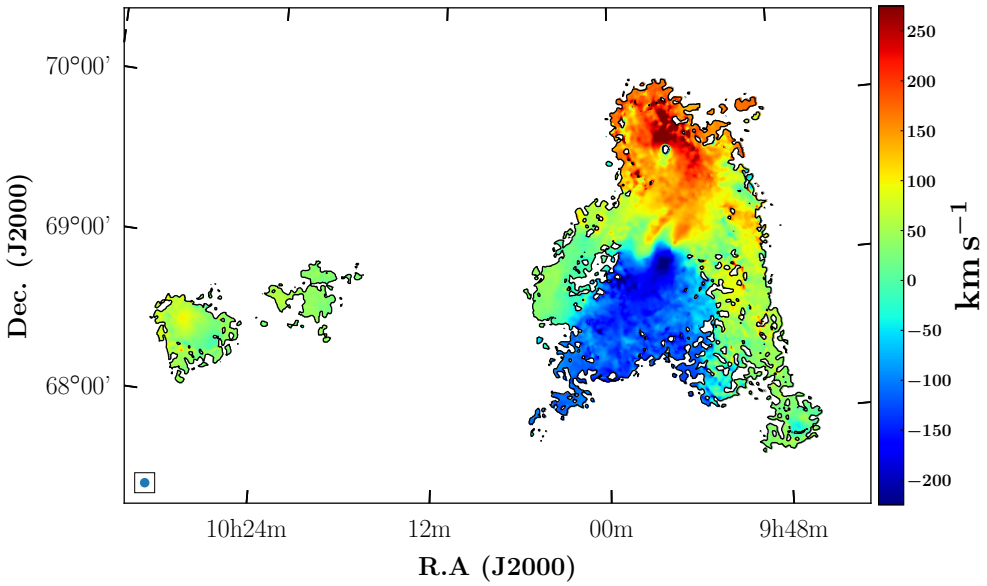

Figure 3.10: The intensity weighted velocity field of the M81 group derived from the DRAO 1.8′ resolution datacube. The contour corresponds to the $1 \times 10^{19}\,\mathrm{cm}^{-2}$ column density level.

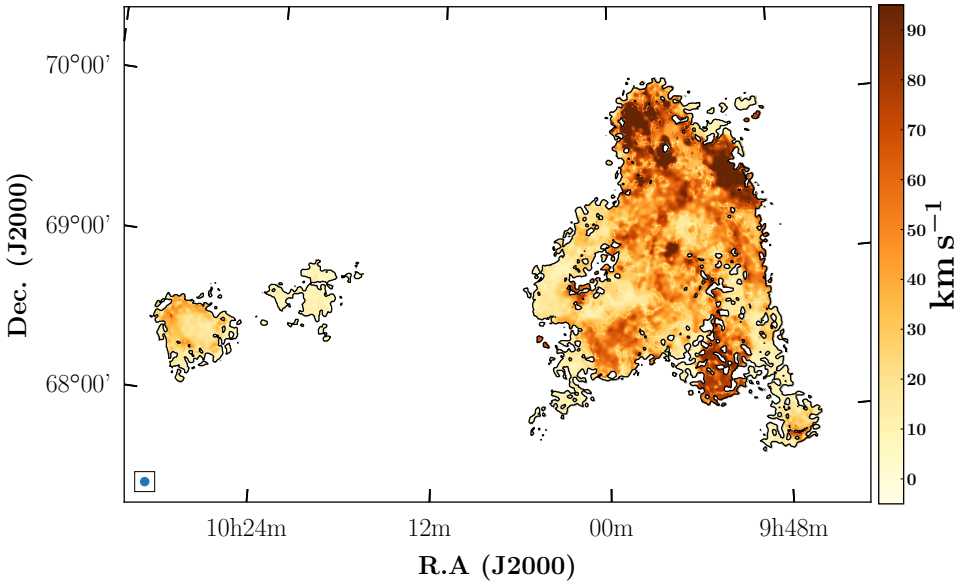

Figure 3.11: The velocity dispersion map of the M81 group derived from the DRAO 1.8′ resolution datacube. The contour corresponds to the $1 \times 10^{19}\,\mathrm{cm}^{-2}$ column density level.

Because of the poor overlap between the two datasets in the *uv* plane (35m to 90m), the data also shows negative bowls around emission peaks, and especially around M82. We therefore re-applied the zero-spacing correction to the VLA data using the Effelsberg EBHIS data of the area covering the M81 galaxies, in order to improve the detection of gas in that region with respect to the analysis made in de Blok et al. (2018b). The EBHIS survey is properly Nyquist sampled on the sky, and can be considered "complete" in the sense that it observes all spatial structures down to its resolution limit. Also, the baseline subtraction procedure was done in a better way than the GBT data, such that there are no negative artefacts in the EBHIS data of the M81 region.

The resulting data contains less artefacts, and shows an improvement over the GBT zero-spacing data. The datacube is $2048 \times 2048 \times 450$ pixels in size, with a pixel size of $6''$ and a channel spacing of 2 km s^{-1}. Applying the technique described in Section 3.2.3, we subtracted the MW emission from the datacube, and used once again the smooth and clip algorithm implemented in SoFiA to build a mask of the resulting datacube. For such a large size of data, SoFiA requires an unusual amount of computing power to work efficiently (see Serra et al. 2015). However, the beam size of the data is $38.1'' \times 30.9''$, translating to a sampling of more than 6 pixels per beam (along the beam's major axis). We therefore spatially resampled the cube to about 3.2 pixels per beam, decreasing its size to $1024 \times 1024 \times 450$ pixels. This was done with the MIRIAD task REGRID. The optimal mask, sensitive to low column density emission and extended structures, was obtained from a combination of masks at a 4σ clipping level at resolutions (1,1,1), (1,1,2), (2,2,1), (2,2,2) and (3,3,1), where the first two numbers of each triplet represent the multiples of the two spatial resolutions, and the third number the multiple of the velocity resolution. In the masking process, we flagged an aliasing effect that was contained in the VLA mosaic, and appeared East of NGC 3077.

In Fig. 3.12 we show a comparison of the re-processed VLA+EBHIS data and the GBT zero-spacing (VLA+GBT) data published in de Blok et al. (2018b). It is clear that our re-processing of the VLA data with other short baselines has improved the detection of gas with respect to de Blok et al. (2018b). In particular, the western arm connected to NGC 2976 is neater, and the emission between that arm and the "main body" of the system is more extended. Also, the C+D map of de Blok et al. (2018b) revealed a few low-mass HI clouds in the vicinity of the system, which they labelled as cloud "1" (North-West of M82), complex "A" and cloud "B" (South of NGC 3077) in their Figure 11. These clouds are found to be more extended in the new "EBHIS-added" mosaic, and we detect two additional clouds east of the system.

These additional clouds, which we denote clouds "C" and "D", appear at velocities of the MW emission and their association to the system is therefore uncertain. However, the peak of cloud "D" appears in the GBT data of Chynoweth et al. (2008) at $4.5 \times 10^{18}\,\mathrm{cm}^{-2}$, but it remains unclear at what velocity the peak is located. At about $17'$ (translating to a projected distance of about 18 kpc) North-West of cloud "1", is located a second cloud (cloud "E") whose peak is seen in the de Blok et al. (2018b) data but appears more extended in the combined data. In Table 3.4 we list the respective HI masses of the different clouds, and for completeness, we also list the HI masses from Chynoweth et al. (2008) and de Blok et al. (2018b). We note that the VLA+EBHIS HI masses of the clouds "1" and "B" are intermediate between the VLA-only and the GBT respective masses. The masses measured in the combined mosaic are about 1.5 higher that those measured in the VLA-only mosaic. This confirms that the extended structures of these clouds are not just a resolution effect, but we detect low column density gas that was previously unseen in the VLA+GBT mosaic. The mass of the complex "A" is higher than in both the VLA-only data and the GBT data, which previously detected two clouds and a single overdensity, respectively. In fact, the GBT mass of "A" and "B" listed in Table 3.4 are masses corresponding to the peak flux of the respective clouds in the GBT map, quoted in de Blok et al. (2018b). Therefore, the listed GBT mass of "A" does not necessarily account for the total mass of the 3 individual clouds, and may thus underestimate the total mass. Similarly to the DRAO mosaic, the VLA+EBHIS map of NGC 2976 shows a cloud South-East of the galaxy, and likely associated the galaxy. This cloud, whose peak only appears in the VLA+GBT map, is also seen in the GBT map as a distinct object from NGC 2976.

3.4 HI kinematics of the system

Besides the major galaxies M81, M82 and NGC 3077, the existence of several dwarf galaxies has been reported in the immediate vicinity of the M81 group (see e.g., Börngen & Karachentseva 1982; 1985, Karachentsev et al. 2000; 2004, Chiboucas et al. 2009; 2013), some of which may have formed as a result of tidal stripping (Makarova et al. 2002, de Mello et al. 2008, Sabbi et al. 2008). Obviously, each of these galaxies orbits on its own plane, and are not necessarily contained in the same plane.

The major galaxies of the group are believed to have interacted closely at least once in the past (Cottrell 1977, van der Hulst 1979, Yun et al. 1994, Yun 1999, Okamoto et al. 2015); and the hierarchical model of the ΛCDM cosmology requires

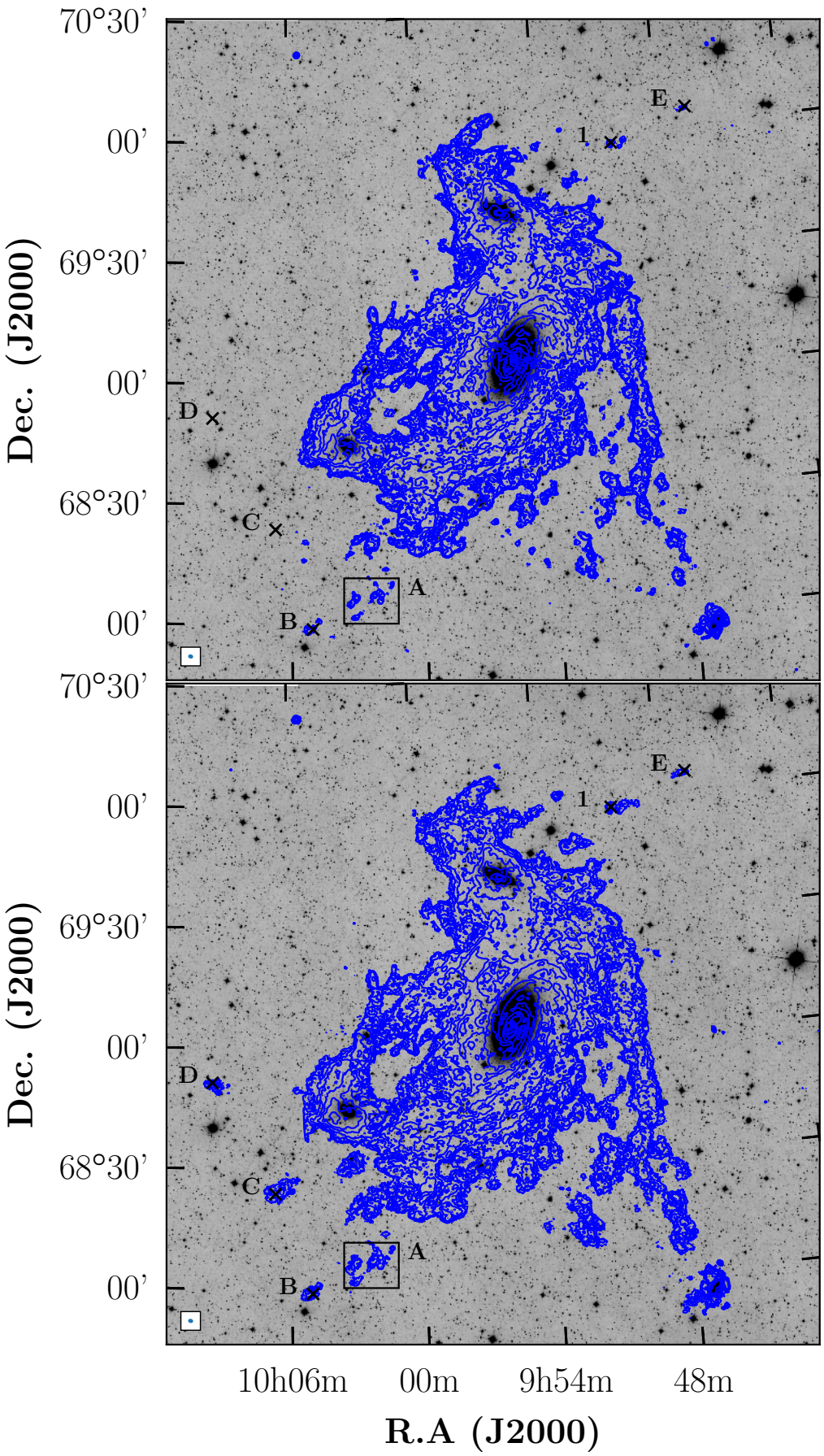

Figure 3.12: The VLA(C+D)+GBT total HI intensity maps of the M81 system. *Top panel*: zero-spacing correction performed using GBT data, adapted from de Blok et al. (2018b); *bottom panel*: zero-spacing correction done with EBHIS data. Contours are $2, 4, 8, \cdots \times 10^{19}$ cm^{-2}.

Cloud	J2000 position		S_{HI} (Jy km s^{-1})	M_{HI} (10^7 M$_\odot$)		
	RA	Dec		VLA+EBHIS	VLA-only	GBT
1	09 50 18.3	69 56 26.0	1.68	0.52	0.32	1.47
A[a]	10 02 23.1	68 06 43.3	4.72	1.48	0.48	1.2
B	10 05 05.0	67 58 28.9	1.52	0.47	0.32	1.2
C	10 06 42.5	68 23 25.1	3.18	1.00	...	...
D	10 09 34.2	68 51 13.5	1.15	0.35	...	...
E	09 46 35.7	70 03 57.6	0.56	1.74	0.02	...

Table 3.4: HI mass of the clouds detected in the VLA+EBHIS mosaic. Cloud "1" was named so in Chynoweth et al. (2008), and clouds "A" and "B" in de Blok et al. (2018b). All masses derived in this work were determined at the distance of M81. The VLA-only masses are taken from de Blok et al. (2018b), and the GBT masses from Chynoweth et al. (2008). Note: [a]: the complex A is composed of three clouds, and the quoted mass corresponds to the total mass. The listed position corresponds to the peak of the Western cloud, which is the brightest. The peaks of the Eastern and Southern clouds have coordinates (10:03:05.7, 68:05:46.9) and (10:03:14.9,68:01:07.0), respectively.

that the group was formed through the infall of the individual galaxies. Using semi analytic models, Oehm et al. (2017) investigated the possible orbits of the three major galaxies and found that both or at least one of the galaxies M82 and NGC 3077 started out from far away and was not bound to the central M81 galaxy 7 Gyr ago.

In Fig. 3.13 we show an interactive 3-dimensional map (inspired by Fig. 4 in Hess et al. 2018) of the DRAO HI datacube of the M81 group. The volume rendering was produced with the SLICERASTRO package (Punzo et al. 2017), which allows the user to manually set the flux in the data. The package contains different modules designed for viewing and analysing HI line data. To optimise the volume rendering of the M81 cube, we have used a gaussian filter in the ASTROSMOOTHING module to smooth the cube down to a 4.8′ resolution, and have chosen 3 separate intensity ranges to distinguish different components of the complex. These components are represented by different colours and opacities in the figure: the green transparent contours representing the HI envelope of the complex, the yellow contours showing the intermediate column density component of the system containing the HI northern and southern tidal bridges connecting the galaxies of the system as well as part of the western arm. This intermediate column density component also reveals a few HI clouds around the system and IC 2574, and the optically dark galaxy HIJASS J1021+68. Finally, the core objects of the M81 are revealed by the high column density component shown in opaque red in the figure.

It is evident from the figure that the members of the system are not contained

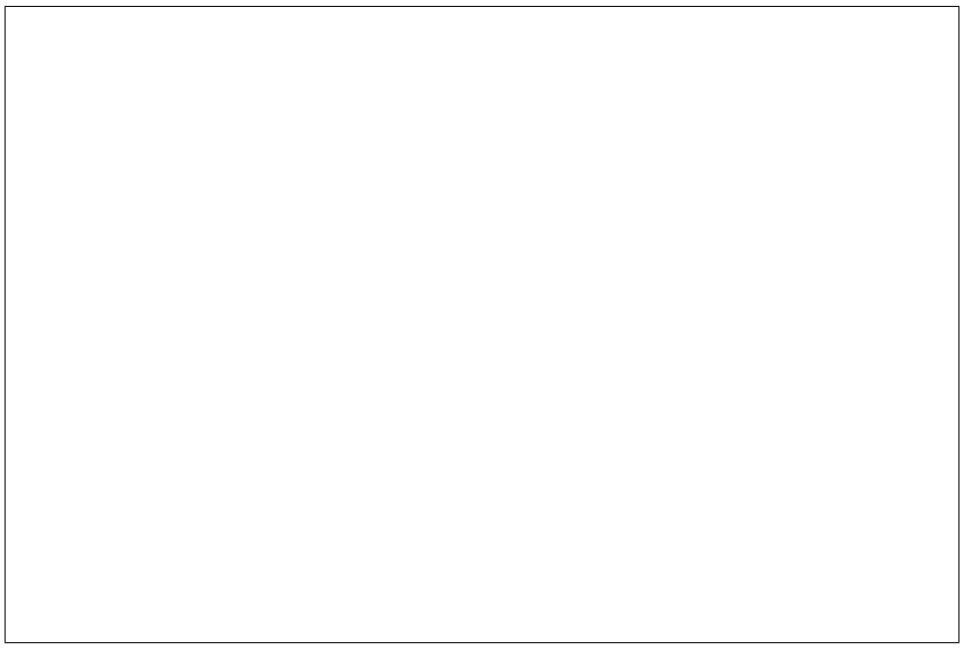

Figure 3.13: Interactive 3D rendering of the M81 group (must be opened with Adobe Acrobat). The green contours represent the low column density envelope, the yellow contours show the intermediate column density structures, and the red solid components represent the inner regions of the major galaxies.

in the same plane, with M81 being more inclined than the plane of the envelope engulfing the individual galaxies, and the companion galaxies having different inclinations. However, despite the complexity of the geometry in this inner region of the group and the interactions between the members the common envelope seems to cut through the discs of M81 and M82 around their respective centres and presents little perturbations. Furthermore, the velocity field of the complex in Fig. 3.10 suggests a large-scale, ordered motion of the galaxies around the M81 galaxy, with the receding northern part that contains M82 and A0952+69 (the Arp's loop), while the southern part containing KDG61 and pointing towards BK5N and KDG64 approaches the observer. In that large-scale framework, regions at the systemic velocity of the system would contain BK3N, and the arms pointing towards NGC 3077 and Garland (East) and NGC 2976 (West) also at velocities close to systemic would act like prominent wiggles (streaming motions). It is thus tempting to fit an idealised kinematic model to the velocity field, like the usual tilted-ring model. We test that hypothesis in the following section.

3.4.1 Tilted-ring model

To measure the large-scale rotational pattern, we used the tilted ring model implemented in the GIPSY (van der Hulst et al. 1992) task ROTCUR (Begeman 1989). However, unlike for single galaxies whose rotational pattern is easily described by a circular orbit, the complex structure of the M81 group requires an extra caution. This is because the system is made of galaxies of different sizes and not necessarily orbiting in the same plane. Moreover, some of these galaxies are known to be strongly interacting, which is likely to cause non-negligible, non-circular motions that will influence the overall rotation of the large-scale system. Therefore, instead of assuming a circular orbit to describe the gas in the complex as is usually done for individual galaxies, one has to consider an additional radial, non-circular velocity component. The observed velocity is therefore the projection of the rotation and radial velocities along the line-of-sight, and can be written

$$v_{\rm obs} = v_{\rm sys} + v_{\rm rot}\ \sin i\ \cos\theta + v_{\rm rad}\ \sin i\ \sin\theta, \tag{3.1}$$

where $v_{\rm sys}$, $v_{\rm rot}$, and $v_{\rm rad}$ are respectively the systemic, rotation and radial velocities, and i and θ are respectively the inclination and the azimuthal angle in the assumed plane of the complex. The latter is function of the position angle ϕ of the semi-major axis of the receding side of the system.

The tilted ring model was fitted to the velocity field presented in Fig. 3.10, with the optical parameters (centre position, position angle and inclination) of M81 as initial parameters. This choice of initial parameters is motivated by the fact that the velocity field is centred on the galaxy, and seems to expand out to the other two major galaxies of the system. With all parameters let free, we derived, in turn, the systemic velocity and dynamical centre of the complex. Because of the particularly complex structure of the system and to be sensitive to the local motions, we used a uniform weighting function where all points in a given ring are given the same weight.

We found that the dynamical centre is at (α, δ) = (09:56:22.9, +69:03:05), with a systemic velocity of $v_{\rm sys} = -5.0$ km s^{-1}. To put this in context, the dynamical centre is located 4.5′ east and 29 km s^{-1} away from M81 centre (M81's systemic velocity is -34 ± 2 km s^{-1}, Appleton et al. 1981). Keeping these parameters fixed and all others left free, a third ROTCUR run was used to determine the position angle and inclination of the system out to 79 kpc. The inclination is found to be increasing with the radius, while the position angle shows little variation. The velocity field of the system shows perturbations due to its complex structure, with

the most noticeable being the deviation along the minor axis of M81, at the position of the dwarf galaxy HoIX. This region seems directly connected in velocity space with M82 through an arc. To exclude as much as possible these perturbations from the rotation curve, we fitted a first order polynomial to the inclination and position angle whose variations are partly caused by these perturbations. We ran ROTCUR once more with these parameters fixed to the fitted values, with only the rotation velocity allowed to vary freely. The process was repeated for the approaching and the receding sides separately, and we show in the left panel of Fig. 3.14 the variations of the position angle and inclination with the radius. The trends of the P.A for the 3 models (approaching, receding and both sides) are similar, with a highest slope noted for the approaching side. In the inner regions of the system, the approaching side shows, on average, lower values of P.A than the other two models. The variations of the inclinations, on the other hand, tend to be similar for the approaching side and the "both sides" models, while the trend of the receding side is different: while the inclination tends to increase with the radius for the approaching side and both sides, we observe a slight decrease of the inclination on the receding side, for which there is a large scatter in the outer parts. The average values of the adopted inclination and P.A for the overall model are respectively $i = 62.^{\circ}0 \pm 9.^{\circ}1$ and $\phi = 346.^{\circ}7 \pm 8.^{\circ}0$

3.4.2 Rotation curve

The rotation curve of the M81 system is presented in the right panel of Fig. 3.14. The uncertainties on the velocities of the average model of both sides are the quadratic sums of the uncertainties of the ROTCUR fits and half the difference between the approaching and the receding side. Also shown are the rotation curves for each of the approaching and receding sides. Not surprisingly, the approaching side is very different from the receding side, with the former peaking in the innermost region before gradually decreasing with the radius down to about 100 km s^{-1}. The receding side, on the other hand, increases slowly in the inner regions, shows signs of perturbation around the position of HoIX, and stays more or less flat in the external regions with a spike between $40'$ and $50'$, corresponding to the position of M82. This difference in the trends of the approaching and receding sides agree with the expectations, given the complex structure of the HI in the complex. In fact, as noted earlier, the galaxies in the system are not contained in the same plane, and lie each at a different inclination. Each of these galaxies affects the rotation of the gas in a different way: on the receding side, the average inclination of the complex is lower than M82's inclination of 82°, which tends to overestimate the rotation velocities; on the other hand, the average inclination is higher than NGC 3077's inclination of

38°, which is located on the approaching side of the complex. This results in an underestimation of the velocities of the approaching side.

Despite these differences, the observation of a "flat" velocity curve in the outermost regions, with an amplitude comparable to that in the innermost region (the M81 disc) corroborates the visual aspect of a common rotational pattern for the interacting galaxies, that has M81 at the mass centre.

The large-scale ordered motion is also accompanied with a significant non-circular, radial motion (green symbols). In the inner part, it is likely caused by the prominent spiral structure of M81, while in the outer regions it could reflect the respective motions of gas and galaxy companions with respect to M81. Due to the complexity and the unknown 3D geometry of the system, it is not possible to constrain whether the radial motions are directed inwards or outwards.

The rotation curves of the individual galaxies M81 and M82 have been derived by a few authors (e.g., Rots 1974, Visser 1980 and de Blok et al. 2008 for M81 using HI data, Sofue & Yoshiaki 1997 for M81 and M82 using CO(2-1) and HI data), and they revealed the complex rotations of the galaxies. The HI rotation curve of M81 derived by Rots (1974) extended out to $\sim$ 20 kpc and showed that beyond $\sim$ 10 kpc, the curve of the receding side rises to high positive velocities, whereas that of the approaching side decreases monotonically. Unsurprisingly, this picture of the M81 galaxy's rotation resembles the trends that are seen in the rotation curve of the complex shown in Fig. 3.14, given that the galaxy constitutes the central part of the complex. Moreover, Visser (1980) and de Blok et al. (2008) found that the rotation velocity of the galaxy is of the order of 250 km s^{-1}, and slightly decreases in the outer parts (from about 7 kpc) out to 15 kpc. This presents a picture of the galaxy whose rotation is high in the central regions, but tends to slow down as one moves to the outer regions. On the other hand, the hybrid rotation curve of the galaxy derived in Sofue & Yoshiaki (1997) showed that its rotation velocity peaks to about 300 km s^{-1} in the central regions, before staying slightly over 200 km s^{-1} out to about 10 kpc. Beyond this point, the curve decreases very slightly below 200 km s^{-1} out to $\gtrsim$ 20 kpc. This discrepancy with the HI rotation curve shows that the atomic and molecular gas rotate differently in the galaxy. As for M82, Sofue & Yoshiaki (1997) found that the galaxy's rotation curve decreases monotonically from 200 km s^{-1} to about 50 km s^{-1} in its inner $\sim$ 4 kpc. They later attribute this unusual shape of the galaxy's rotation curve to its interaction with M81 (Sofue 1998). In Fig. 3.15 we show a comparison of the different above-mentioned rotation curves of M81 to the inner parts of system's large-scale rotation curve, where each curve was corrected to the same distance scale. Although no robust and direct comparison of the rotation

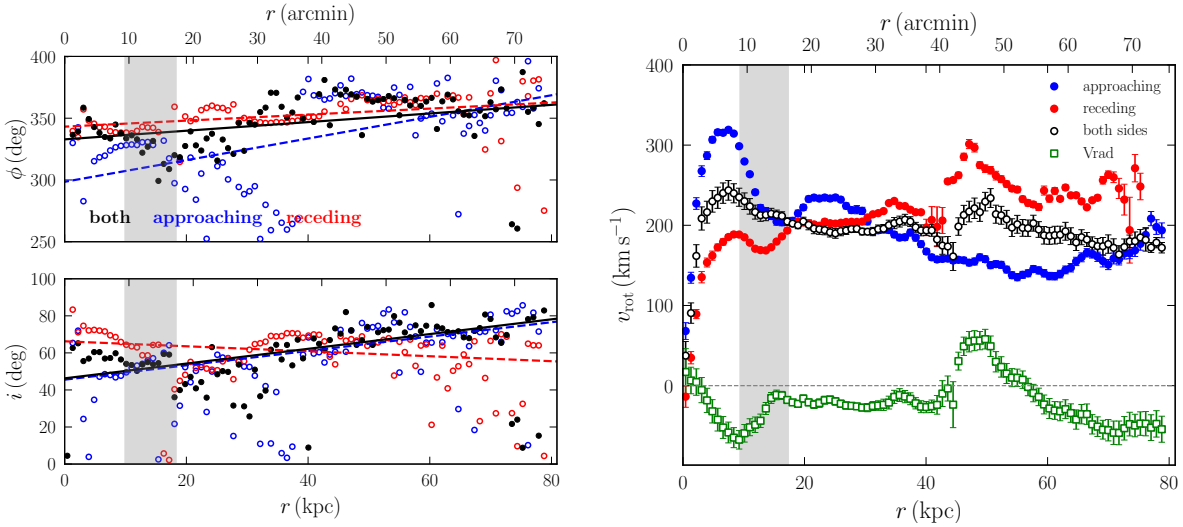

Figure 3.14: *Left panel:* The variations of the position angle (*top*) and the inclination (*bottom*) as a function of the radius in the tilted-ring model of the M81 system; *right panel:* Rotation curve of the M81 system derived using the tilted-ring model. The *green dots* show the variations of the radial velocities. The grey area in both panels corresponds to the position of HoIX.

of the two systems can be made because of the difference in the adopted kinematical parameters, the agreement of the different curves in the regions between $\sim 5-10$ kpc shows us that the M81 system's rotation is significantly influenced by the M81's disc. The discrepancy between the system's rotation curve derived in this work and those of the literature is likely an effect of beam smearing due to the lower resolution of our data (see, e.g. Swaters et al. 2009, Sorgho et al. 2019a).

3.5 Dynamical evolution of the group

The large-scale maps derived from the present observations reveal new HI features of the M81 system that help us to understand the evolution of the group. The presence of gas clouds near the system, as well as the continuity of velocity in the region between the eastern side of NGC 3077 and the western side of IC 2574 suggests that there may exist more low column density gas around the system that was not detected in the present observations. This raises more questions about the formation and dynamics of the member galaxies of the group. Of course, a definite evolutionary scenario can only be obtained through numerical simulations, but the observational view offered by the present HI data suggests that the galaxies have formed individually at different positions, and have moved closer to each other, up to a point where

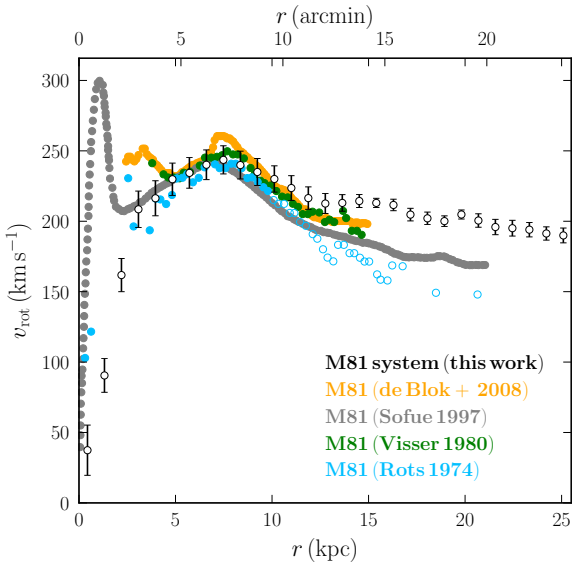

Figure 3.15: Rotation curves of the M81 galaxy from the literature, compared to that of the M81 system in the inner 25 kpc. The *open circles* of Rots (1974) correspond to the approaching side of the galaxy.

they are interacting. We will discuss this scenario more in depth in this section.

The structures of the HI bridges between the three members of the system suggest strong tidal interactions between the galaxies (see van der Hulst 1979, Yun et al. 1993; 1994). These interactions have caused the truncation of the M82 disc (Sofue 1998) and the displacement of the atomic and molecular gas of NGC 3077 from its stellar component (Walter et al. 2002a). These effects suggest that the interactions between the galaxies are violent, and they are thought to be the origin of the increased star formation rates in M81, M82 and NGC 3077 (Yun 1999), in agreement with the idea proposed by Toomre & Toomre (1972) that such tidal disruptions could enhance starburst or AGN activity in the interacting galaxies. Such violent interactions require that at least some of the member galaxies have acquired a large momentum, which favours the idea that they have travelled a certain distance and have initiated an interaction with the other members with a high enough velocity. This is in agreement with numerical simulations of the major galaxies of the system (e.g. Gunn & Gott 1972, Yun 1999, Oehm et al. 2017). The simulation used in Yun (1999)* successfully reproduces both the spatial distribution of the high column density HI gas in the system, and predicts that the nearest approach of M82 and NGC 3077 to the central galaxy M81 happened respectively 220 and 280 Myr ago. This timescale is consistent with the ages of starbursts in all three galaxies, and successfully reproduces

*see an animation at http://www.aoc.nrao.edu/~myun/movie.gif

the HI northern (between M82 and NGC 3077) and southern (between M81 and NGC 3077) tidal bridges revealed by the early observations of the group. However, it is now clear that there exists a tail connecting the system to NGC 2976, hinting at an interaction between the galaxy and the system. Although a further numerical analysis is required to determine the orbit of NGC 2976, the tail mapped in HI shows an evidence that the galaxy has recently passed near the position of at least one of the system's members.

The same hypothesis can be formulated, although with less confidence, for IC 2574; the galaxy may have crossed the path of at least some of the galaxies in the system. Indeed, multi-wavelength studies of IC 2574 have revealed that the galaxy has undergone two significant starburst events in the past $\sim$ 300 Myr (Pasquali et al. 2008, Weisz et al. 2009). Although these starbursts were attributed to stellar feedback in the galaxy, there is a possibility that its recent interaction with the system may have somehow contributed to enhance its star formation activity.

Also, the existence of the gas complex HIJASS J1021+68 – previously classified as an optically dark galaxy – and its connection with IC 2574 further supports this hypothesis of interaction of IC 2574 with the system. In fact, Boyce et al. (2001) hinted that HIJASS J1021+68 is a possible tidal dwarf galaxy in which star formation has not begun. The present observations (bottom panel of Fig. 3.6) revealed additional clouds in the neighbourhood of HIJASS J1021+68, and an HI envelope of IC 2574 that seems to point towards the tidal dwarf. These new features suggest that HIJASS J1021+68, as well as the neighbouring clouds, may in fact be a complex of HI gas that was initially in IC2574.

While most of the observational features of the group revealed in this work corroborate existing numerical simulations, it is not clear what the role of IC 2574 is with respect to the evolution of the M81 system. There is no direct evidence of a past interaction between the galaxy and the system, and one can only speculate from the observations. Part of the scenario is supported by existing numerical simulations, but further studies are required to account for the newly discovered low column density features. In particular, the nature of the HI complex west of IC 2574 (including HIJASS J1021+68) is unclear, and this region of the group will be investigated more in detail in an upcoming paper. As stated in Section 4.2, additional DRAO observations are underway, and will be presented in subsequent papers. These observations will undoubtedly unveil more HI features of the M81 group, that will help to better constrain numerical models of the dynamical evolution of the group (e.g., Oehm et al. 2017).

3.6 Conclusions

We used the DRAO synthesis telescope to map a 25 squared degrees area of the HI in the M81 group. The aim of the observations was to make a full census of the HI in the M81 system and the eastern region extending to the "isolated" galaxy IC 2574. Similarly to previous HI observations of the group, we found that the interacting three major galaxies of the group – M81, M82 and NGC 3077 – are connected through HI bridges and intergalactic HI clouds. We also mapped the full extent of the western HI arm connecting the three galaxies to NGC 2976, the fourth galaxy of the group located at a projected distance of 87.3 kpc southwest of M81. We have mapped, to a higher resolution than the previous GBT observations of Chynoweth et al. (2008), the gas clouds residing in the space between the M81 system and the arm. The observations revealed that what was previously thought, from the GBT observations, to be an extended cloud is in fact a complex of small clouds filling the space between the arm and the "main body" of the system.

The galaxy HIJASS J1021+68, previously detected with the 76m Lovell (Boyce et al. 2001, Lang et al. 2003) and the 100m GBT (Chynoweth et al. 2008) single-dish telescopes, was resolved in the present observations. The DRAO mosaic in the present work suggests that the connection between the galaxy and IC 2574 (previously hinted by Boyce et al. 2001) is through a "filament" of small clouds spanning the space between the two galaxies.

Reprocessing the VLA mosaic of de Blok et al. (2018b) with the Effelsberg single-dish data in lieu of the GBT as the authors did, we have obtained a datacube less affected by artefacts, and from which the MW HI emission could be subtracted. We have mapped three previously detected clouds to a larger extent, and their respective measured HI masses reveal that we have recovered more HI fluxes that were undetected in the VLA-only and VLA+GBT mosaics.

Accounting for the ordered motion of the HI gas around the M81 galaxy, and assuming that all gas and galaxies lie in a common rotating system, we have derived the rotation curve of the system using the tilted-ring model. This revealed that the dynamical centre of the system is located at a projected distance of about 4.7 kpc east of M81, and at systemic velocity of -5.0 km s^{-1}. The average inclination and position angle of the common plane of the system gas are $i = 62.^{\circ}0 \pm 9.^{\circ}1$ and $\phi = 346.^{\circ}7 \pm 8.^{\circ}0$, respectively. The rotation curve of the system is observed to be roughly constant over a large range of radii, with a prominent wiggle associated to M82, as if the outermost gas and galaxies were rotating at the same speed as the inner disc of M81. Although the velocities of the approaching and receding sides of

the system differ, the flat trend corroborates the assumption of a large-scale rotating system dominated by M81. Our idealised rotating tilted-ring model is accompanied by a non-negligible radial motion, perhaps highlighting the streaming of outer gas and galaxies with respect to M81.

As the mapping at DRAO is still being performed, the sensitivity at the vicinity of IC 2574 will be increased. That will allow us to study the HI environment of the dwarf galaxy more precisely, and investigate better its relation with HIJASS J1021+68, and the possible relation with the main M81 system. Future articles from this series will particularly focus on this analysis.

Acknowledgments

The authors are very grateful to the staff at DRAO, particularly to Operations Manager Dr. Andrew Gray for his flexibility and assistance in observing the many fields and gathering archived data for our work. We thank Prof. Tom H. Jarrett for providing the *WISE* stellar masses of the main galaxies of M81 in Table 3.2. We acknowledge Dr. Kelley M. Hess for her enormous contribution in making the interactive 3D map presented in Fig. 3.13. Kelley provided us with a step-by-step guide and advice on how to improve the display of the rendering. We also thank Prof. Jacqueline van Gorkom for the interesting discussions, which has certainly added value to the quality of the paper. The comments of the anonymous referee were very useful and helped to improve the quality of the present work, and for that we are grateful to them. The work of CC is based upon research supported by the South African Research Chairs Initiative (SARChI) of the Department of Science and Technology (DST), the South African Radio Astronomy Observatory (SARAO) and the National Research Foundation of South Africa (NRF). The research of AS has been supported by SARChI and SARAO fellowships. The research of LC is supported by the Comité Mixto ESO-Chile and the DGI at University of Antofagasta.

Chapter 4

A $5^\circ \times 5^\circ$ deep HI survey of the M81 group: II. HI distribution and kinematics of IC 2574 and HIJASS J1021+68

Abstract

We analyse the eastern region of a $5^\circ \times 5^\circ$ deep HI survey of the M81 group containing the dwarf galaxy IC 2574 and the HI complex HIJASS J1021+68, located between the dwarf and the M81 system. The data show that IC 2574 has an extended HI envelope that connects to HIJASS J1021+68 in the form of a filament of small clouds. We argue, based on the morphology of the clouds forming HIJASS J1021+68 and its velocity distribution, that the complex is not a dark galaxy as previously suggested, but is instead a complex of clouds either stripped from, or falling onto the primordial HI envelope of IC 2574. We also use the deep HI observations to map the extended HI envelope around IC 2574 and, using a 3D tilted-ring model, we derive the rotation curve of the galaxy to an unprecedented extent. Combining the obtained rotation curve to higher resolution curves from the literature, we constrain the galaxy's dark matter halo parameters.

4.1 Introduction

The most widely accepted models of galaxy formation, the standard Λ cold dark matter (ΛCDM) and the hierarchical clustering model, predict that massive early type galaxies form through mergers of smaller, late type galaxies (e.g., Peebles 1965,

Press & Schechter 1974, Searle & Zinn 1978, Blumenthal et al. 1984). The models also predict the abundance of low-mass halos mostly in the form of satellites around giant spirals (e.g., Moore et al. 1999). Although observational studies of galaxy distributions in the nearby Universe – particularly in galaxy clusters and groups – recover fewer low-mass dwarf galaxies than actually predicted by the models (Klypin et al. 1999, Moore et al. 1999), the statistics show that dwarfs remain the most abundant type of galaxies in the nearby Universe (e.g., Ferguson & Binggeli 1994, Bell et al. 2003, Oppenheimer et al. 2010). For example, the Local Group is composed of over 40 dwarf galaxies, while only containing three normal size spirals (e.g., Mateo 1998, McConnachie 2012). The same trend is observed in the M81 group, where the number of detected low-mass galaxies is far greater than the number of giant spirals (e.g., Chiboucas et al. 2009). This makes dwarf galaxies an important tracer of environmental effects (e.g., Drinkwater et al. 2003), and their study is crucial for understanding the galaxy formation and evolution processes.

Because of their low mass, dwarf galaxies – particularly late-type dwarf galaxies – are slow rotators with their maximum rotation velocity usually below 80-100 km s^{-1} (e.g. Côté et al. 1991, Carignan & Purton 1998, Oh et al. 2011). Furthermore, they present more slowly rising rotation curves as compared to massive spirals (although detailed studies show a diversity in the shapes of their rotation curves; e.g., Swaters et al. 2009, Oman et al. 2015), a result of their low baryon content (e.g., lack of important bulge component) and high gas fractions. In the context of understanding the dark matter (DM) distribution in galaxies, the low baryon fraction of dwarf galaxies makes them interesting to study: because their inner regions tend to have higher fractions of DM (as compared to spirals), the uncertainties related to constraining their DM inner halos are minimised. Several observational studies have shown that late-type dwarf galaxies are usually best described by a cored profile (e.g., Moore 1994, Flores & Primack 1994, de Blok et al. 2001, Swaters et al. 2003, Oh et al. 2011), that is, their DM halos are better characterised by an approximately constant density core. This is in contrast with the ΛCDM model, which predicts a steeply cusped DM density distribution (Dubinski & Carlberg 1991, Navarro et al. 1996b; 1997, Moore et al. 1999). A detailed review of this discrepancy between observations and the model, known as the "cusp-core" problem, is given in de Blok (2010).

In an effort to minimise observational systematic uncertainties (such as beam smearing) that may contribute to the discrepancy of the cusp-core problem (e.g. van den Bosch et al. 2000, Simon et al. 2003, Rhee et al. 2004), high resolution line observations (mainly in HI and Hα) of dwarf galaxies have been performed over

the past few decades (e.g. Weldrake et al. 2003, Swaters et al. 2003, Simon et al. 2005). For example, the sample of the high-resolution ($\sim 6''$) THINGS (The HI Nearby Galaxy Survey; Walter et al. 2008) survey contains a few dwarfs, and other surveys such as VLA-ANGST (VLA*-ACS Nearby Galaxy Survey Treasury Project; Ott et al. 2012), FIGGS (Faint Irregular Galaxy GMRT Survey; Begum et al. 2008) and LITTLE-THINGS (Local Irregulars That Trace Luminosity Extremes-THINGS; Hunter et al. 2012) have provided high resolution HI observations of a large sample of dwarf galaxies. While these high-resolution observations allow to probe the inner regions of galaxies, their limited column density sensitivity usually does not allow to probe the galaxies' outskirts where the HI has a low column density. Particularly for IC 2574, the previous HI observations of the galaxy found in the literature have high angular and velocity resolutions (e.g., Martimbeau et al. 1994, Walter et al. 2008), but none present a hint on the existence of low column density gas around the galaxy.

Located in the nearby M81 group and at a distance of ~ 4 Mpc (Karachentsev et al. 2002b), IC 2574 is a prime example of dwarf galaxy whose rotation curve conflicts with the ΛCDM cuspy profile. The galaxy is well studied in HI, and was found by several authors to exhibit holes and shells in its HI distribution (e.g., Martimbeau et al. 1994, Walter & Brinks 1999, Weisz et al. 2009, Egorov et al. 2014). Its HI rotation curve shows a solid body-type of rotation with DM dominating its dynamics at almost all radii (Martimbeau et al. 1994), and no presence of cusp was detected in the galaxy's DM halo (Oh et al. 2008). West of the galaxy is located an HI structure – HIJASS J1021+68 – identified as a dark galaxy (Boyce et al. 2001, Lang et al. 2003), whose systemic velocity roughly coincides with that of IC 2574. The structure was observed to be marginally connected to IC 2574 through a filament (Boyce et al. 2001). However, due to the low spatial resolution of the observations, it is not clear what the nature of the connection is. A good example of this is what was thought to be a filament between M31 and M33 (Braun & Thilker 2004) turned out to be discrete clouds when higher spatial resolution data became available (Wolfe et al. 2013).

Using the DRAO telescope[†], we have mapped, to a high column density sensitivity, a $5^\circ \times 5^\circ$ region of the M81 group covering the M81 interacting system (M81, M82 and NGC 3077), NGC 2976 and IC 2574 (Sorgho et al. 2019b, hereafter Paper I) during $\sim$3000 hours of observation. The observations allowed us to *i)* map the HI arm connecting the M81 system and NGC 2976, *ii)* resolve the HI clouds adjacent to

[*] https://science.nrao.edu/facilities/vla/
[†] https://www.nrc-cnrc.gc.ca/eng/solutions/facilities/drao.html

the arm, and also *iii)* resolve, for the first time, the HIJASS J1021+68 cloud located west of IC 2574 (see Fig. 6 of Paper I). In this second paper of the series, we focus on the subset of the observations data covering IC 2574 and HIJASS J1021+68, and present both the extended emission around IC 2574, and a kinematical analysis of its HI gas. We take advantage of the high column density sensitivity of the observations to extend the rotation curves of the galaxy found in the literature. We also present and discuss the HI distribution and kinematics of HIJASS J1021+68. The paper is organised as follows: in Section 4.2 we summarise the observations and the data reduction method and present the global HI profiles and moment maps of the galaxy in Section 4.3. We next derive its rotation curve and construct its mass models in Section 4.4, and summarise the results in Section 4.5.

4.2 Observations and data reduction

The observations were conducted in 2016/2017 using the DRAO telescope, and are extensively described in Paper I. Twenty different fields covering the IC 2574 galaxy, M81 and its interacting counterparts M82 and NGC 3077, as well as NGC 2976 were observed for 144 hours each during the observational campaign, for a total of nearly 3000 hours in total. To further increase the sensitivity of the data in certain key areas such as the regions containing respectively the M81 triplet and IC 2574, 10 additional fields were retrieved from the DRAO archive and added to the observations, bringing the total number of fields to 30. These fields were calibrated, reduced and processed individually before being combined into a single mosaic of $1024 \times 1024 \times 256$ pixels in size, with spatial and spectral pixel widths of $20''$ and 3.3 km s^{-1}, respectively. Because of the limitation of the DRAO as an interferometer when it comes to accurately recover the fluxes of large-scale structures (in this case, structures larger than $56'$), we have combined the data to the EBHIS HI data (Winkel et al. 2016) to correct for short-spacing. The EBHIS data were obtained with the 100m Effelsberg single-dish telescope, and were shown to present a good overlap with the DRAO data in the *uv* plane. The resulting data has a 1σ sensitivity of 5.3 mJy/beam around IC 2574, for a spatial resolution of $61'' \times 59''$ and a spectral resolution of 5.2 km s^{-1}. In column density units, this is equivalent to 2.6×10^{19} cm^{-2} over 16 km s^{-1} and at a spatial resolution of 1.2 kpc. To further increase the sensitivity of the observations, we smoothed the datacube down to a resolution of $108'' \times 108''$ (or 2.1 kpc at the distance of IC 2574).

The last step of the data processing consisted of subtracting the Milky Way HI emission from the IC 2574 emission. Because of the low systemic velocity of the

Parameter	Value
R.A (J2000)	$10^h28^m23\overset{s}{.}5$
Dec. (J2000)	$68^d24^m43\overset{s}{.}7$
Morphological type [a]	SABm
Distance[b]	4.02 Mpc
Optical 25th mag. diameters [c]	$13\overset{'}{.}2 \times 5\overset{'}{.}4$
Total B Magnitude [c]	10.84 mag
Stellar mass [d]	$0.4 \times 10^9\,M_\odot$
Inclination [e]	60°
Position angle [f]	50°

Table 4.1: Optical parameters of IC 2574. References: [a]RC3 catalogue (de Vaucouleurs et al. 1991); [b]Karachentsev et al. (2002a); [c]Karachentsev et al. (2004); [d]Derived from the *WISE* photometry (Jarrett et al., *in prep.*); [e]Nilson (1973); [f]Appleton et al. (1981).

galaxy, the data was contaminated by the foreground Galactic HI emission. We adopted a technique similar to that described in Chemin et al. (2009), which consisted of subtracting a modelled Galactic emission from the data. The technique was successful in mitigating most of the foreground HI in the data. A complete description of the observations, the calibration and post-calibration processing procedures can be found in Paper I. The smoothed cube, which is used in this work, has a 1σ noise level of $1.2 \times 10^{18}\,cm^{-2}$ (around IC 2574) over 16 km s^{-1} and a spatial resolution of 2.1 kpc (at the distance of IC 2574).

4.3 HI properties

4.3.1 HI emission in IC 2574

The global HI profile of IC 2574, computed by integrating on the HI emission inside the HI radius (see below) of the galaxy, is presented in Fig. 4.1. The total HI line flux measured for the galaxy is 367 ± 21 Jy km s^{-1}, which corresponds to an HI mass of $(1.4 \pm 0.1) \times 10^9\,M_\odot$. For comparison, the HI flux of the galaxy published in Martimbeau et al. (1994) and derived using the WSRT (Westerbork Synthesis Radio Telescope) is 286 Jy km s^{-1}, i.e, ∼22% lower than the flux derived in the present work. The relatively high HI mass of IC 2574 makes the dwarf a gas rich galaxy, with a gas fraction of 3.5 ± 0.1. The systemic velocity of the galaxy derived from the HI profile is 49.5 ± 0.8 km s^{-1}, with a velocity width measured at 50% of the peak intensity of 106.7 ± 5.3 km s^{-1}. The profile shows that the galaxy is quite asymmetric, with more HI flux residing on its approaching (southwestern) side

than on the receding (northeastern) side. The foreground Galactic HI mainly affects the rising part of the approaching side, but the shape of the profile shows that the Milky Way subtraction procedure successfully removed most of the contamination. In Fig. 4.2 we show the HI surface density profile of the galaxy, from which we derive an HI diameter of 20.8′ (or 24.4 kpc) at the $1\,M_{\odot}\,pc^{-2}$ isophote.

We present in Fig. 4.3 the total HI intensity (zeroth moment) map of IC 2574 obtained from the 1.8′ (2.1 kpc) resolution datacube. In Fig. 4.4 we show the corresponding velocity field (first moment) and the velocity dispersion (second moment) maps. These moment maps were computed with the MOMENT task of MIRIAD using a mask previously created at a 5σ clipping level with the smooth and clip algorithm of SOFIA (Serra et al. 2015). We have constructed the mask such that the emission from the extended HI envelope of the galaxy (see Section 4.3.2) is excluded, and only the gas contributing to the rotation of the galaxy is accounted for. This implies that no spatial smoothing was performed on the datacube, and only a spectral smoothing to twice the channel width of the cube was done before the final mask was derived. More explicitly, this means that the mask used to compute the moment maps was obtained by combining two masks: one created from the original datacube, and the other at twice the original velocity resolution. Consistently with the maps presented in earlier works (e.g., Martimbeau et al. 1994, Walter & Brinks 1999, Oh et al. 2008, de Blok et al. 2008), the velocity maps in Fig. 4.4 show non-circular and random motions in the inner regions of the galaxy. These are likely the effects of the dynamics of the expanding HI shells and holes residing in the galaxy (Walter & Brinks 1999).

4.3.2 Extended HI emission around IC 2574

To get a full view of the extended HI envelope of IC 2574, we have built a mask that includes the faint emission around the galaxy. This was done by lowering the detection flux threshold to 4σ and expanding the number of smoothing kernels used to build the mask. The corresponding HI intensity map is presented in Fig. 4.5. The map shows a very extended HI emission around the galaxy, mostly to its south. To ensure that the emission in the envelope is not just an artefact or foreground emission from the Milky Way, we have extracted spectra in boxes taken inside and outside the envelope (see Fig. 4.5). The spectra show that: i) most of the emission is located outside the velocity channels affected by Galactic emission, and ii) a comparison with spectra outside the envelope shows that such emission is not seen everywhere around the galaxy. Furthermore, the velocity distribution in the envelope (Fig. 4.6) suggests that most of the low density gas, especially the southern and western concentrations, is roughly rotating with the galaxy. The extension to the south is more or less aligned

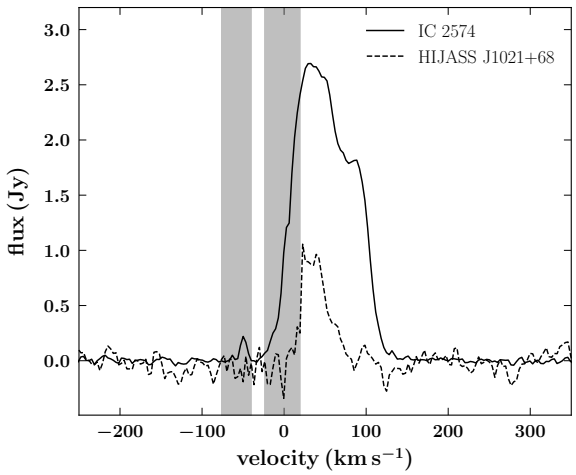

Figure 4.1: The global HI profile of IC 2574 (*full line*) and HIJASS J1021+21 (*dashed line*). The grey areas show the velocity ranges that are contaminated by foreground emission.

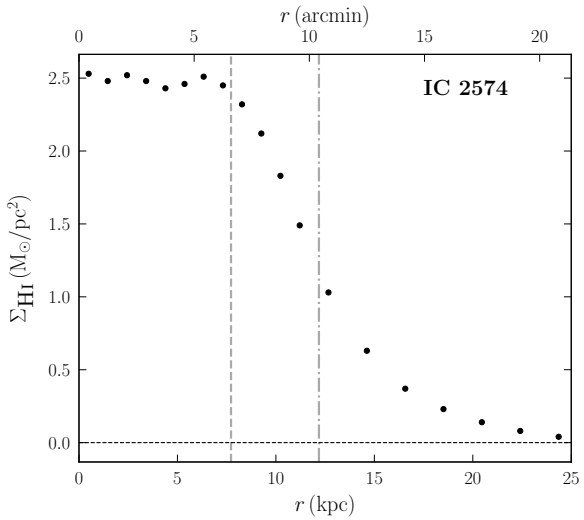

Figure 4.2: HI surface density profile of IC 2574. The *dashed* and *dash-dotted* vertical lines represent respectively the optical radius measured at the 25th B magnitude and the HI radius measured at $1\,M_\odot\,pc^{-2}$.

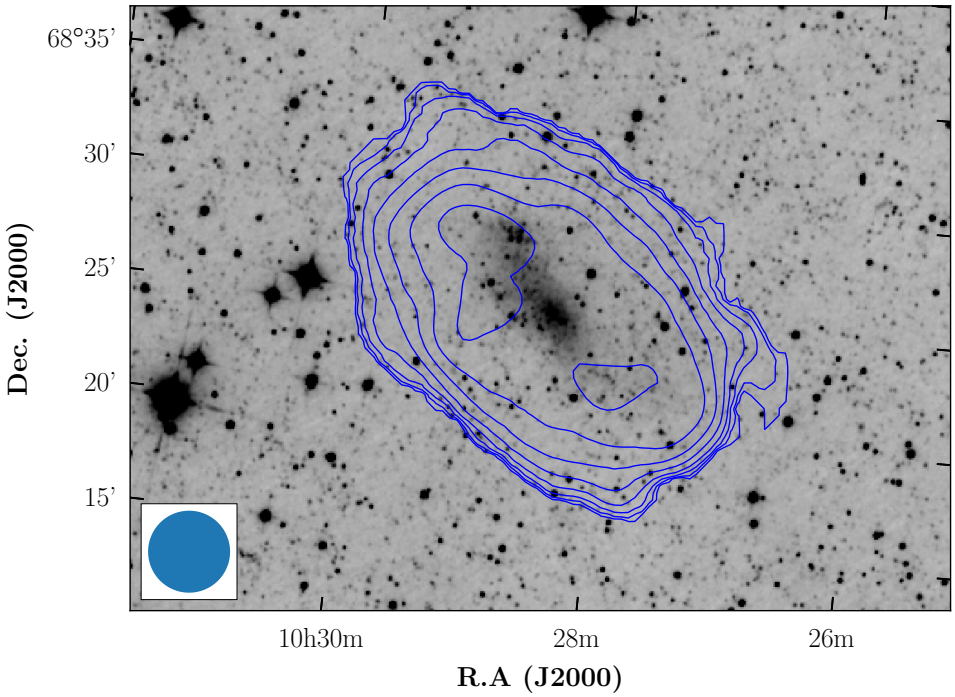

Figure 4.3: Column density map of IC 2574 overlaid on a *WISE* W1 grayscale image. Contours are $1, 2, 4, \ldots, 128 \times 10^{19}\,\mathrm{cm}^{-2}$. The blue circle at the bottom left corner shows the synthesised beam.

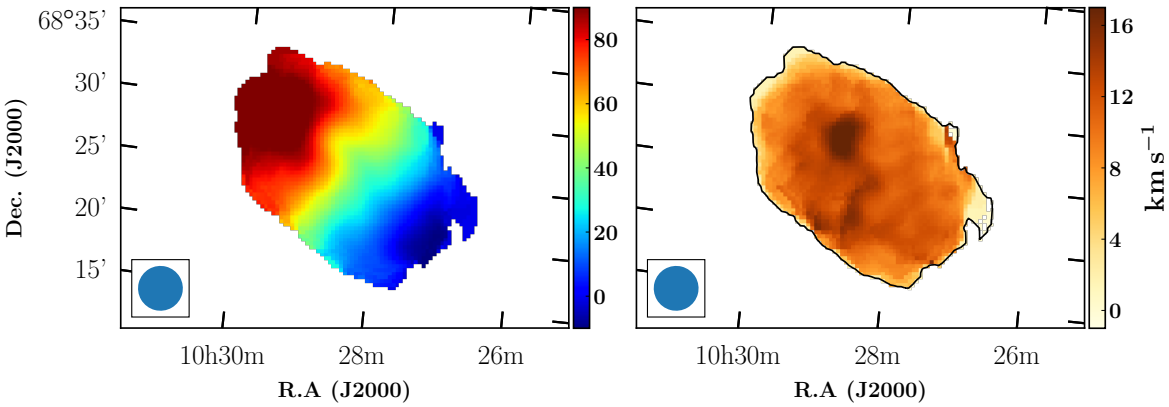

Figure 4.4: Velocity (*left*) and velocity dispersion (*right*) maps of IC 2574. Contours of these maps overlaid on optical image are given in Figs. C.1 and C.2.

with the minor axis of the galaxy, and the gas located in that region is at systemic velocities; the gas along the western edge sits on the approaching side of the galaxy, although it appears to be lagging behind. This further supports the idea that the low density gas detected around IC 2574 forms an extended envelope around the galaxy.

4.3.3 HI distribution in HIJASS J1021+68

Located at approximately 54 kpc west of IC 2574, HIJASS J1021+68 is a complex of gas clouds previously identified as a dark galaxy in the HIJASS catalogue (Boyce et al. 2001). The complex is not much studied in the literature, and no stellar counterpart has been reported. Fig. 4.7 shows an HI map of the region containing IC 2574 and the gas complex. HIJASS J1021+68 appears to be a complex of three major clouds (and a small cloud south of the central cloud), with an apparent connection between the central and the northern clumps. Its total HI mass, as derived in Paper I, is $(6.5 \pm 1.0) \times 10^7\,\mathrm{M}_\odot$. Its global HI profile is shown in Fig. 4.1, computed by integrating the emission from the whole complex. The systemic velocity and velocity width at 50% of the peak intensity of HIJASS J1021+68, derived from the global profile, are respectively 35.7 ± 2.9 km s^{-1} and 30.4 ± 5.8 km s^{-1}. This shows that HIJASS J1021+68 has very little rotation (unless it is seen fortuitously almost face-on).

In a search for a possible stellar counterpart for the gas complex, we collected and looked at images of the clouds in three different bands in the hope of finding a star forming region or an associated stellar population. Fig. 4.8 shows the HI intensity map of the complex, overlaid on GALEX (Galaxy Evolution Explorer; Martin et al. 2005) far-UV, optical R-band, and infrared *WISE* (Wright et al. 2010) W1 images. The R-band image is a mosaic of four different image tiles taken from the PS1 (*aka* PanSTARRS1: Panoramic Survey Telescope and Rapid Response System; Chambers et al. 2016, Flewelling et al. 2016) catalogue* of images. At the spatial position of HIJASS J1021+68, none of the images present a structure that may be a possible counterpart to the complex. Considering the *WISE* image whose W1 band has a surface brightness noise of 23.2 mag arcsec^{-2} (μJy/arcsec^2) per pixel (Jarrett et al. 2012), and considering a minimum of 1000 pixels (the angular pixel size being 2.75″), we find that the upper limit of the noise in the image shown in the right panel of Fig. 4.8 is about 0.015 μJy/arcsec^2 (or 25.8 mag arcsec^{-2}). Converting this surface brightness level to luminosities yields about 0.43 $\mathrm{L}_\odot$/pc^2, which corresponds to an upper limit on stellar mass of $1.4 \times 10^5\,\mathrm{M}_\odot$ assuming an exaggerated mass-to-light ratio of 1 $M_\odot/L_\odot$. The non-detection of stellar counterparts down to this level most

*Accessible via MAST: http://catalogs.mast.stsci.edu/

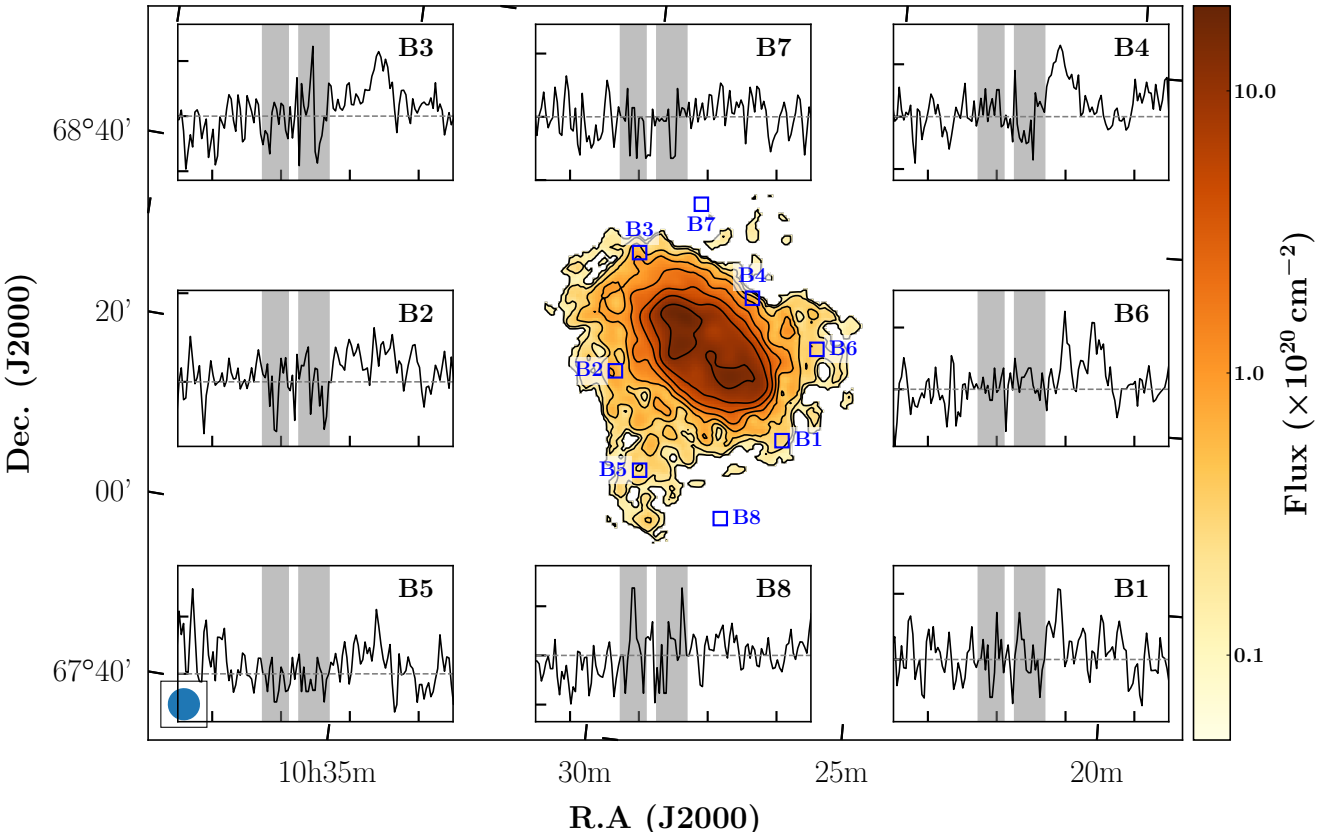

Figure 4.5: The extended HI envelope around IC 2574. The plots in the subpanels B1, B2, ..., B8 are the spectra (flux vs. velocity) extracted in and outside the HI envelope at the positions delimited by boxes of corresponding names. The x-axis ticks of the plots are -150, -50, 50 and 150 km s^{-1}. The grey area shows the velocity range affected and processed for Galactic emission. The contours are $1, 2, 4, \ldots, 128 \times 10^{19}\,cm^{-2}$. The blue circle at the bottom left corner shows the synthesised beam.

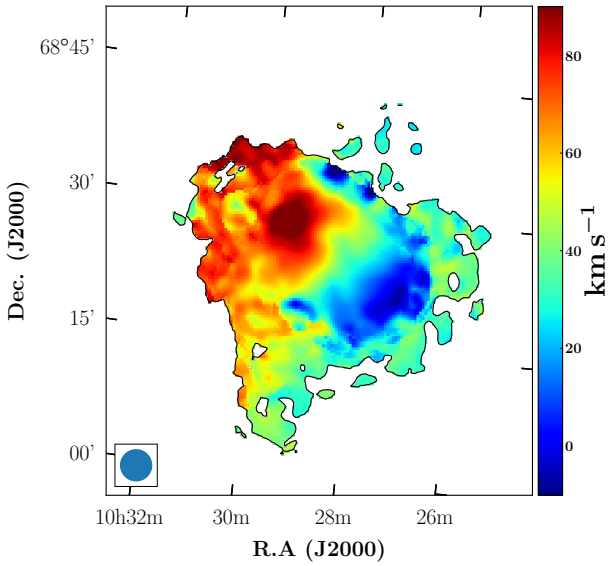

Figure 4.6: Velocity distribution including the HI envelope around IC 2574.

likely suggests that no star formation has taken place (*yet*) in the gas clouds. We also note that the M81's dwarf galaxy survey of Chiboucas et al. (2009) – and follow-up in Chiboucas et al. (2013) – with the CFHT has detected no stellar counterparts at the position of HIJASS J1021+68.

4.4 HI kinematics

4.4.1 Rotation curves of IC 2574

Tilted-ring modelling

Using the 3D tilted-ring model fitting tool 3D BAROLO (Di Teodoro & Fraternali 2015), we derived the rotation curve of the galaxy. Unlike the traditionally-used ROTCUR (Begeman 1989) task in GIPSY (van der Hulst et al. 1992) which derives the rotation curve from the two-dimensional velocity field, 3D BAROLO takes as input the three-dimensional HI datacube and fits a 3D tilted-ring model to it. In fact, because of the relatively low spatial resolution of the data (only $\sim$ 6 beams across IC 2574), rotation curves derived from low-resolution velocity fields are generally sensitive to beam smearing effects, which tend to underestimate the velocities in the inner regions of galaxies (e.g. Swaters et al. 2009, Lelli et al. 2010). However, the 3D fitting procedure was shown to be less sensitive to these effects, and describes more

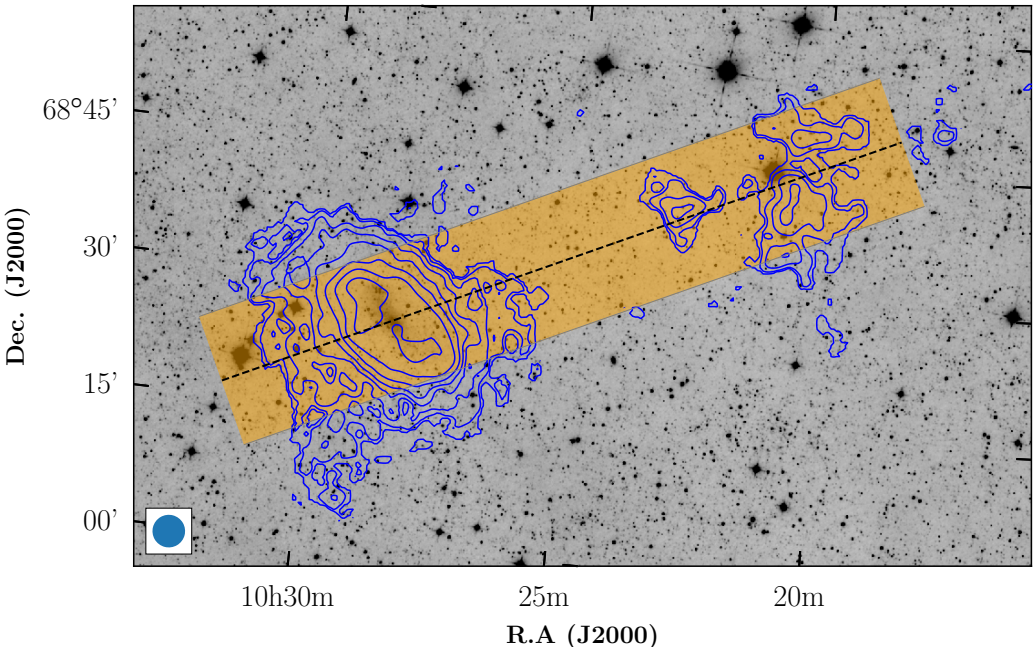

Figure 4.7: Total HI intensity map of the region covering IC 2574 and HIJASS J1021+68 (*blue contours*) overlaid on a *WISE* W1 (3.4μm) grayscale image. The *dashed line* shows the position-velocity slice of the diagram in Fig. 4.14 (see Section 4.4.2) and the *orange shaded area* the width of the slice (15′). The contours are $1, 2, 4, ..., 128 \times 10^{19}\,\mathrm{cm}^{-2}$.

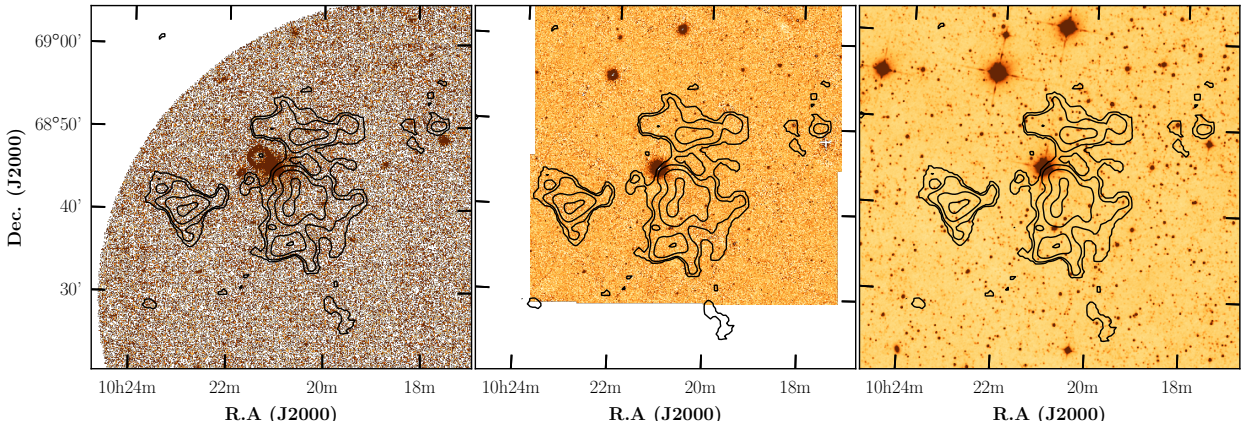

Figure 4.8: Total HI intensity map of HIJASS J1021+68 (*black contours*) overlaid on GALEX UV (*left panel*), optical R-band (*middle panel*) and infrared *WISE* (*right panel*) images. The contours are $1, 2, 4, 8 \times 10^{19}\,\mathrm{cm}^{-2}$.

accurately the rising parts of rotation curves (e.g., Di Teodoro & Fraternali 2015, Sorgho et al. 2019a).

We supplied to the fitting program the MW-subtracted HI datacube of IC 2574 and the 5σ mask derived in Section 4.3.1 with SoFiA, and provided the optical values of the inclination and position angle as initial guesses. As for the systemic velocity and the dynamical centre, we guessed the initial values from the velocity field in Fig. 4.4. We have run the program for the entire galaxy (both sides), allowing it to run twice: a first stage during which it allows all the kinematical parameters to vary, then performs a parameter regularisation where the parameters are interpolated, and a second stage during which these parameters (except the rotation velocity) are kept fixed to the fitted values. The rings in the tilted-ring model were chosen to be $50''$ wide (i.e, about half the beam size) in the inner regions of the galaxy, and because of the non-regular shape of the object (see Fig. 4.4), a ring width of $100''$ was chosen in the outer regions. Also, 3D BAROLO lets the user choose the fitting function (polynomial or Bezier) for the inclination and the position angle, and a series of tests has shown that the best results are obtained with a third order polynomial function.

The dynamical centre and systemic velocity obtained from the fit are respectively $(\alpha, \delta) = (10^{\rm h}28^{\rm m}36\overset{\rm s}{.}1, 68^{\rm d}25^{\rm m}39\overset{\rm s}{.}1)$ and 45.4 ± 0.7 km s^{-1}. To ensure the consistency of these values, we have used ROTCUR to re-estimate these values from the velocity field in Fig. 4.4, and obtained the sensibly similar value of $(10^{\rm h}28^{\rm m}43\overset{\rm s}{.}3, 68^{\rm d}25^{\rm m}34\overset{\rm s}{.}3)$ for the dynamical centre, but a higher value of 56.3 ± 2.1 km s^{-1} for the systemic velocity. This difference in systemic velocity values can however be attributed to the asymmetric shape of the galaxy's global profile. Indeed, the velocity field used was derived by weighting the velocity at each point of the galaxy by the intensity of the emission at that velocity, and one therefore expects the resulting systemic velocity to be biased towards the lower peak of the asymmetric profile.

Fixing the centre and systemic velocity of the galaxy to the above values derived with 3D BAROLO, we have run the program two more times to estimate the variation of both the position angle and inclination for the approaching and receding halves, respectively. These are shown in the left panel of Fig. 4.9. Except a few minor differences, we note a good agreement between the sides and the resultant model for the variations of both the inclination and the position angle. Indeed, we see that for all the 3 models, there is a slight decrease in the variation of the position angle with the radius, while the inclination tends to be high ($\sim 80°$) in the centre and in the outskirts of the galaxy, with the lowest values found in the region $\sim 4 - 10$ kpc. This similarity in the variations of the models' geometric parameters suggests a good

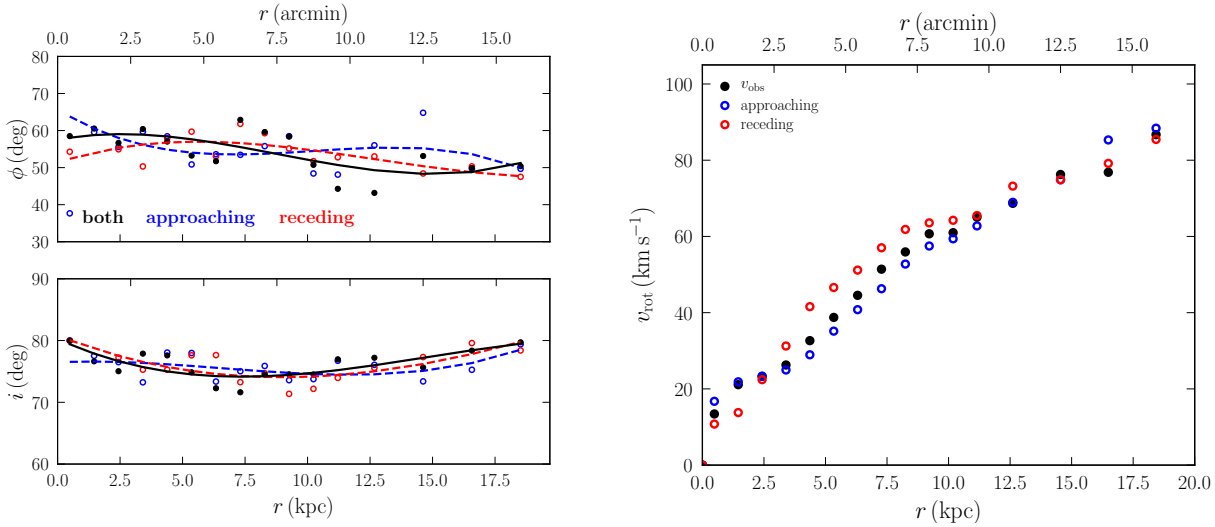

Figure 4.9: *Left:* Tilted-ring model of IC 2574 obtained from the 3D BAROLO fitting program. *Right:* rotation curve of IC 2574 derived using the parameters of the left panel.

kinematical symmetry of the galaxy's disc.

We ran the program once more on the approaching and then on the receding half of the galaxy, with all the geometrical parameters fixed to those obtained for the overall model. The three rotation curves are presented in the right panel of Fig. 4.9 where, as expected, the rotation of the galaxy seems to follow a solid-body type of rotation. Also, similarly to the variations of the kinematical parameters, we note that there is a good agreement between all the models.

Asymmetric drift correction

Because of the low mass and rotation velocity of IC 2574, one expects the rotation curve of the galaxy to be underestimated because of the effects of the asymmetric drift (e.g., Valenzuela et al. 2007, Dalcanton & Stilp 2010, Pineda et al. 2017). To obtain the true circular velocity of the galaxy, we use the Eq. (4.227) of Binney & Tremaine (2008) with the assumption that the product $v_r v_z$ is independent of z, and that the thickness of the disc is constant; we write (also see Côté et al. 2000, Carignan et al. 2013, Chemin et al. 2016)

$$v_{\rm circ}(r) = v^2_{\rm obs}(r) - r\,\sigma^2(r)\left[\frac{d}{dr}\ln\Sigma(r) + \frac{d}{dr}\ln\sigma^2(r)\right] \tag{4.1}$$

where $v_{\rm obs}(r)$, $\sigma(r)$ and $\Sigma(r)$ are respectively the observed rotational velocity, the observed line-of-sight dispersion velocity and the total gas surface density at a radius

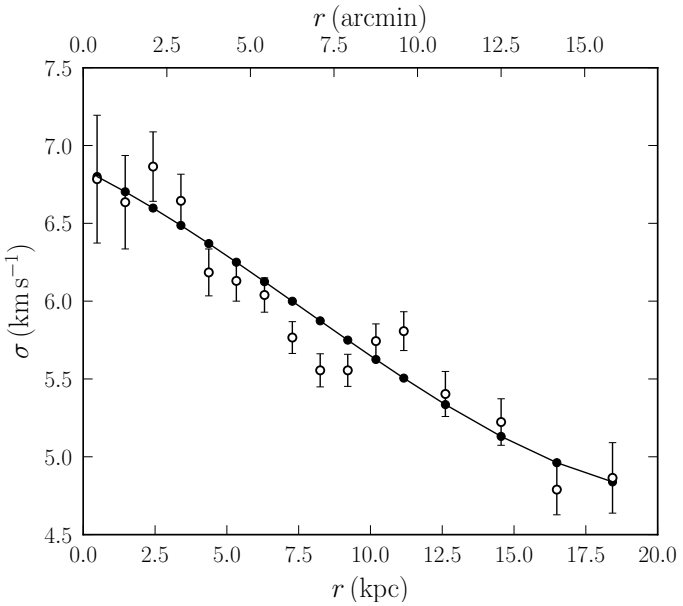

Figure 4.10: Velocity dispersion profile of IC 2574. The empty dots represent the observed velocity dispersions while the black dots and the line show the *smoothed* velocities used to determined the asymmetric drift corrections.

r. The line-of-sight dispersion velocity was derived by fitting ellipses to the second moment map of the galaxy, and its variation is given in Fig. 4.10. The velocities were corrected from instrumental broadening, and the profile was smoothed with a third order polynomial to make it less sensitive to the small-scale, local fluctuations. Following Dalcanton & Stilp (2010), the total gas surface density was assumed to be 1.4 times higher than the HI surface density of Fig. 4.2, where the factor 1.4 allows to approximately correct for the helium and heavier elements. In Fig. 4.11 we show a comparison of the observed rotational and circular velocities, and those derived in previous studies in the literature. We also show on the plot the asymmetric drift velocity, given by the second term of the right-hand side of Equation (4.1). As expected, the difference between the observed and circular velocities is highest in the outer regions of the galaxy, where the pressure due to the random motions in the disc is mostly exerted.

The rotation curves derived in the present work extend farther than those in the literature, and overall agree well with the THINGS intensity-weighted mean (IWM, Oh et al. 2008) and Martimbeau et al. (1994)'s rotation curves in the central regions of the galaxy. However, the velocities of the derived rotation curves in the inner regions of the galaxy (< 2 kpc) are overestimated by 11% to 27% when compared to these higher resolution curves. In the region $\sim 10 - 13$ kpc, the derived rotation

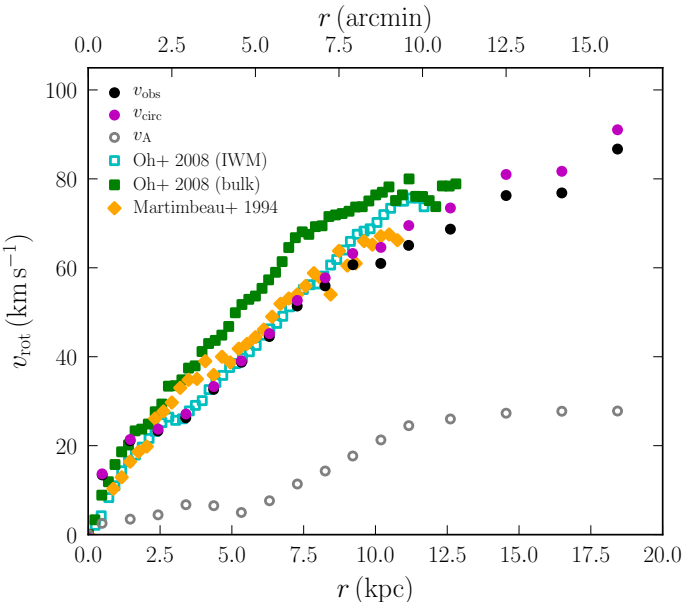

Figure 4.11: Rotation curves of IC 2574 compared with the literature.

curves are slightly below the THINGS curve, but agree with the latter within the error bars (not shown for clarity). The figure also shows the THINGS bulk rotation curve from Oh et al. (2008), derived from the galaxy's HI velocity field after correcting the data for random and small-scale non-circular motions. The bulk rotation curve is above the curves derived in this work in the region > 2.3 kpc, but its last points agree with the circular velocities of the present work.

To get a comparison between the tilted-ring model and the observed kinematics of the galaxy, we have constructed a residual map of the velocity field (Fig. 4.12) by subtracting a velocity field of the model from the observed velocity field. The model velocity field was computed using the 3D BAROLO geometrical parameters and the circular rotation curve obtained after accounting for the asymmetric drift. The residual map shows the regions of the galaxy where the non-circular motions mostly affect the rotation of the galaxy, with a difference velocity between the model and the data of the order of about $10 - 25$ km s^{-1}. It also shows that the residual velocities are highest in the outermost regions of the galaxy, especially around the southwestern side.

4.4.2 HI kinematics of HIJASS J1021+68

In Fig. 4.13 we show the velocity distribution in HIJASS J1021+68. There is a slight horizontal rotation pattern in the complex, with the western side approaching the observer while the eastern side recedes. Also, the eastern clump seems kinematically

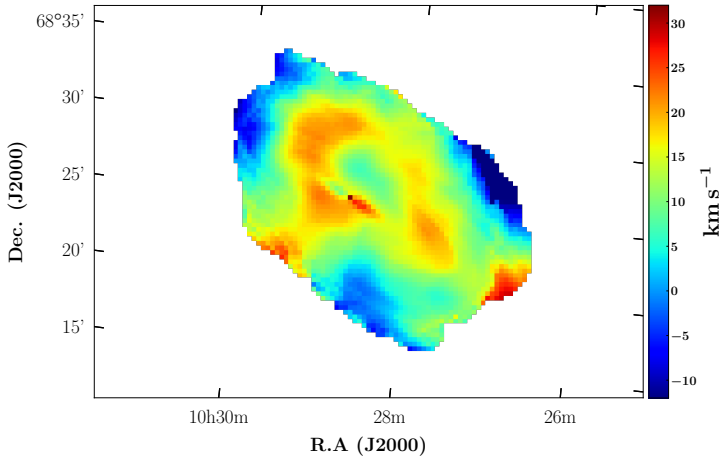

Figure 4.12: Residual velocity field of IC 2574. The regions of high residuals around the centre show where the non-circular motions influence the rotation of the galaxy.

separated from the rest of the complex, with a difference in velocity reaching ∼10 km s^{-1}. In the central and northern clouds of the complex, the velocity dispersion seems to follow the pattern of the velocity field, increasing from west to east. In the eastern cloud, the dispersion is roughly uniformly distributed with an average of $\sim 8 - 10$ km s^{-1}. Although the limited resolution of the data does not allow us to perform an in-depth kinematical analysis of the complex, the present maps show that its kinematics are not exclusively supported by rotation nor is it solely supported by dispersion; instead, the data suggest that both the rotation and the random motions of the gas complex contribute importantly to its gravitational support.

4.4.3 The nature of HIJASS J1021+68

On the nature of HIJASS J1021+68, two possibilities arise: the object is either just a complex of gas clouds, or it is a dark galaxy in which star formation has not begun yet. The first hypothesis is obvious, as the system shows no stellar counterpart, and appears to be fragmented in different clouds. However, a few observational facts argue in favour of the dark galaxy nature of the object: the apparent gradient in the velocity field and the high velocity dispersion (up to ∼14 km s^{-1}) in the atomic gas. The gradient in the velocity field, although small, suggests that the gas in the clouds complex is somewhat gravitationally bound. To confirm this, we estimated the Jeans instability mass of the complex from the column density of the data and assuming that the gas has a line-of-sight size similar to its projected size, with an average

temperature of ∼100 K; we found a Jeans mass in the range of $\sim 10^6\,M_\odot$, an order of magnitude lower than the measured total HI mass of the complex, confirming that – theoretically – the gravitational force in the gas is strong enough to balance the kinetic force due to random motions. Also, the HI kinematics of HIJASS J1021+68 present the same characteristics as those of the low-mass dwarf irregular galaxy GR8 (Carignan et al. 1990), whose gravitational support is essentially provided by rotation only in the inner regions, while it is dominated by random motions in the outer parts. Moreover, the rotation axis of the object – as given by the gradient of the velocity in Fig. 4.13 – is roughly vertical; the spatial distribution of the HI in the system suggests that its major axis is also vertical. This makes HIJASS J1021+68 a system in which the rotation axis is parallel to the major axis, and the same pattern was observed in GR8 (see Carignan et al. 1990). These kinematical similarities with GR8 show that HIJASS J1021+68 can possibly be a dark galaxy as first suggested by Boyce et al. (2001). However, for this possibility to be true, there has to be a connection between the eastern and central clouds, such that the whole complex forms a single body. Otherwise, the velocity gradient in the central and northern clouds alone (of $\sim$10 km s^{-1}) is not high enough for the gravitational force to be important. Could there be some low column density gas in the space between the two major parts of the complex that was missed by the present observations? To investigate the connections between the clouds in the complex and with the dwarf galaxy IC 2574, we plot in Fig. 4.14 a position-velocity (PV) diagram taken across the two systems. To maximise the signal-to-noise ratio, the width of the slice was taken to be $15'$, wide enough to cover most of the gas complex. Nonetheless, no apparent connection is seen between the major two parts of HIJASS J1021+68. However, the diagram reveals a set of small clouds (above the 2σ level) in the space between the two systems, most of which are not seen in the HI intensity map of Fig. 4.7. It is worth noting that the distribution of these clouds suggests that more non-Galactic clouds could exist in the contaminated velocity channels (grey band in Fig. 4.14), that were removed by the Galactic HI subtraction process. We note two elongated prominent structures in the contaminated region, respectively in IC 2574 and below HIJASS J1021+68 (at velocities of $\sim$0 km s^{-1}), which represent residuals of the Galactic HI at the peak contamination. Furthermore, the continuity of velocity in the distribution of the detected clouds suggests that the connection that the low resolution HIJASS data (Boyce et al. 2001) hinted at may be real. The western region of IC 2574's extended envelope is also seen on the western side of the galaxy, at an angular offset of about $-40'$. Although HIJASS J1021+68 was previously classified as a dark galaxy and its velocity field presents a slight horizontal gradient, the morphology of the complex

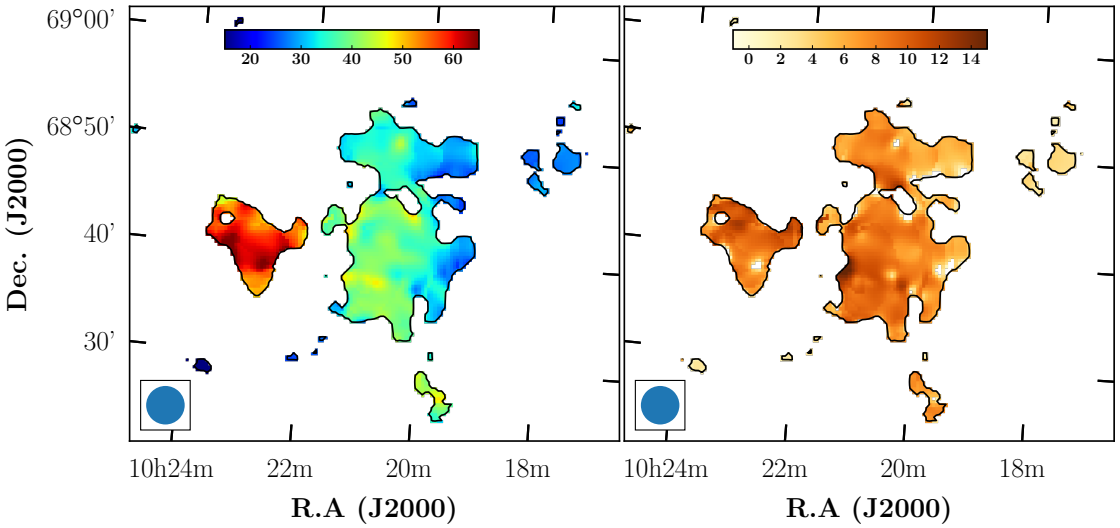

Figure 4.13: Velocity field (*left panel*) and velocity dispersion map (*right panel*) of HIJASS J1021+68.

and its apparent connection to IC 2574 strongly suggests that it may not be a dark galaxy. One possibility that could arise is that the object is, as suggested by Boyce et al. (2001), a forming tidal dwarf galaxy in which star formation has not yet begun. However, as predicted by the simulations (e.g., Bournaud & Duc 2006), tidal dwarf galaxies are more likely to form in major, gas-rich mergers. More specifically, tidal dwarf galaxies are known to generally form out of the debris residing in tidal tails of galaxies, as a result of interactions (e.g., Duc et al. 2000; 2004, Lelli et al. 2015, Lee-Waddell et al. 2016). This makes it less likely for HIJASS J1021+68 to be a tidal dwarf galaxy, since neither the optical nor the HI morphology of IC 2574 hints at the existence of a tidal tail associated with the galaxy. With the natures of dark galaxy and tidal dwarf galaxy discarded as possible natures of HIJASS J1021+68, it becomes most likely that the object is just a complex of gas clouds connected to the large envelope of IC 2574, probably stripped from, or falling onto the envelope.

4.4.4 Mass model

To construct the mass model of IC 2574, we take advantage of both the high resolution VLA data and the extended DRAO curve: we construct a *hybrid* rotation curve by combining the circular velocity rotation curve in Fig. 4.11 to that of Oh et al. (2008) plotted in Fig. 4.9. In the inner regions ($r < 13$ kpc) we consider the

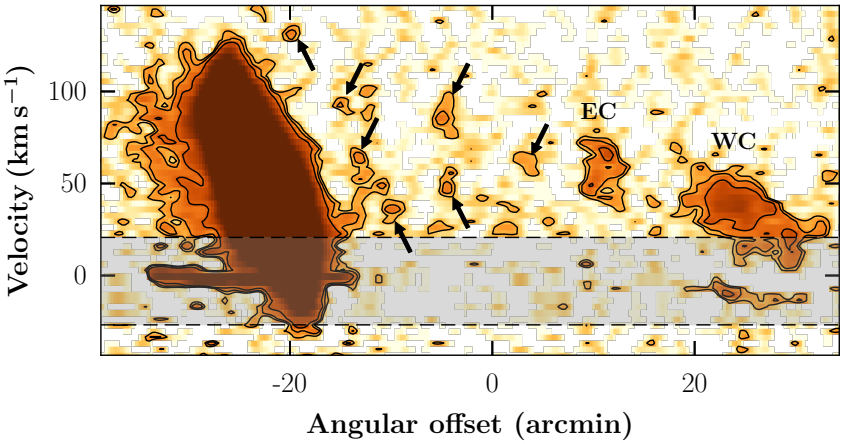

Figure 4.14: PV diagram of the region including IC 2574 (eastern structure) and HIJASS J1021+68 (the two westernmost concentrations). There exists at least 7 small blobs (indicated by arrows) in the space between IC 2574 and HIJASS J1021+68 hinting at a real connection between the two bodies. The contours represent the 2σ, 3σ and 5σ flux levels, and the grey horizontal band delimited by two horizontal lines shows the velocity range that was affected by Galactic foreground HI emission. The labels EC and WC respectively denote the eastern and western (i.e, central + northern) clouds of HIJASS J1021+68. A representation of the slice along which the diagram is taken is shown in Fig. 4.7.

high resolution curve only, while in the outer regions we consider the lower resolution DRAO curve. Also, because the THINGS curve is oversampled (two points per beam), we resampled it by dropping every second point in the curve, following the mass models of THINGS rotation curves in Chemin et al. (2011).

Baryonic component

The *WISE* (Wright et al. 2010) W1 ($3.4\mu m$) light profile of IC 2574 (from Jarrett et al., *in prep.*) is shown in Fig. 4.15. The profile suggests the absence of a prominent bulge as expected, and an attempt to perform a decomposition into different components – an exponential disc and a spherical bulge – further confirmed that the bulge contribution to the total luminosity of the galaxy is negligible, with a bulge-to-total luminosity ratio of only 6%. We therefore assume that the only stellar component of the galaxy is the stellar disc.

For the gaseous disc component, we derived the contribution from the galaxy's HI surface density presented in Fig. 4.2. We assumed a thin disc composed of neutral hydrogen and helium, and multiplied the HI surface densities by a factor of 1.4 to account for the helium and heavier elements. The total baryonic contribution to the observed rotation of the galaxy can therefore be written

$$v_{\rm baryonic} = \sqrt{\Upsilon_\star\,|v_{\rm disc}|v_{\rm disc} + |v_{\rm gas}|v_{\rm gas}}\,, \tag{4.2}$$

where $\Upsilon_\star$ is the stellar mass-to-light ratio (M/L) of the disc, $v_{\rm disc}$ the disc velocity and $v_{\rm gas}$ the velocity of the gaseous disc.

From Jarrett et al. (*in prep.*), we have obtained a W1-W2 colour of 0.089 ± 0.040 mag; following the $M_\star/L_{\rm W1}$ calibration from Cluver et al. (2014), we derived a stellar mass-to-light ratio of 0.62 ± 0.11 $M_\odot/L_\odot$. We will hereafter refer to this value as the *WISE* colour M/L value.

Dark matter component

The other major component in disc galaxies – besides the baryonic components – accounting for their total mass is the dark matter (DM). Indeed, several studies have shown that an important fraction of galaxies' mass – especially for late-type galaxies – is contained in their DM halo (e.g., Rubin et al. 1978, Kalnajs 1983, Carignan & Freeman 1985). Two main profiles are generally used to describe the halo of this unseen matter: the pseudo-isothermal model which assumes an approximately constant DM density in the centre of the DM halo, and the *cuspy* profile (Navarro et al. 1996b; 1997), commonly referred to as the Navarro-Frenk-White (NFW) profile,

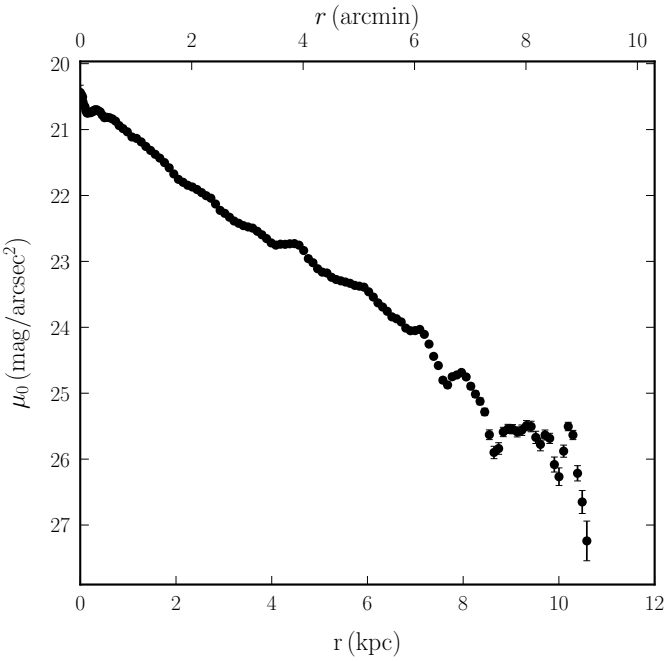

Figure 4.15: W1 (3.4 μm) surface brightness profile of IC 2574.

for which the DM density rapidly increases towards the centre of the halo. The implication of a constant DM density like in the case of the pseudo-isothermal profile is that it results in a rotation curve that increases linearly with the radius, while the NFW profile gives rise to a square-root-like curve. Given the solid body-type rotation of IC 2574, we opt to use the pseudo-isothermal model to describe the galaxy's DM halo. The mass density and velocity distributions of the pseudo-isothermal sphere as a function of the radius r of the sphere are respectively given by

$$\rho_{\rm iso}(r) = \frac{\rho_0}{1+(r/r_{\rm c})^2}, \tag{4.3}$$

$$v_{\rm iso}(r) = \sqrt{4\pi G\rho_0 r_{\rm c}^2\left[1-(r/r_{\rm c})\arctan\left(r/r_{\rm c}\right)\right]} \tag{4.4}$$

where ρ_0 and $r_{\rm c}$ are respectively the central density and the core radius of the halo.

The decomposition of IC 2574's rotation curve was done using the GIPSY's program ROTMAS. The weight affected to a given data point of the rotation curve is equal to the squared inverse of the error bar at that point.

When the stellar M/L is let as a free parameter (best fit model), the least-square fitting of the pseudo-isothermal model to the rotation curve returns a M/L value of $\Upsilon_\star = 0.20\pm0.10\ M_\odot/L_\odot$, with a halo core radius and central density of $r_{\rm C} = 5.8\pm0.6$ kpc and $\rho = (6.7\pm1.0)\times10^{-3}\,{\rm M}_\odot\,{\rm pc}^{-3}$, respectively (see Table 4.2). The obtained

value of the M/L ratio is about 3 times lower than that inferred from the *WISE* colour of the galaxy, but is in agreement with the values obtained in Martinsson et al. (2013) and Lelli et al. (2016). In fact, by measuring the vertical velocity dispersion of disc stars in a sample of 30 spiral galaxies, the authors determined a 3.6μm stellar M/L ratio of about 0.2 $M_{\odot}/L_{\odot}$. At the last measured point (18.4 kpc), the dark component is 10.7 times more massive than the luminous (stars & gas) component. In other words, the dark halo constitutes over 91% of the total dynamical mass of IC 2574, meaning that the stellar and HI discs of the galaxy contribute very little to its total mass. This result is consistent with the study by Martimbeau et al. (1994), who found a dark to luminous mass ratio of 8.9 at their (distance-corrected) last radius of 10.8 kpc, and such large contribution of the dark halo was found in other low mass systems (e.g., DDO 154: Carignan & Freeman 1988, Carignan & Beaulieu 1989; NGC 3109: Jobin & Carignan 1990, Carignan et al. 2013).

To check the effect of the extension of the galaxy's rotation curve on the DM halo model, we have run the fit on the THINGS-only rotation curve; the halo parameters obtained from the fit were sensibly similar to those obtained with the extended curve, showing that the combination has little effect in constraining the model. Because this could be due to the large error bars of the low-resolution DRAO curve, we have used a uniform weighting scheme for the least-square fitting but obtained a similar result. We performed an additional analysis by combining the DRAO curve to the Oh et al. (2008)'s IWM rotation curve of the galaxy instead of the bulk rotation curve (see Fig. 4.9). The rising part of the IWM rotation curve is slightly shallower than the bulk curve, and has a solid body type of rotation at almost all radii. Because of this shape, the best fit model with the pseudo-isothermal profile fails to constrain the parameters of the DM halo, yielding a large core radius of 24.4 ± 4.5 kpc with a stellar M/L ratio of 0.23 ± 0.02 $M_{\odot}/L_{\odot}$. Moreover, when the M/L ratio is fixed to the *WISE* inferred value, the core radius considerably increases to 4.9×10^7 kpc, which is unphysical. It is worth noting that the NFW model also fails to constrain the DM halo. When combined to the DRAO curve following the prescription in Section 4.4.4, the curve becomes slightly flat in the outer regions, allowing to constrain the DM halo with the pseudo-isothermal model. The best model fit provides a core radius of 9.7 ± 1.0 kpc with a M/L ratio of 0.13 ± 0.06 $M_{\odot}/L_{\odot}$, while the fixed M/L method provides a core radius of 16.6 ± 3.4 $M_{\odot}/L_{\odot}$. Again, we note that the *WISE* inferred M/L value overestimates the baryonic contribution to the total mass of the galaxy.

We then fixed the stellar M/L ratio to the *WISE* colour value, and fitted once again the pseudo-isothermal model to the rotation curve. As Table 4.2 shows, the values obtained for the halo parameters do not significantly vary, although a com-

parison of the reduced χ^2 values suggests that the fixed M/L fit is less accurate than the best fit model.

For completeness, we have also used the cusp-like Navarro-Frenk-White (NFW; Navarro et al. 1996b; 1997) density distribution to decompose the rotation curve of the galaxy. Similarly to Oh et al. (2008) and de Blok et al. (2008), we have obtained a zero, therefore unphysical, value for the stellar M/L. The same result was obtained by previous authors for similar galaxies (e.g., NGC 5585, Côté et al. 1991; NGC 3109, Carignan et al. 2013) and for a significant sample of galaxies (Haghi et al. 2018). This implies that the DM halo of the galaxy presents no cusp, and the pseudo-isothermal model should be preferred to the NFW model for the description of the galaxy's DM halo. To investigate whether the inclusion of stellar feedback in the NFW model can produce an acceptable fit to the rotation curve of the galaxy, we have used the criteria of Di Cintio et al. (2014). The authors found a dependence of the inner slope of the dark matter density profile, α, on the stellar-to-halo mass ratio ($M_\star/M_{halo}$). More specifically, for a galaxy like IC 2574, whose $M_\star/M_{halo}$ value is less than ∼0.01 percent (Table 4.2 suggests a ratio of 0.001 percent), the energy from stellar feedback is insufficient to significantly alter the inner dark matter density, and therefore the galaxy retains a cuspy profile. Also, even for galaxies where stellar feedback is sufficient to produce cores in the centre of the halo, the core radius found are only a few kpc in size, definitely lower than the values obtained here. Based on these criteria, we conclude that the NFW profile is not suited to describe the DM profile of IC 2574.

In Fig. 4.16 we show the different decompositions of the hybrid rotation curve with the pseudo-isothermal model.

4.5 Summary

In this work we have used sensitive DRAO observations of IC 2574 and HIJASS J1021+68 to map both the low and high column density gas in the region. The high sensitivity HI intensity map of IC 2574 revealed a substantially large amount of HI around the galaxy, in the form of an HI envelope and in two large concentrations in the regions south and west of the galaxy. The analysis of the HI in the envelope shows that the detected gas is real and distinct from the Galactic HI. Also, the velocity distribution of the HI in the envelope and in the clumps suggests that the low column density gas rotates with the galaxy, but lags behind at the low velocity end of IC 2574. This lag of the gas in the envelope is consistent with a primordial origin for the HI.

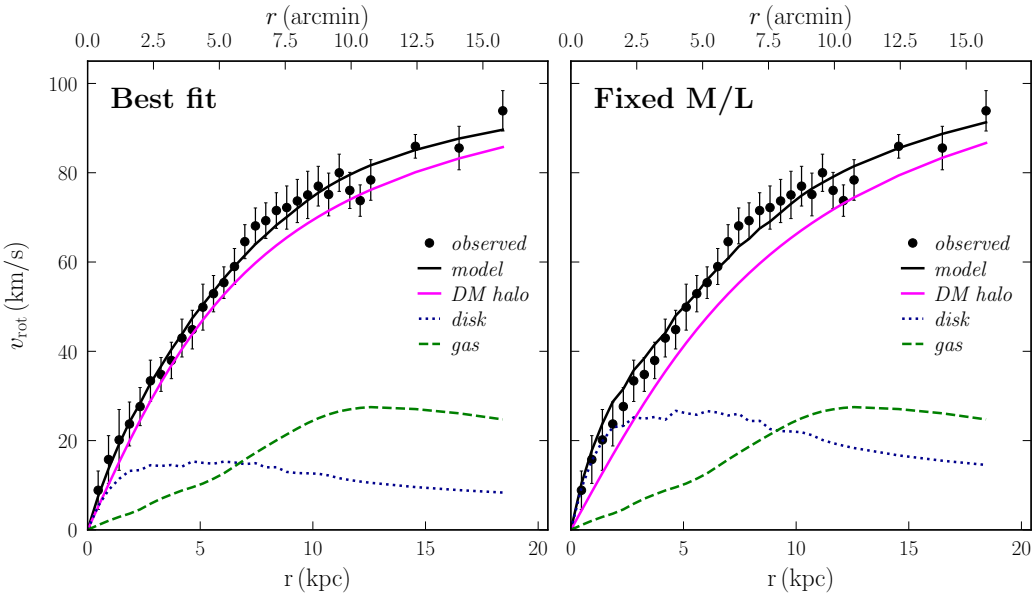

Figure 4.16: Mass models of IC 2574 for the best fit (*left panel*) and fixed M/L (*right panel*) models of the pseudo-isothermal DM halo profile.

Parameter	Best fit	Fixed M/L
THINGS bulk + DRAO		
$\Upsilon_\star$ $(M_\odot/L_\odot)$	0.20 ± 0.14	0.62
$r_{\rm c}$ (kpc)	5.79 ± 0.65	7.60 ± 0.62
ρ_0 $(10^{-3}\,M_\odot\,{\rm pc}^{-3})$	6.71 ± 1.00	4.66 ± 0.37
$\chi^2_{\rm red}$	0.42	0.57
At the last radius ($r = 18.43$ kpc):		
$M_{\rm dark}/M_{\rm lum}$	10.7	9.1
THINGS IWM + DRAO		
$\Upsilon_\star$ $(M_\odot/L_\odot)$	0.13 ± 0.06	0.62
$r_{\rm c}$ (kpc)	9.71 ± 0.95	16.64 ± 3.43
ρ_0 $(10^{-3}\,M_\odot\,{\rm pc}^{-3})$	3.29 ± 0.29	2.11 ± 0.20
$\chi^2_{\rm red}$	0.31	0.99
At the last radius ($r = 18.43$ kpc):		
$M_{\rm dark}/M_{\rm lum}$	11.1	9.4
$M_{\rm total}$ $(M_\odot)$	3.6×10^{10}	

Table 4.2: Results of IC 2574's mass models.

Using a 3D tilted-ring model, we derived the rotation curve of the galaxy to a larger extent than previous works. Taking advantage of higher resolution curves available in the literature, we have constructed a hybrid rotation curve by combining our extended curve to that derived from the THINGS bulk velocity field in Oh et al. (2008). This provided an extended and high resolution rotation curve with a slightly flat part in the outskirts, which can be used to constrain the DM halo parameters. We have then used the pseudo-isothermal model to decompose the resulting rotation curve, and obtained a stellar M/L ratio of 0.2 ± 0.1 $M_{\odot}/L_{\odot}$. This is consistent with the morphological type of the galaxy and with studies in the literature (e.g., Lelli et al. 2016). In order to quantify the effect of the extension on the high resolution curve, we have also decomposed the THINGS bulk rotation curve with the model and obtained similar values for the DM halo parameters. This implies that extension has little effect on the model. However, when combined to the solid body-type of rotation curve derived from the THINGS intensity-weighted mean velocity field, we found that our lower resolution curve allows to constrain the DM halo of the galaxy.

The observations also allowed to resolve the object HIJASS J1021+68 for the first time, and its HI intensity map revealed three major clumps forming the complex. A search for a counterpart in UV, optical R-band and infrared *WISE* W1 was unsuccessful, and the HI kinematics of the system suggests that both rotation and random motions contribute importantly to its gravitational support. Furthermore, the analysis of the PV diagram of the data shows strong evidence of an HI connection between the gas complex and IC 2574, but not between the central and eastern clouds of the complex. This sheds light on the nature of HIJASS J1021+68, and we argue that the object is not a dark galaxy as previously thought, but a complex of HI clouds stripped from, or falling onto the envelope of IC 2574.

Acknowledgments

The authors are very grateful to the staff at DRAO, particularly to Operations Manager Dr. Andrew Gray for his flexibility and assistance in observing the many fields and gathering archived data for our work. The work of CC is based upon research supported by the South African Research Chairs Initiative (SARChI) of the Department of Science and Technology (DST), the South African Radio Astronomy Observatory (SARAO) and the National Research Foundation of South Africa (NRF). The research of AS has been supported by SARChI and SARAO fellowships. The research of LC is supported by the Comité Mixto ESO-Chile and the DGI at University of Antofagasta.

Chapter 5

Conclusion

5.1 Summary of observational results

In this thesis we have presented deep HI observations of various nearby galaxies, allowing us not only to probe the distribution of the low column density gas in and around these galaxies, but also to obtain a detailed picture of their HI kinematics.

Starting with a sample of twenty galaxies selected from the MHONGOOSE survey (de Blok et al. 2018b), we have used the KAT-7, GBT and MeerKAT AR1 telescopes to investigate the HI distribution and kinematics in nearby galaxies down to low column density levels. With the KAT-7 observations of five of the twenty galaxies, we have selected different flux and phase calibrators to investigate the effects of the calibrator choice on the final data products. This allowed us to identify the best flux and phase calibrators for these galaxies. We found that the calibrations applied to the KAT-7 observations proved to improve the quality of the data after a self-calibration of the calibrators was performed. Using the GBT observations of sixteen galaxies, we searched for gas clouds around the galaxies that might hint at ongoing gas accretion taking place in the candidates. Despite the high column density sensitivity of the observations, we did not detect any such structure with a reasonable level of confidence above a 3σ detection level of $\sim 2.2 \times 10^{18}\,\mathrm{cm}^{-2}$, at an average physical resolution of 30 kpc and for a 20 km s^{-1} linewidth. However, noting that the low column density clouds are generally found in small discrete clouds, we admit that there is a possibility that we may have missed them if they reside in the probed regions in sizes smaller than the GBT beam. This confirms that resolution is an important factor in detecting low column density emission just like sensitivity, as was shown for the intergalactic HI between M31 and M33 (Wolfe et al. 2013) and for some HALOGAS galaxies (Pingel et al. 2018).

Next, we have brought our attention to two nearby galaxies: NGC 7424 taken from the MHONGOOSE sample and observed with the KAT-7, and NGC 3621 observed with the MeerKAT AR1 as part of the telescope commissioning. The kinematical analysis of the former galaxy allowed to construct its mass models by decomposing its rotation curve with three different models: the pseudo-isothermal (ISO), the Navarro-Frenk-White (NFW) and the MOND models. The first two models show that the dynamics of the galaxy is dominated by dark matter at all radii, in agreement with its morphological type. As for MOND, the decomposition of the galaxy's rotation curve with the model provided results that are inconsistent with the observations. For NGC 3621, the MeerKAT AR1 commissioning observations of the galaxy allowed to extend its rotation curve twice as far as in previous works in the literature (e.g., THINGS; de Blok et al. 2008). We found that the galaxy is asymmetric in HI, and presents a warp parallel to the line of sight. The mass models of the galaxy reveal a maximum stellar disc in its inner regions, and show that the pseudo-isothermal model provides the best agreement with the observations, consistent with NGC 7424's mass models.

In the second part of the thesis, we have used the DRAO telescope to survey at a high column density sensitivity the HI in a $5° \times 5°$ region of the M81 group that includes the M81 complex and the dwarf galaxy IC 2574. This survey is unprecedented, as no other survey had probed before such a large area of the M81 group at such high sensitivity in HI. Aiming to make a full census of the HI in the surveyed area, we have found, similarly to previous observations, that the interacting three major galaxies of the group – M81, M82 and NGC 3077 – are connected through HI bridges and intergalactic HI clouds. One of the major findings of the survey is the reveal of the full extent of the western HI arm connecting the three galaxies to NGC 2976, the fourth galaxy of the group located at a projected distance of 87.3 kpc southwest of M81. Indeed, the previous maps of the interacting system were either not deep enough to map the full extent of (e.g. Yun et al. 1994, de Blok et al. 2018b), or lacked the resolution to resolve the arm (see the GBT map of Chynoweth et al. 2008). The M81 observations presented in this thesis not only show that the arm connects the three interacting galaxies to NGC 2976, but they also offer enough resolution to map the structure of the arm. Our HI map also shows that what was previously thought, from the GBT observations, to be an extended cloud located between the southern region of M81 and NGC 2976, is in fact a complex of small clouds filling the space between the arm and the "main body" of the system.

Accounting for the ordered motion of the HI gas in the M81-M82-NGC3077 sys-

tem, and assuming that all gas and galaxies lie in a common rotating system, we have used the tilted-ring model to derive the rotation curve of the system. The model allowed us to identify the dynamical centre of the system, which is at a projected distance of about 4.7 kpc east of M81, and at systemic velocity of -5 km s^{-1}. The average inclination and position angle of the common plane of the system gas, as obtained from the model, are respectively $62\overset{\circ}{.}0 \pm 9\overset{\circ}{.}1$ and $346\overset{\circ}{.}7 \pm 8\overset{\circ}{.}0$. We observed the rotation curve of the system to be roughly constant over a large range of radii, with a prominent wiggle associated to M82, as if the outermost gas were rotating at the same speed as the gas in the disc of the M81 galaxy. The shape of the large-scale rotation curve could suggest a single dark matter halo for the system. Also, although the velocities of the approaching and receding sides of the system differ, the flat trend corroborates the assumption of a large-scale rotating system dominated by M81. We also noted a non-negligible radial motion in the model, perhaps highlighting the streaming of outer gas and galaxies with respect to M81.

In the last part of the thesis, we have focused on the subset of the M81 observations data covering IC 2574 and previously classified dark galaxy HIJASS J1021+68, and performed a thorough analysis of the distribution and kinematics of the HI in the two systems. Thanks to the high sensitivity reached, we were able to detect a substantially large amount of low column density HI around the galaxy, in the form of an HI envelope and in two large concentrations in the regions south and west of the galaxy. This low density gas was found to rotate with the galaxy but lags behind, especially at the low velocity end of IC 2574. This lag of the gas in the envelope is consistent with a primordial origin for the HI.

We have also used a 3D tilted-ring model to derive the rotation curve of IC 2574 to a larger extent than previous works, and taking advantage of higher resolution curves available in the literature, we have constructed a hybrid rotation curve by combining our extended curve to that derived from the high resolution THINGS data (Oh et al. 2008). This allowed to constrain the galaxy's DM halo parameters with the pseudo-isothermal model, and we obtained a M/L ratio of 0.2 ± 0.1 $M_{\odot}/L_{\odot}$ for its stellar disc, consistent with studies in the literature (e.g., Lelli et al. 2016). The observations also allowed to resolve HIJASS J1021+68 for the first time, and its HI intensity map revealed three major clumps forming the complex. A search for a counterpart in UV, optical R-band and infrared WISE W1 was unsuccessful, and the HI kinematics of the system suggests that both rotation and random motions contribute importantly to its gravitational support. The analysis of HIJASS J1021+68 in light of its connection with IC 2574 allowed us to postulate that the object is not a dark galaxy as previously

thought, but a complex of HI clouds stripped from, or falling onto the envelope of IC 2574.

5.2 General conclusions and future work

The emerging picture of low column density HI coming from the observations presented in this thesis, as well as those reported in recent studies (e.g., Heald et al. 2011, Pingel et al. 2018), is that extended low column density HI emission does not seem to systemically exist around late type galaxies. The lack of HI complexes around the 20 isolated, carefully selected galaxies of the MHONGOOSE sample indicates that the detection of such faint features, if they exist, necessitates both high sensitivity and spatial resolution. The search conducted in these work was carried to a typical column density limit of $\sim 2.2 \times 10^{18}\,\mathrm{cm}^{-2}$ at an angular scale of $9.1'$ kpc. The MHONGOOSE survey, which is scheduled to begin observing soon with MeerKAT, will probe the HI in these galaxies down to $7.5 \times 10^{18}\,\mathrm{cm}^{-2}$ at an angular scale of $30''$, or to $5.5 \times 10^{17}\,\mathrm{cm}^{-2}$ at a scale of $90''$ (de Blok et al. 2018a). Unlike most existing interferometers, MeerKAT has a large number of short baselines and a wide field of view. This will allow the observations to efficiently detect low column density material in the galaxies, and map, in a single pointing, the HI twice as far out into their halo as the VLA or WSRT can allow. The commissioning data of the Array Release 1 of the telescope (16 antennas) presented in this work has clearly demonstrated its capability of performing sensitive observations. To overcome some of the technical difficulties related to data calibration, the work presented here shows that applying self-calibration to phase calibrator sources before using them to calibrate targets is an efficient way of improving the quality of the data. This is particularly important for the high resolution, large field-of-view MeerKAT telescope for which (i) calibrator sources can be resolved and therefore cannot be approximated as point sources, and (ii) it is likely for secondary sources to appear in the field-of-view of the calibrators. This technique could be applied to future surveys, such as the upcoming MHONGOOSE survey, for further testing and development.

With the advent of the 500 m FAST single dish telescope in China scheduled to start operating in the next few years, the detection limit of faint, large scale HI structures is expected to improve (Carignan 2016; 2019). The combination of the high resolution MeerKAT data with those of FAST will provide more sensitive data at reasonable resolutions (see Sorgho et al. 2017, for an example of combination with KAT-7 and WSRT), that will allow us to obtain a more complete picture of galaxies' low column density HI.

Unlike the twenty individual MHONGOOSE galaxies observed, the intergalactic medium of the M81 group's central region exhibits several low column density HI clouds. In fact, M81 has been the target of several observational campaigns in recent years (e.g., Yun et al. 1994, Chynoweth et al. 2008, de Blok et al. 2018b), each conducted with the aim of improving the existing HI picture of the group. The deep ($\sim 10^{18}\,\mathrm{cm}^{-2}$) and wide ($5^\circ \times 5^\circ$) survey presented here shows that there exists an important quantity of faint extragalactic HI material in the environment of the group that none of the previous observations had been able to detect or resolve. This HI is mainly found in the form of discrete clouds that are not distributed everywhere in the group, but are observed to lie mostly around the HI complex formed by intergalactic bridges and arms connecting the central members, and near the dwarf galaxy IC 2574. The spatial and kinematical association of the clouds with the HI complex suggests that they are most likely being stripped from the HI complex, or are being accreted onto it. Given that all searches for direct signs of gas accretion have been unsuccessful so far, we postulate that if the second hypothesis is true, then there could exist more HI in the medium either at lower column densities or in an ionised form. The mapping of the HI in the group is still being performed, and additional observations are expected to be completed in the near future. This will increase the sensitivity of the survey, allowing to search for fainter structures. Also, to better understand the origin of the detected clouds, it will be necessary to obtain sensitive Hα data in the vicinity to search for Hα counterparts.

Two galaxy members of the group – IC 2574 and NGC 2976 – present extended low column density HI envelopes at low systemic velocities that had not been detected before. The nature of the gas in these envelopes is not clear yet, although it is likely that IC 2574's envelope is a primordial HI envelope out of which the galaxy formed, and the envelope around NGC 2976 formed as a result of interaction with the members of the interacting M81 system. A sensitive telescope like MeerKAT, because of its short baselines, could help us to unveil the kinematical structure of these envelopes and better understand their origin.

Lastly, the decompositions of the rotation curves obtained for the studied galaxies (for which we had enough angular resolution to analyse their kinematics) show that the observationally-motivated pseudo-isothermal profile describes better their Dark Matter halo than the NFW profile suggested by the CDM model for low-mass galaxies, while both profiles fit equally well the rotation curves of massive spirals. This conclusion is in agreement with the results from the high-resolution THINGS survey (de Blok et al. 2008, Oh et al. 2008) which mostly focused on detailing the kinematics of galaxies' inner regions. Kinematical studies of larger samples conducted with

MeerKAT and eventually the SKA 1 will help to better constrain the Dark Matter halos of galaxies by tracing, at high resolutions, their rotation to much larger radii from their centre.

Appendix A

HI maps of the GBT detections

Below we present the GBT HI maps and global spectra of the 16 MHONGOOSE galaxies, as well as the secondary sources listed in Table 2.4. Figs. A.1 to A.16 show the column density map on the left panel and the global spectrum on the right. The HI column density levels are $0.5\,(3\sigma), 1.0, 2.0, 4.0, ..., \times 10^{19}\,\mathrm{cm}^{-2}$, overlaid on infrared *WISE* W1 grayscale images. The galaxies marked with an asterisk were not bright enough in the W1 band, and their grayscale images were obtained from NED[†] in the optical Johnson B_J band. Fig. A.17 shows two secondary sources that were located in the field of view of some of the targets. The global profiles of the four secondary sources are given in Fig. A.18. For each profile, the systemic velocity is marked by a vertical upward arrow.

[†] http://ned.ipac.caltech.edu/

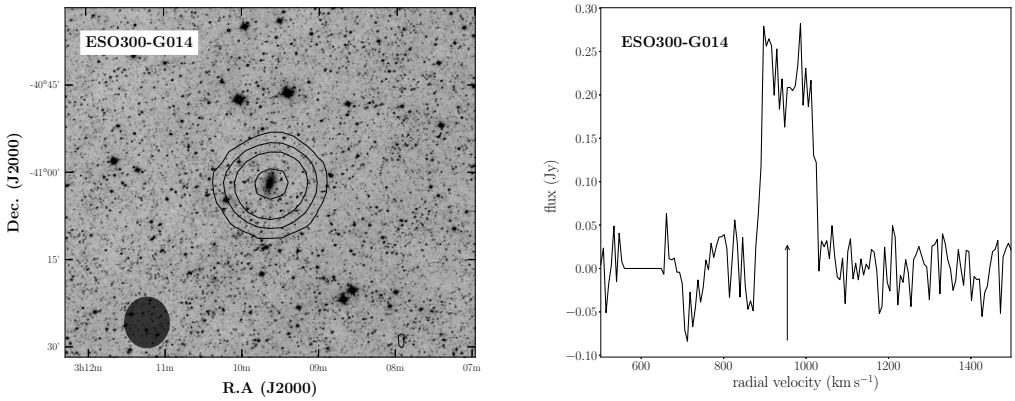

Figure A.1: ESO 300-G014.

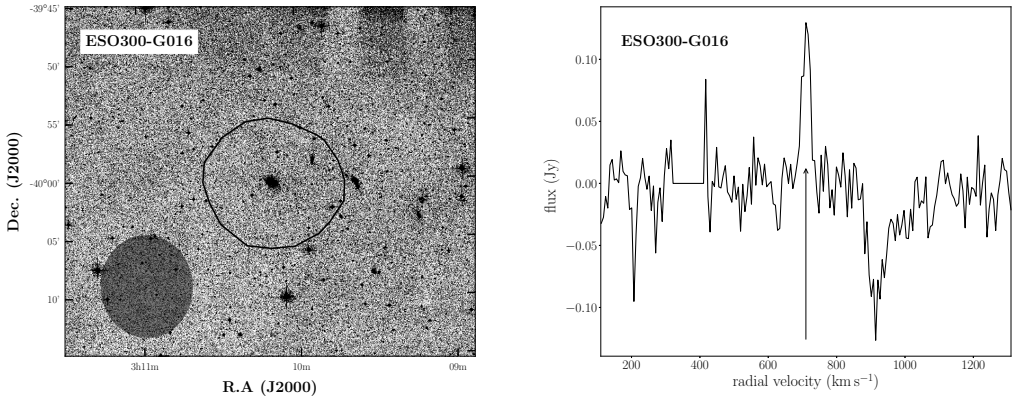

Figure A.2: ESO 300-G016*.

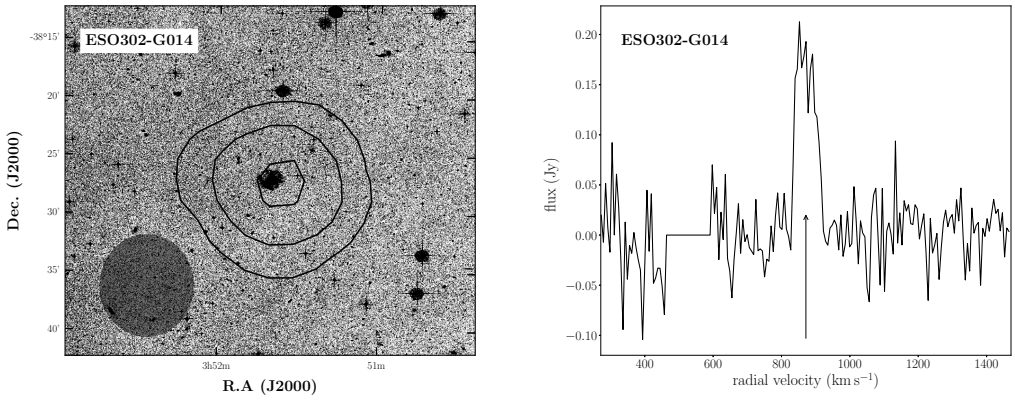

Figure A.3: ESO 302-G014*.

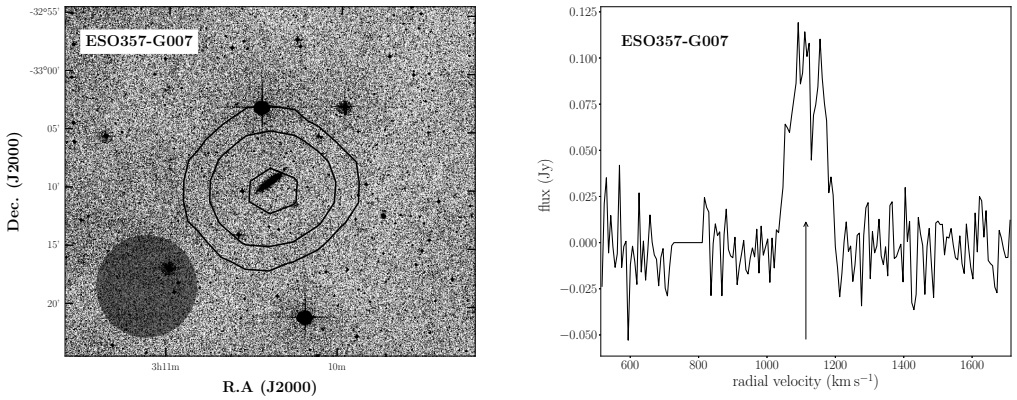

Figure A.4: ESO 357-G007*.

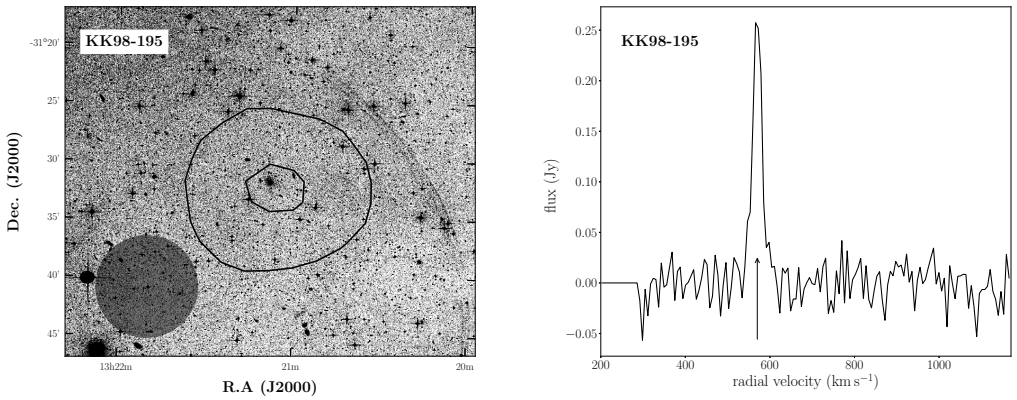

Figure A.5: KK 98-195*.

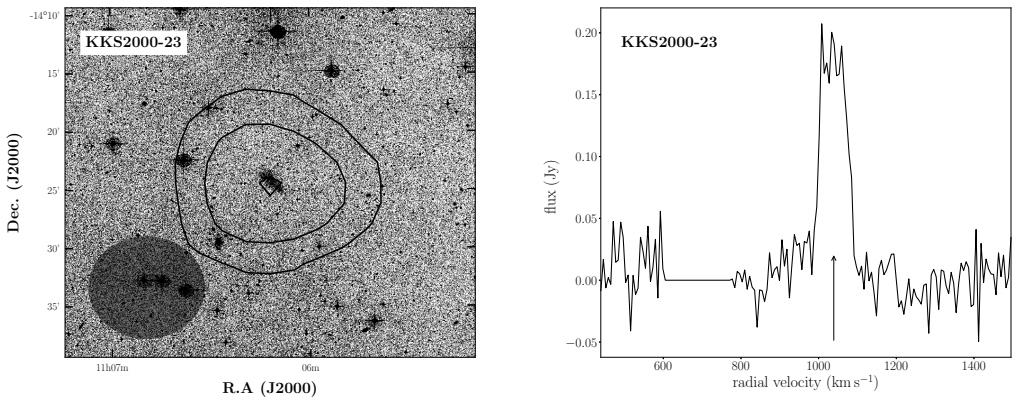

Figure A.6: KKS 2000-23*.

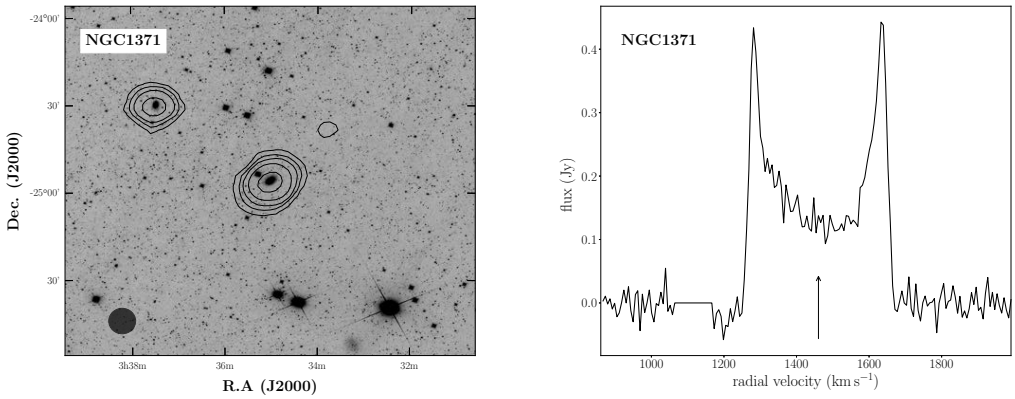

Figure A.7: NGC 1371 (*centre*) and secondary source NGC 1385 (*upper left contours*). The profile of NGC 1385 is given in Fig. A.18.

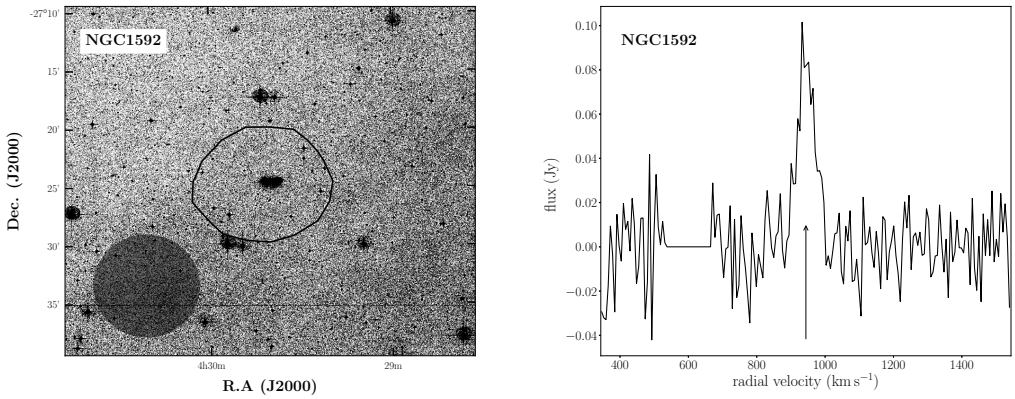

Figure A.8: NGC 1592*.

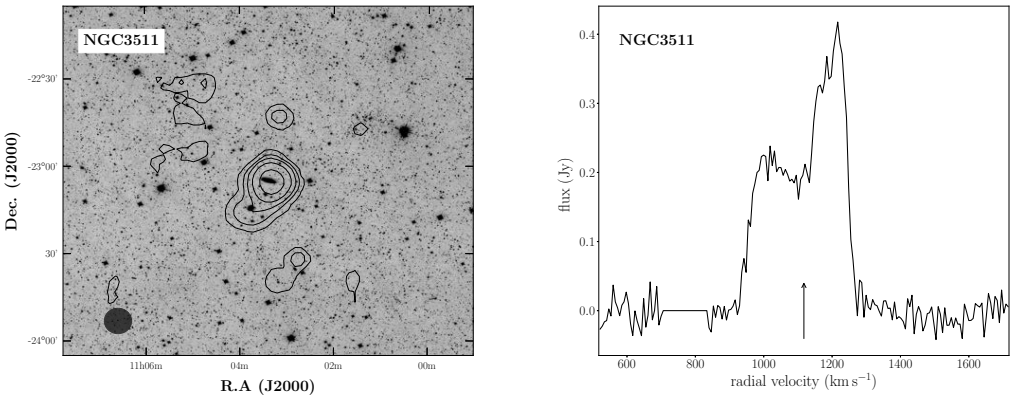

Figure A.9: The GBT-confused sources NGC 3511 (*centre*) and NC 3513 (*lower left*). The contours in the outskirts do not have reported optical counterparts, and their structures, plus their low detection levels, suggest that further investigation is needed to confirm whether they correspond to real detections.

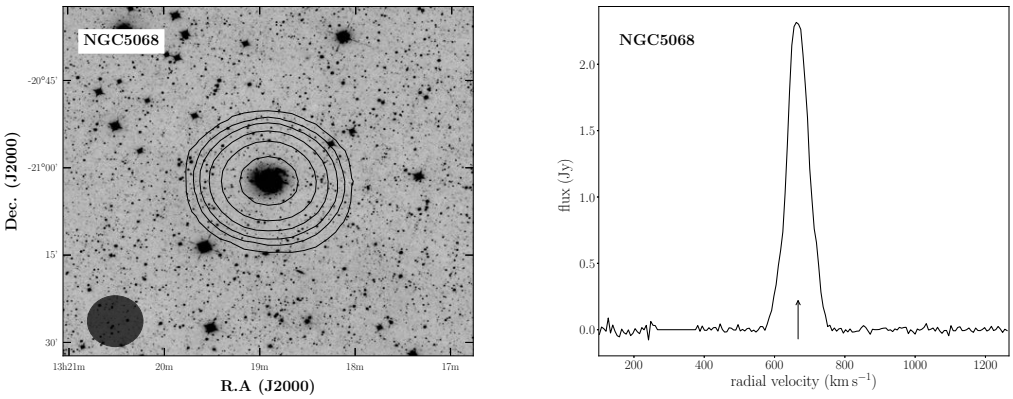

Figure A.10: NGC 5068.

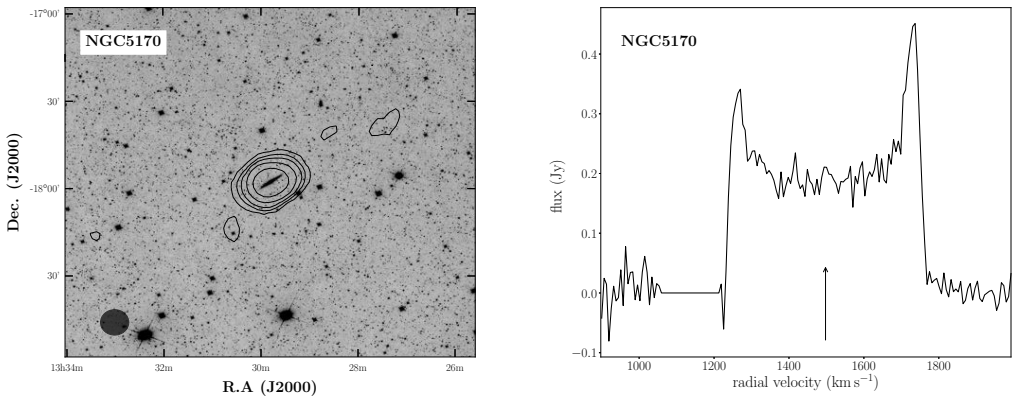

Figure A.11: NGC 5170. The true nature of the structures around the galaxy is not known, and further investigation is needed to determine whether they are real detections.

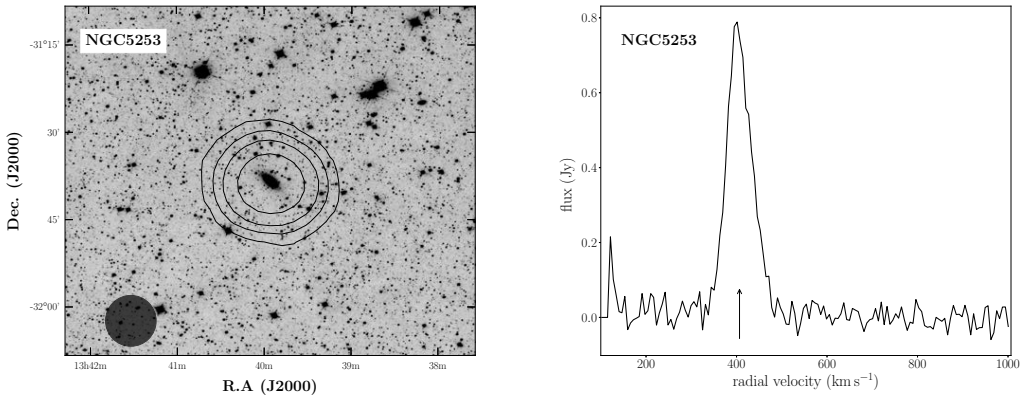

Figure A.12: NGC 5253.

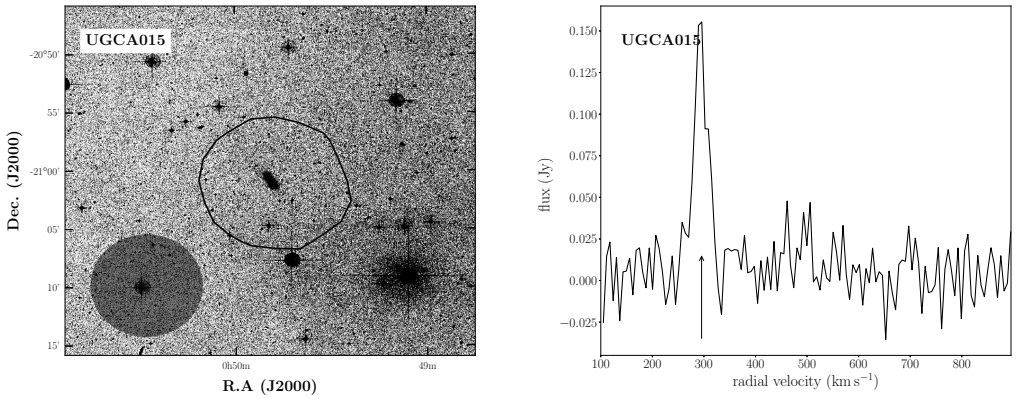

Figure A.13: UGCA 015*.

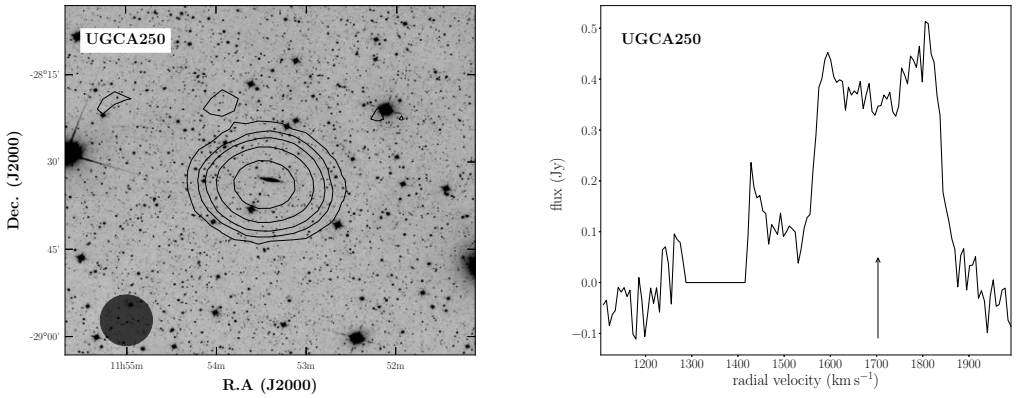

Figure A.14: UGCA 250. The true nature of the structures northeast of the galaxy is not known, and further investigation is needed to determine whether they are real detections.

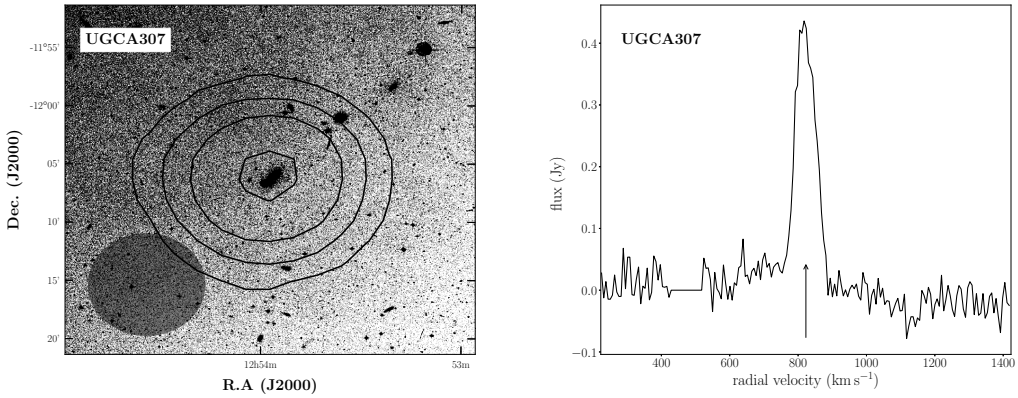

Figure A.15: UGCA 307*.

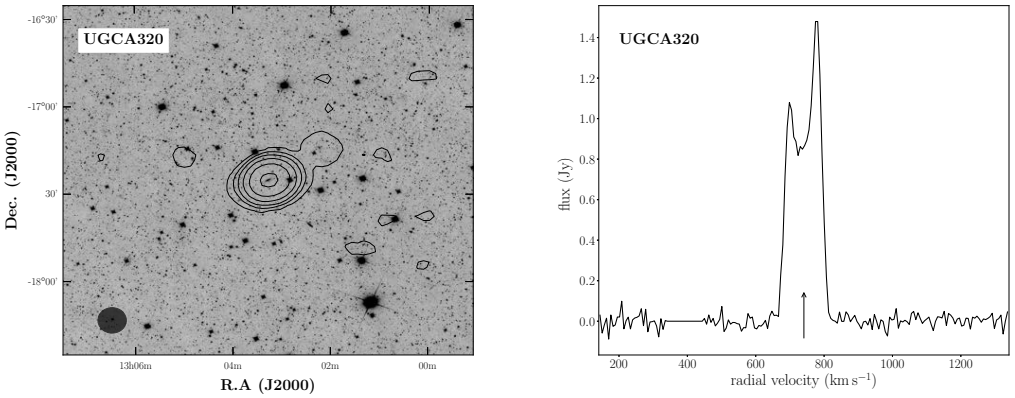

Figure A.16: The central contours represent the position of UGCA 320, while the adjacent contour on the upper right side shows the galaxy UGCA 319. The HI profile of UGCA 319 is shown in Fig. A.18. The true nature of the structures around the galaxies pair is not known, and further investigation is needed to determine whether they are real detections.

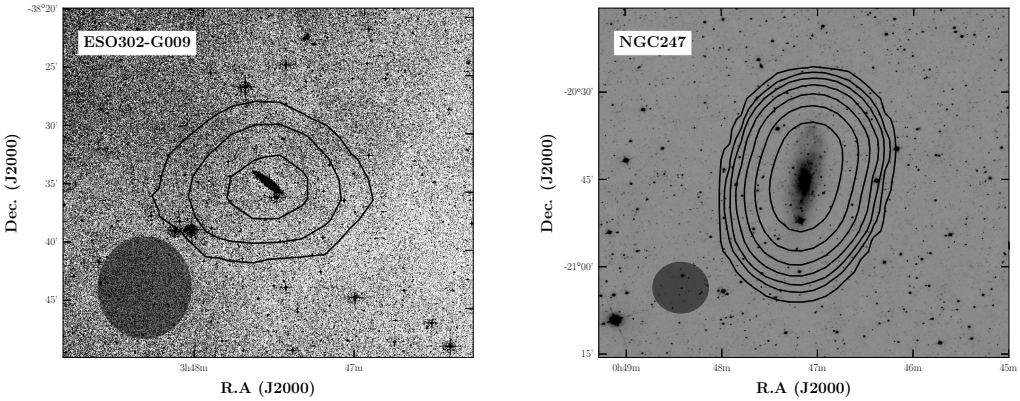

Figure A.17: The secondary galaxies ESO 302-G009 located west of ESO 302-G014 (*left*, overlaid on an optical IIIaJ image) and NGC 247 located west of UGCA 015 (*right*, overlaid on a *WISE* W1 image). Their HI profiles are given in Fig. A.18.

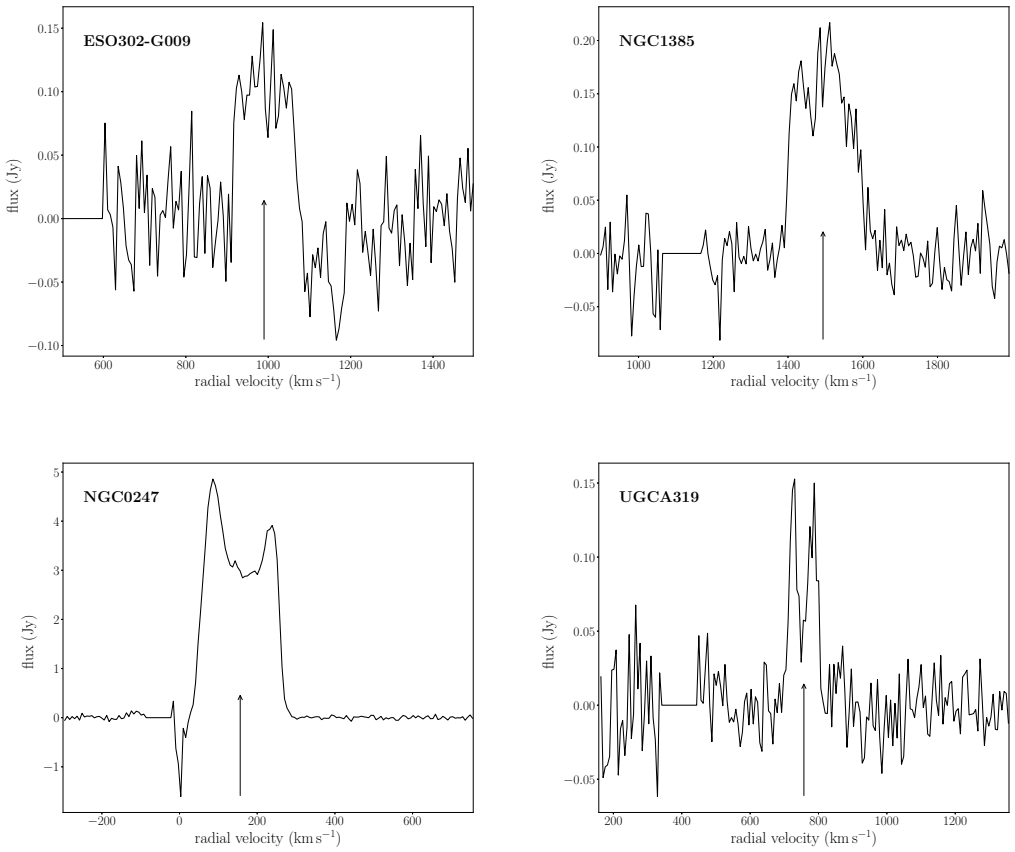

Figure A.18: The global HI profiles of the secondary sources ESO 302-G009 (*upper left*), NGC 1385 (*upper right*), NGC 247 (*lower left*) and UGCA 319 (*lower right*).

Appendix B

HI map of HIJASS J1021+68 clouds

The different clouds of HIJASS J1021+68 are delimited by boxes in Fig. B.1.

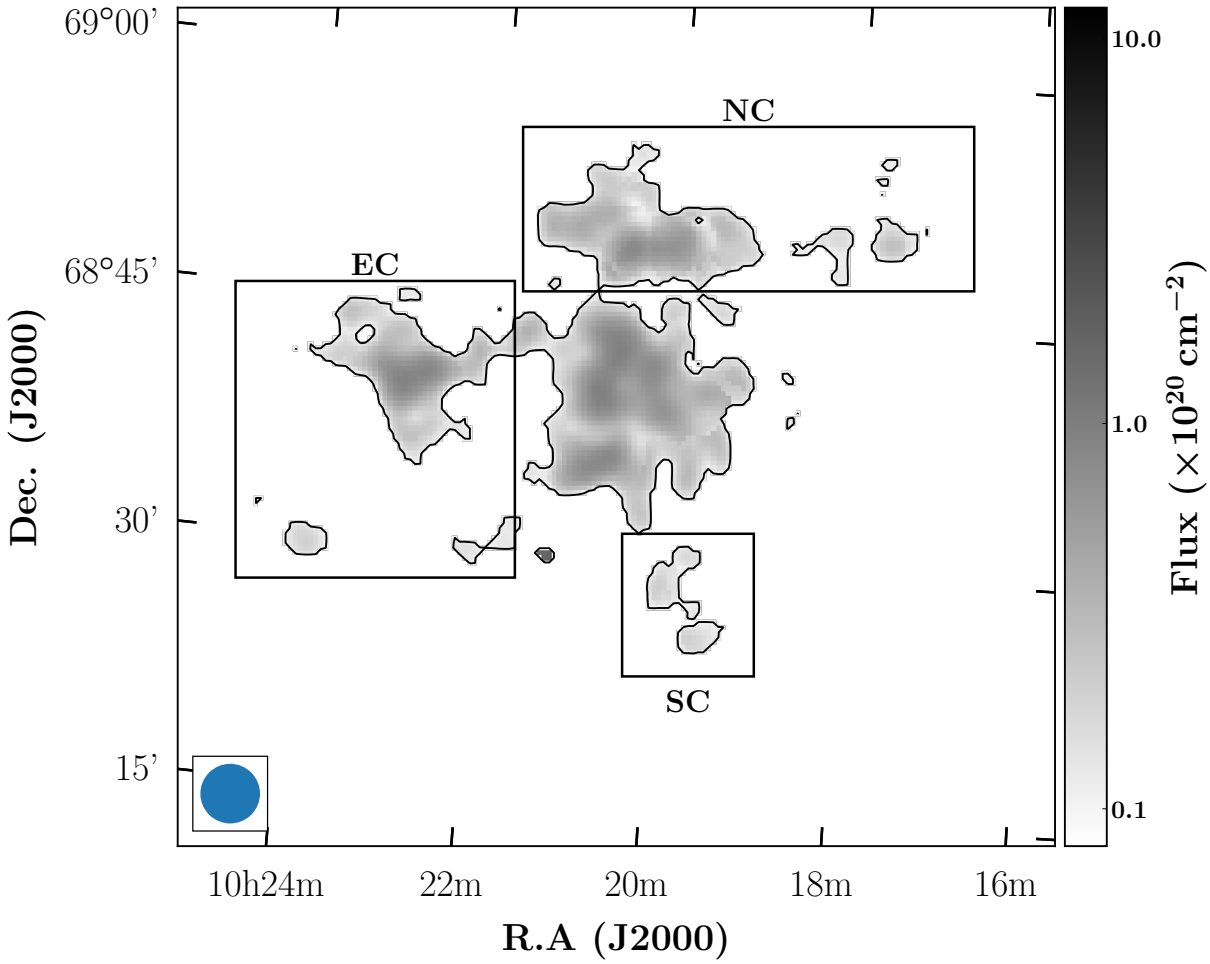

Figure B.1: The different clouds of HIJASS J1021+68.

Appendix C

HI velocity field and velocity dispersion of IC 2574.

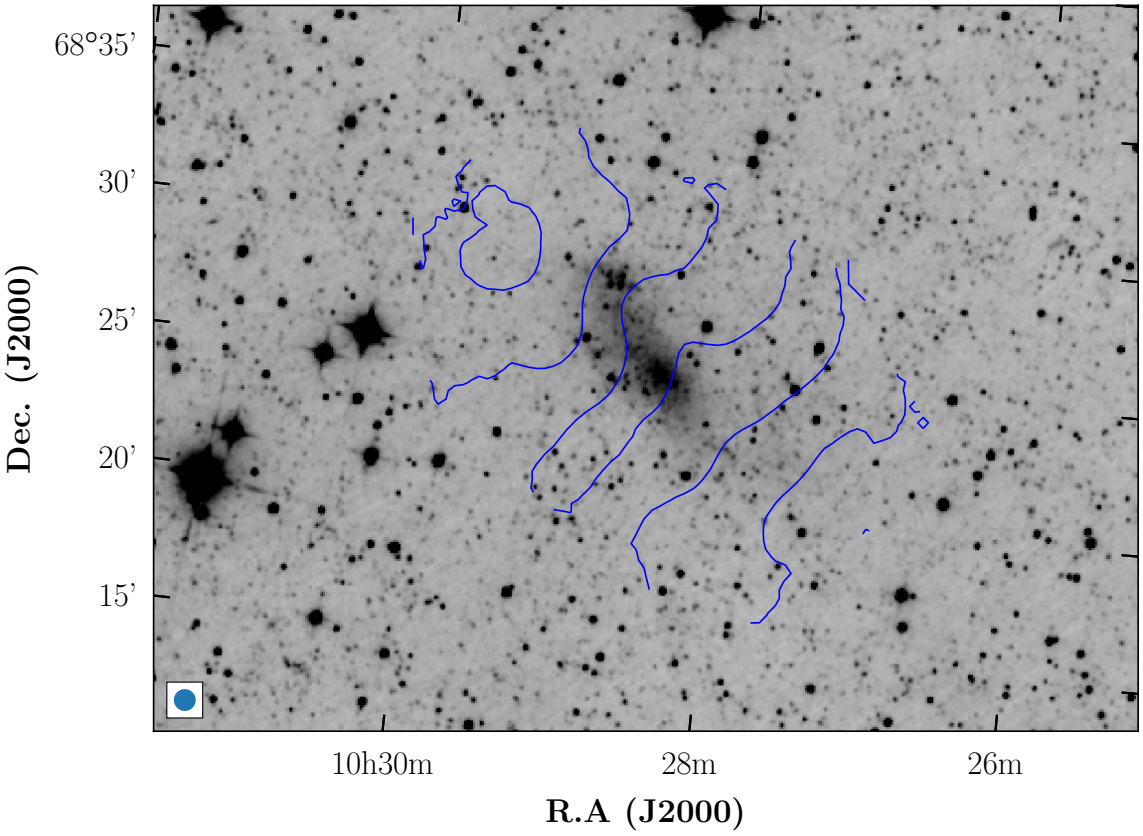

Figure C.1: The velocity field of IC 2574 overlaid on a *WISE* W1 image. Contours go from 0 (southwest) to 100 km s^{-1} (northeast) in 20 km s^{-1} increment.

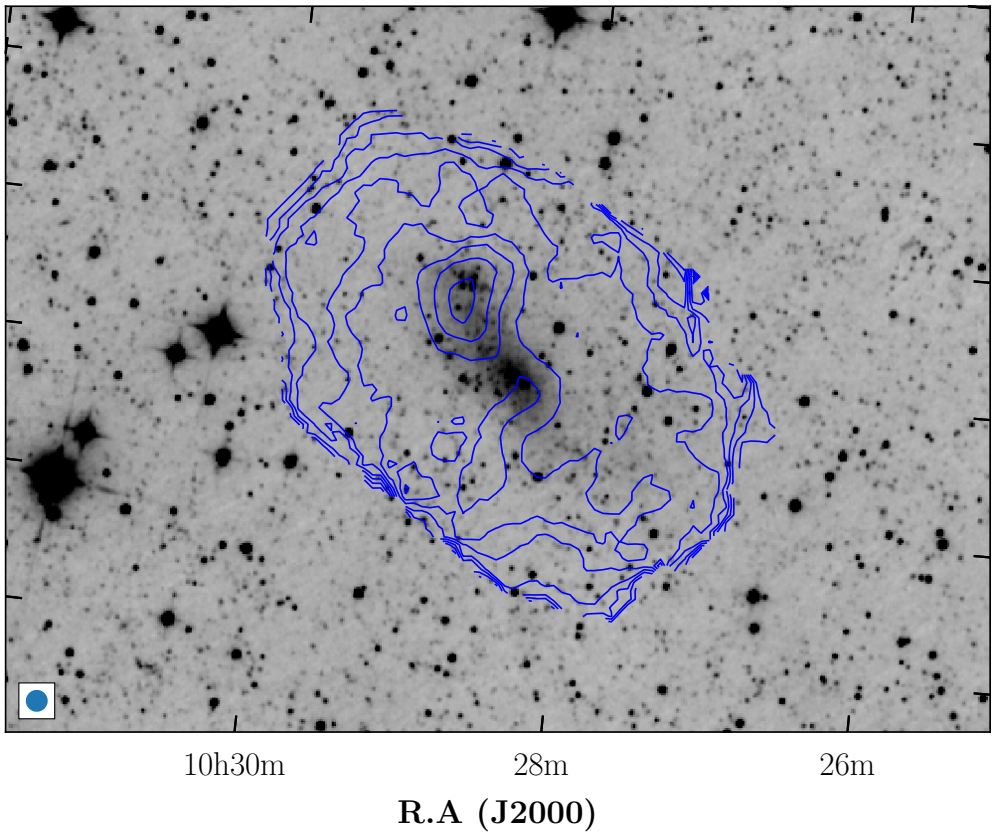

Figure C.2: The velocity dispersion of IC 2574 overlaid on a *WISE* W1 image. Contours are $0, 2, 4, ..., 18$ km s^{-1}.

Bibliography

Allen R. J., Goss W. M., van Woerden H., 1973, A&A, 29, 447

Alpaslan M., et al., 2014, MNRAS, 440, L106

Appleton P. N., Davies R. D., Stephenson R. J., 1981, MNRAS, 195, 327

Argyle E., 1965, ApJ, 141, 750

Babcock H. W., 1939, Lick Obs. Bull., 19, 41

Baldry I. K., 2008, A&G, 49, 5.25

Baldwin J. E., Field C., Warner P. J., Wright M. C. H., 1971, MNRAS, 154, 445

Barnes D. G., et al., 2001, MNRAS, 322, 486

Begeman K. G., 1989, A&A, 223, 47

Begeman K. G., Broeils A. H., Sanders R. H., 1991, MNRAS, 249, 523

Begum A., Chengalur J. N., Karachentsev I. D., Sharina M. E., Kaisin S. S., 2008, MNRAS, 386, 1667

Bell E. F., McIntosh D. H., Katz N., Weinberg M. D., 2003, ApJS, 149, 289

Binney J., Tremaine S., 2008, Galactic dynamics: Second Edition. Princeton University Press, http://adsabs.harvard.edu/abs/2008gady.book.....B

Blitz L., Spergel D. N., Teuben P. J., Hartmann D., Burton W. B., 1999, ApJ, 514, 818

Blumenthal G. R., Faber S. M., Primack J. R., Rees M. J., 1984, Nature, 311, 517

Bond J. R., Kofman L., Pogosyan D., 1996, Nature, 380, 603

Börngen F., Karachentseva V. E., 1982, AN, 303, 189

Börngen F., Karachentseva V. E., 1985, AN, 306, 301

Bose S., et al., 2019, MNRAS, 486, 4790

Bosma A., 1978, PhD thesis, Groningen Univ., http://adsabs.harvard.edu/abs/1978PhDT.......195B

Bosma A., 1981a, AJ, 86, 1791

Bosma A., 1981b, AJ, 86, 1825

Bournaud F., Duc P. A., 2006, A&A, 456, 481

Bowen D. V., Chelouche D., Jenkins E. B., Tripp T. M., Pettini M., York D. G., Frye B. L., 2016, ApJ, 826, 50

Bower R. G., Lucey J. R., Ellis R. S., 1992, MNRAS, 254, 601

Boyce P. J., et al., 2001, ApJ, 560, L127

Braun R., Thilker D. A., 2004, A&A, 435, 421

Broeils A. H., Rhee M.-H., 1997, A&A, 324, 877

Brouillet N., Baudry A., Combes F., Kaufman M., Bash F., 1991, A&A, 242, 35

Camilo F., et al., 2018, ApJ, 856, 180

Carignan C., 2016, in Qain L., Li D., eds, ASPC Vol. 502, Frontiers in Radio Astronomy and FAST Early Sciences Symposium 2015. Guiyang, China, p. 55 (arXiv:1510.03462), http://adsabs.harvard.edu/abs/2016ASPC..502...55C

Carignan C., 2019, in Peng B., Carignan C., Zhu M., eds, Proceedings of the FAST-MeerKAT and SKA Pathfinders Synergies meeting. Pingtang, China

Carignan C., Beaulieu S., 1989, ApJ, 347, 760

Carignan C., Freeman K. C., 1985, ApJ, 294, 494

Carignan C., Freeman K. C., 1988, ApJ, 332, L33

Carignan C., Puche D., 1990, AJ, 100, 394

Carignan C., Purton C., 1998, ApJ, 506, 125

Carignan C., Beaulieu S., Freeman K. C., 1990, AJ, 99, 178

Carignan C., Frank B. S., Hess K. M., Lucero D. M., Randriamampandry T. H., Goedhart S., Passmoor S. S., 2013, AJ, 146, 48

Cautun M., van de Weygaert R., Jones B. J. T., Frenk C. S., 2014, MNRAS, 441, 2923

Cayatte V., Balkowski C., van Gorkom J. H., Kotanyi C., 1990, AJ, 100, 604

Cen R., Ostriker J. P., 1999, ApJ, 514, 1

Chambers K. C., et al., 2016, eprint arXiv:1612.05560

Chandar R., Tsvetanov Z., Ford H. C., 2001, AJ, 122, 1342

Chandra P., Ray A., Bhatnagar S., 2002, IAU Circ., 7994

Chemin L., Carignan C., Foster T., 2009, ApJ, 705, 1395

Chemin L., de Blok W. J. G., Mamon G. A., 2011, The Astronomical Journal, 142, 109

Chemin L., Huré J.-M., Soubiran C., Zibetti S., Charlot S., Kawata D., 2016, A&A, 588, A48

Chiboucas K., Karachentsev I. D., Tully R. B., 2009, AJ, 137, 3009

Chiboucas K., Jacobs B. A., Tully R. B., Karachentsev I. D., 2013, AJ, 146, 126

Chung A., van Gorkom J. H., Kenney J. D. P., Vollmer B., 2007, ApJ, 659, L115

Chynoweth K. M., Langston G. I., Yun M. S., Lockman F. J., Rubin K. H. R., Scoles S. A., 2008, AJ, 135, 1983

Chynoweth K. M., Langston G. I., Holley-Bockelmann K., Lockman F. J., 2009, AJ, 138, 287

Chynoweth K. M., Langston G. I., Holley-Bockelmann K., 2011, AJ, 141, 9

Cluver M. E., et al., 2014, ApJ, 782, 90

Colless M., et al., 2001, MNRAS, 328, 1039

Colless M., et al., 2003, eprint arXiv:astro-ph/0306581

Cornwell T. J., Golap K., Bhatnagar S., 2008, ISTSP, 2, 647

Côté S., Carignan C., Sancisi R., 1991, AJ, 102, 904

Côté S., Carignan C., Freeman K. C., 2000, AJ, 120, 3027

Cottrell G. A., 1977, MNRAS, 178, 577

Dalcanton J. J., Stilp A., 2010, ApJ, 721, 547

Davé R., et al., 2001, ApJ, 552, 473

Davidge T. J., 2009, ApJ, 697, 1439

Dekel A., Silk J., 1986, ApJ, 303, 39

Di Cintio A., Brook C. B., Macciò A. V., Stinson G. S., Knebe A., Dutton A. A., Wadsley J., 2014, MNRAS, 437, 415

Di Matteo P., Combes F., Melchior A.-L., Semelin B., 2007, A&A, 468, 61

Di Teodoro E., Fraternali F., 2014, A&A, 567, A68

Di Teodoro E., Fraternali F., 2015, MNRAS, 451, 3021

Doyle M. T., et al., 2005, MNRAS, 361, 34

Dressler A., 1980, ApJ, 236, 351

Drinkwater M. J., Gregg M. D., Hilker M., Bekki K., Couch W. J., Ferguson H. C., Jones J. B., Phillipps S., 2003, Nature, 423, 519

Dubinski J., Carlberg R. G., 1991, ApJ, 378, 496

Duc P.-A., Brinks E., Springel V., Pichardo B., Weilbacher P., Mirabel I. F., 2000, AJ, 120, 1238

Duc P.-A., Bournaud F., Masset F., 2004, A&A, 427, 803

Egorov O. V., Lozinskaya T. A., Moiseev A. V., Smirnov-Pinchukov G. V., 2014, MNRAS, 444, 376

Ellingson S. W., 2015, Antennas in Radio Telescope Systems. Springer Singapore, Singapore, doi:10.1007/978-981-4560-75-7_124-1, http://link.springer.com/10.1007/978-981-4560-75-7{_}124-1

Ewen H. I., Purcell E. M., 1951, Nature, 168, 356

Ferguson H. C., Binggeli B., 1994, A&ARv, 6, 67

Flewelling H. A., et al., 2016, eprint arXiv:1612.05243

Flores R. A., Primack J. R., 1994, ApJ, 427, L1

Freedman W. L., et al., 2001, ApJ, 553, 47

Frenk C. S., White S. D. M., Davis M., Efstathiou G., 1988, ApJ, 327, 507

Fukugita M., Peebles P. J. E., 2004, ApJ, 616, 643

Fukugita M., Hogan C. J., Peebles P. J. E., 1998, ApJ, 503, 518

Gendre M. A., Fenech D. M., Beswick R. J., Muxlow T. W. B., Argo M. K., 2013, MNRAS, 431, 1107

Gentile G., Baes M., Famaey B., Van Acoleyen K., 2010, MNRAS, 406, 2493

Gentile G., et al., 2013, A&A, 554, A125

Goobar A., et al., 2014, ApJ, 784, L12

Greisen E. W., 2003, in , Vol. 285, Information Handling in Astronomy - Historical Vistas. Springer Netherlands, Dordrecht, pp 109–125, doi:10.1007/0-306-48080-8_7

Gunn J. E., Gott J. R. I., 1972, ApJ, 176, 1

Haghi H., Khodadadi A., Ghari A., Zonoozi A. H., Kroupa P., 2018, MNRAS, 477, 4187

Haynes M. P., Giovanelli R., Roberts M. S., 1979, ApJ, 229, 83

Haynes M. P., Giovanelli R., Chincarini G. L., 1984, ARA&A, 22, 445

Heald G., 2015, IAUS, 309, 69

Heald G., et al., 2011, A&A, 526, A118

Heald G., et al., 2016, MNRAS, 462, 1238

Heckman T. M., Dahlem M., Lehnert M. D., Fabbiano G., Gilmore D., Waller W. H., 1995, ApJ, 448, 98

Hernquist L., 1992, ApJ, 400, 460

Hess K. M., et al., 2018, eprint arXiv:1811.12405

Hibbard J. E., van Gorkom J. H., 1996, AJ, 111, 655

Holwerda B. W., Blyth S.-L., 2010, in ISKAF2010 Science Meeting. (arXiv:1007.4101), http://adsabs.harvard.edu/abs/2010iska.meetE..68Hhttps://pos.sissa.it/cgi-bin/reader/conf.cgi?confid=112

Hopkins P. F., Hernquist L., Cox T. J., Di Matteo T., Robertson B., Springel V., 2006, ApJS, 163, 1

Hubble E. P., 1936, Realm of the Nebulae, by E.P.˜Hubble.˜ New Haven: Yale University Press, 1936.˜ ISBN 9780300025002. Yale University Press, http://adsabs.harvard.edu/abs/1936rene.book.....H

Hubble E., Humason M. L., 1931, ApJ, 74, 43

Huchra J., et al., 2005, ASPC, 329

Huchtmeier W. K., Bohnenstengel H.-D., 1981, A&A, 100, 72

Huchtmeier W. K., Witzel A., 1979, A&A, 74, 138

Hunter D. A., et al., 2012, AJ, 144, 134

Jacobs B. A., Rizzi L., Tully R. B., Shaya E. J., Makarov D. I., Makarova L., 2009, AJ, 138, 332

Jarrett T. H., et al., 2012, AJ, 144, 68

Jarvis M. J., et al., 2017, in Proceedings of MeerKAT Science: On the Pathway to the SKA – PoS(MeerKAT2016). (arXiv:1709.01901), http://adsabs.harvard.edu/abs/2016mks..confE...6J

Jobin M., Carignan C., 1990, AJ, 100, 648

Kalnajs A., 1983, in Athanassoula E., ed., IAUS Vol. 100, Internal Kinematics and Dynamics of Galaxies. Dordrecht, D. Reidel Publishing Co., Besancon, France, pp 87–88, http://adsabs.harvard.edu/abs/1983IAUS..100...87K

Karachentsev I. D., et al., 2000, A&A, 363, 117

Karachentsev I. D., et al., 2002a, A&A, 383, 125

Karachentsev I. D., Mitronova S. N., Karachentseva V. E., Kudrya Y. N., Jarrett T. H., 2002b, A&A, 396, 431

Karachentsev I. D., Karachentseva V. E., Huchtmeier W. K., Makarov D. I., 2004, AJ, 127, 2031

Karachentseva V. E., Karachentsev I. D., Shcherbanovsky A. L., 1979, AISAO, 11, 3

Kauffmann G., Li C., Heckman T. M., 2010, MNRAS, 409, 491

Kaviraj S., et al., 2007, ApJS, 173, 619

Kenney J. D. P., van Gorkom J. H., Vollmer B., 2004, AJ, 127, 3361

Kenney J. D. P., Geha M., Jáchym P., Crowl H. H., Dague W., Chung A., van Gorkom J., Vollmer B., 2014, ApJ, 780, 119

Kent S. M., 1986, AJ, 91, 1301

Kereš D., Katz N., Weinberg D. H., Davé R., 2005, MNRAS, 363, 2

Klypin A. A., Shandarin S. F., 1983, MNRAS, 204, 891

Klypin A. A., Kravtsov A. V., Valenzuela O., Prada F., 1999, ApJ, 522, 82

Kobulnicky H. A., Skillman E. D., 2008, AJ, 135, 527

Koribalski B., Dahlem M., Mebold U., Brinks E., 1993, A&A, 268, 14

Koribalski B. S., et al., 2004, AJ, 128, 16

Koribalski B. S., et al., 2018, MNRAS

Landecker T. L., et al., 2000, A&AS, 145, 509

Lang R. H., et al., 2003, MNRAS, 342, 738

Lee-Waddell K., et al., 2016, MNRAS, 460, 2945

Lehner N., et al., 2013, ApJ, 770, 138

Lehner N., Howk J. C., Wakker B. P., 2017, ApJ, 848, 71

Lelli F., Fraternali F., Sancisi R., 2010, A&A, 516, A11

Lelli F., et al., 2015, A&A, 584, A113

Lelli F., McGaugh S. S., Schombert J. M., 2016, AJ, 152, 157

Lockman F. J., Free N. L., Shields J. C., 2012, AJ, 144, 52

Makarov D., Prugniel P., Terekhova N., Courtois H., Vauglin I., 2014, A&A, 570, A13

Makarova L. N., et al., 2002, A&A, 396, 473

Martimbeau N., Carignan C., Roy J.-R., 1994, AJ, 107, 543

Martin D. C., et al., 2005, ApJ, 619, L1

Martinsson T. P. K., Verheijen M. A. W., Westfall K. B., Bershady M. A., Andersen D. R., Swaters R. A., 2013, A&A, 557, 131

Mashchenko S., Couchman H. M. P., Wadsley J., 2006, Nature, 442, 539

Mashchenko S., Wadsley J., Couchman H. M. P., 2008, Science, 319, 174

Mateo M., 1998, ARA&A, 36, 435

Matsushita S., Kawabe R., Kohno K., Matsumoto H., Tsuru T. G., Vila-Vilaro B., 2005, ApJ, 618, 712

Mattila S., Fraser M., Smartt S. J., Meikle W. P. S., Romero-Canizales C., Crockett R. M., Stephens A., 2013, MNRAS, 431, 2050

Mayall N. U., 1951, Publ. Obs. Mich., 10, 19

Mayya Y. D., Carrasco L., Luna A., 2005, ApJ, 628, L33

McConnachie A. W., 2012, AJ, 144, 4

McKeith C. D., Greve A., Downes D., Prada F., 1995, A&A, 293, 703

Meurer G. R., Carignan C., Beaulieu S., Freeman K. C., 1996, AJ, 111, 1551

Meurer G. R., et al., 2006, ApJS, 165, 307

Meyer M. J., et al., 2004, MNRAS, 350, 1195

Mihos J. C., Hernquist L., 1996, ApJ, 464, 641

Milgrom M., 1983a, ApJ, 270, 365

Milgrom M., 1983b, ApJ, 270, 371

Moore B., 1994, Nature, 370, 629

Moore B., Ghigna S., Governato F., Lake G., Quinn T., Stadel J., Tozzi P., 1999, ApJ, 524, L19

Morris M., Wannier P. G., 1980, ApJ, 238, L7

Nan R., et al., 2011, IJMPD, 20, 989

Navarro J. F., Eke V. R., Frenk C. S., 1996a, MNRAS, 283, L72

Navarro J. F., Frenk C. S., White S. D. M., 1996b, ApJ, 462, 563

Navarro J. F., Frenk C. S., White S. D. M., 1997, ApJ, 490, 493

Neininger N., Guelin M., Klein U., Garcia-Burillo S., Wielebinski R., 1998, A&A, 339, 737

Nilson P., 1973, Uppsala General Catalogue of Galaxies. Astronomiska Observatorium, Uppsala

Noordermeer E., van der Hulst J. M., Sancisi R., Swaters R. A., van Albada T. S., 2005, A&A, 442, 137

Oehm W., Thies I., Kroupa P., 2017, MNRAS, 467, 273

Oh S.-H., de Blok W. J. G., Walter F., Brinks E., Kennicutt R. C., 2008, AJ, 136, 2761

Oh S.-H., de Blok W. J. G., Brinks E., Walter F., Kennicutt R. C., 2011, AJ, 141, 193

Okamoto S., Arimoto N., Ferguson A. M. N., Bernard E. J., Irwin M. J., Yamada Y., Utsumi Y., 2015, ApJ, 809, L1

Oman K. A., et al., 2015, MNRAS, 452, 3650

Oppenheimer B. D., Davé R., Kereš D., Fardal M., Katz N., Kollmeier J. A., Weinberg D. H., 2010, MNRAS, 406, 2325

Ott J., et al., 2012, AJ, 144, 123

Pasquali A., et al., 2008, ApJ, 687, 1004

Pease F. G., 1918, PNAS, 4, 21

Peebles P. J. E., 1965, ApJ, 142, 1317

Persic M., Salucci P., 1992, MNRAS, 258

Pineda J. C. B., Hayward C. C., Springel V., Mendes de Oliveira C., 2017, MNRAS, 466, 63

Pingel N. M., et al., 2018, ApJ, 865, 36

Pisano D. J., 2014, AJ, 147, 48

Pisano D. J., Barnes D. G., Staveley-Smith L., Gibson B. K., Kilborn V. A., Freeman K. C., 2011, ApJS, 197, 28

Pontzen A., Governato F., 2012, MNRAS, 421, 3464

Press W. H., Schechter P., 1974, ApJ, 187, 425

Prestage R., Constantikes K., Hunter T., King L., Lacasse R., Lockman F., Norrod R., 2009, IEEEP, 97, 1382

Punzo D., van der Hulst J. M., Roerdink J. B. T. M., Fillion-Robin J. C., Yu L., 2017, A&C, 19, 45

Read J. I., Gilmore G., 2005, MNRAS, 356, 107

Rhee G., Valenzuela O., Klypin A., Holtzman J., Moorthy B., 2004, ApJ, 617, 1059

Roberts M. S., 1972, IAUS, 44, 12

Roberts M. S., Whitehurst R. N., 1975, ApJ, 201, 327

Rogstad D. H., Shostak G. S., 1971, A&A, 13, 99

Rogstad D. H., Lockart I. A., Wright M. C. H., 1974, ApJ, 193, 309

Rots A. H., 1974, PhD thesis, Univerity of Groningen, http://adsabs.harvard.edu/abs/1974PhDT.....114R

Rubin V. C., Ford, W. K. J., Thonnard N., 1978, ApJ, 225, L107

Sabbi E., Gallagher J. S., Smith L. J., de Mello D. F., Mountain M., 2008, ApJ, 676, L113

Sancisi R., Fraternali F., 2008, A&ARv, 15, 189

Sandage A., Allan 1961, The Hubble Atlas of Galaxies. Washington: Carnegie Institution, http://adsabs.harvard.edu/abs/1961hag..book.....S

Sanders R. H., Verheijen M. A. W., 1998, ApJ, 503, 97

Sault R. J., Teuben P. J., Wright M. C. H., 1995, ASPC, 77, 433

Searle L., Zinn R., 1978, ApJ, 225, 357

Serra P., Jurek R., Floer L., 2012a, PASA, pp 296–300

Serra P., et al., 2012b, MNRAS, 422, 1835

Serra P., et al., 2015, MNRAS, 452, 2680

Simon J. D., Bolatto A. D., Leroy A., Blitz L., 2003, ApJ, 596, 957

Simon J. D., Bolatto A. D., Leroy A., Blitz L., Gates E. L., 2005, ApJ, 621, 757

Smith S., 1936, ApJ, 83, 23

Sofue Y., 1998, PASJ, 50, 227

Sofue Y., Reich W., 1979, A&AS, 38, 251

Sofue Y., Yoshiaki 1997, PASJ, 49, 17

Solanes J. M., Manrique A., Garcia-Gomez C., Gonzalez-Casado G., Giovanelli R., Haynes M. P., 2001, ApJ, 548, 97

Sorce J. G., Tully R. B., Courtois H. M., Jarrett T. H., Neill J. D., Shaya E. J., 2014, MNRAS, 444, 527

Sorgho A., Hess K., Carignan C., Oosterloo T. A., 2017, MNRAS, 464, 530

Sorgho A., et al., 2019a, MNRAS, 482, 1248

Sorgho A., Foster T., Carignan C., Chemin L., 2019b, MNRAS, 486, 504

Soria R., Kuncic Z., Broderick J. W., Ryder S. D., 2006, MNRAS, 370, 1666

Springel V., et al., 2005, Nature, 435, 629

Staveley-Smith L., Kim S., Calabretta M. R., Haynes R. F., Kesteven M. J., 2003, MNRAS, 339, 87

Sullivan W. T. I., Bates B., Bothun G. D., Schommer R. A., 1981, AJ, 86, 919

Swaters R. A., Balcells M., 2002, A&A, 390, 863

Swaters R. A., van Albada T. S., van der Hulst J. M., Sancisi R., 2002, A&A, 390, 829

Swaters R. A., Madore B. F., van den Bosch F. C., Balcells M., 2003, ApJ, 583, 732

Swaters R. A., Sancisi R., van Albada T. S., van der Hulst J. M., 2009, A&A, 493, 871

Taylor A. R., et al., 2003, AJ, 125, 3145

Thomasson M., Donner K. J., 1993, Astronomy and Astrophysics, Vol.272, NO. 1/MAYI, P. 153, 1993, 272, 153

Toomre A., Toomre J., 1972, ApJ, 178, 623

Trager S. C., Faber S. M., Worthey G., González J. J., 2000, AJ, 119, 1645

Tumlinson J., Peeples M. S., Werk J. K., 2017, ARA&A, 55, 389

Valenzuela O., Rhee G., Klypin A., Governato F., Stinson G., Quinn T., Wadsley J., 2007, ApJ, 657, 773

Vargas C. J., et al., 2017, ApJ, 839, 118

Visser H. C. D., 1980, A&A, 88, 149

Vollmer B., Beck R., Kenney J. D. P., van Gorkom J. H., 2004, AJ, 127, 3375

Vollmer B., Braine J., Pappalardo C., 2008, A&A, 464, 455

Walter F., Brinks E., 1999, AJ, 118, 273

Walter F., Weiss A., Martin C., Scoville N., 2002a, AJ, 123, 225

Walter F., Weiss A., Scoville N., 2002b, ApJ, 580, L21

Walter F., Brinks E., de Blok W. J. G., Bigiel F., Kennicutt R. C., Thornley M. D., Leroy A., 2008, AJ, 136, 2563

Wang J., et al., 2014, MNRAS, 441, 2159

Wang J., Koribalski B. S., Serra P., van der Hulst T., Roychowdhury S., Kamphuis P., N. Chengalur J., 2016, MNRAS, 460, 2143

Weisz D. R., Skillman E. D., Cannon J. M., Walter F., Brinks E., Ott J., Dolphin A. E., 2009, ApJ, 691, L59

Weldrake D. T. F., De Blok W. J. G., Walter F., 2003, MNRAS, 340, 12

White S. D. M., Frenk C. S., 1991, ApJ, 379, 52

White S. D. M., Rees M. J., 1978, MNRAS, 183, 341

Winkel B., Kerp J., Flöer L., Kalberla P. M. W., Bekhti N. B., Keller R., Lenz D., 2016, A&A, 585, A41

Wolfe S. A., Pisano D. J., Lockman F. J., McGaugh S. S., Shaya E. J., 2013, Nature, 497, 224

Wolfe S. A., Lockman F. J., Pisano D. J., 2016, ApJ, 816, 81

Wright E. L., et al., 2010, AJ, 140, 1868

Yi S. K., et al., 2005, ApJ, 619, L111

York D. G., et al., 2000, AJ, 120, 1579

Yun M. S., 1999, IAUS, 186, 81

Yun M. S., Ho P. T. P., Lo K. Y., 1993, ApJ, 411, L17

Yun M. S., Ho P. T., Lo K. Y., 1994, Nature, 372, 530

Zhao H., Famaey B., 2006, ApJ, 638, L9

Zschaechner L. K., Rand R. J., Heald G. H., Gentile G., Kamphuis P., 2011, ApJ, 740, 35

Zschaechner L. K., Rand R. J., Heald G. H., Gentile G., Józsa G., 2012, ApJ, 760, 37

Zwicky F., 1933, Helv. Phys. Act., 6, 110

Zwicky F., 1937, ApJ, 86, 217

de Blok W. J. G., 2010, Adv. Astron., 2010, 5

de Blok W. J. G., McGaugh S. S., Bosma A., Rubin V. C., 2001, ApJ, 552, L23

de Blok W. J. G., Walter F., Brinks E., Trachternach C., Oh S.-H., Kennicutt R. C., 2008, AJ, 136, 2648

de Blok W. J. G., et al., 2014, A&A, 569, A68

de Blok W., et al., 2018a, in Proceedings of MeerKAT Science: On the Pathway to the SKA – PoS(MeerKAT2016). Sissa Medialab, Cape Town, doi:10.22323/1.277.0007, https://pos.sissa.it/277/007

de Blok W. J. G., et al., 2018b, AJ, 865, 26

de Mello D. F., Smith L. J., Sabbi E., Gallagher J. S., Mountain M., Harbeck D. R., 2008, AJ, 135, 548

de Vaucouleurs G., 1959, HDP, 53, 275

de Vaucouleurs G., de Vaucouleurs A., Corwin, H. G. J., Buta R. J., Paturel G., Fouqué P., 1991, Third Reference Catalogue of Bright Galaxies. Volume I: Explanations and references. Volume II: Data for galaxies between 0h and 12h. Volume III: Data for galaxies between 12h and 24h. Springer, http://adsabs.harvard.edu/abs/1991S{&}T....82Q.621D

van Albada T. S., Bahcall J. N., Begeman K., Sancisi R., 1985, ApJ, 295, 305

van Dokkum P. G., Franx M., Fabricant D., Kelson D. D., Illingworth G. D., 1999, ApJ, 520, L95

van Woerden H., van Driel W., Schwarz U. J., 2004, in Athanassoula E., ed., IAUS Vol. 100, Internal kinematics and dynamics of galaxies. Cambridge University Press, pp 99–104, http://adsabs.harvard.edu/abs/1983IAUS..100...99V

van de Hulst H. C., 1945, Nederlandsch Tijdschrift voor Natuurkunde (in Dutch; reprinted in Sullivan III, paper 34), 11, 210

van de Hulst H. C., Raimond E., van Woerden H., 1957, Bull. Astron. Inst. Netherlands, 14, 1

van den Bosch F. C., Robertson B. E., Dalcanton J. J., de Blok W. J. G., 2000, AJ, 119, 1579

van der Hulst J. M., 1979, A&A, 75, 97

van der Hulst J. M., Terlouw J. P., Begeman K. G., Zwitser W., Roelfsema P. R., 1992, ASPC, 25, 131